New Frontiers in Exoplanet Detection: High Contrast Imaging with Subaru

Courtney Danielle Dressing

Advisors: Professor Edwin Turner and Dr. Michael McElwain

Submitted in partial fulfillment

of the requirements for the degree of

Bachelor of Arts

Department of Astrophysical Sciences

Princeton University

April 2010

I hereby declare that I am the sole author of this thesis.

I authorize Princeton University to lend this thesis to other institutions or individuals for the purpose of scholarly research.

Courtney Danielle Dressing

I further authorize Princeton University to reproduce this thesis by photocopying or by other means, in total or in part, at the request of other institutions or individuals for the purpose of scholarly research.

Courtney Danielle Dressing

Abstract

The Subaru Strategic Exploration of Exoplanets and Disks (SEEDS) collaboration is conducting high-contrast observations of exoplanets and disks using the 188 actuator AO system (AO188), classical Lyot coronagraph, and near infrared differential imaging science camera (HiCIAO) on the Subaru Telescope. This work supports the SEEDS project by conducting an analysis of the importance of field rotation for observations acquired in angular differential mode (ADI). ADI suppresses optical speckle features by fixing the telescope point spread function (PSF) with respect to the science camera detector, while allowing the field with any companions to rotate freely. In post processing, the sequence of images are registered and combined to produce a reference PSF that is subtracted from each image. The final images are de-rotated to realign the field with a fixed position angle. We find that increasing field rotation does influence sensitivity and that doubling the amount of field rotation in an observation can reduce the minimum angular separation at which companions can be detected by 0.1" and increase the sensitivity of an observation by factors of ∼2–4 at separations of ∼0.2"–0.4". These results emphasize the importance of conducting ADI observations during transit when the rotation rate of the target is maximized.

Acknowledgements

First and foremost, I would like to thank my advisors Professor Edwin Turner and Dr. Michael McElwain for providing superb guidance and support throughout the year and for funding my travel to Hawaii to participate in the January SEEDS observing run. My thesis would still be in the drafting stages without all of your helpful comments and suggestions. I would also like to thank Professor Gillian Knapp for agreeing to be my second reader and for funding my continued involvement with the SEEDS collaboration this summer. Thank you also to the rest of the Princeton SEEDS team for welcoming me to the collaboration and for offering advice during team meetings. The help@astro team of Steve Huston, Leigh Koven, and Robert Lupton is always phenomenal, but in this case they really went above and beyond the call of duty. Thank you very much to Steve, Leigh, and Robert for the many hours you spent tackling the wakusei problem and for giving me permission to crash the computer. Thank you also to Cullen Blake and Dave Spiegel for graciously allowing me to use your computers to complete my reductions. I would also like to thank SEEDS PI Dr. Motohide Tamura and the rest of the SEEDS team for allowing me to become involved in the SEEDS project. This project would not have been possible without their years of hard work and dedication to the project. As always, thank you to Team Astro for your friendship, laughter, and constant willingness to take breaks for tea and cookies.

In memory of Paul Stumpe

Contents

List of Tables

List of Figures

Chapter 1

Introduction

Come, my friends,

'Tis not too late to seek a newer world. . . .

To sail beyond the sunset, and the baths

Of all the western stars, until I die.

Alfred Lord Tennyson, Ulysses, 1842.

1.1 A Brief History of Exoplanet Detection

Although planets around other stars have been discussed in literature for generations, the era of extrasolar planet discovery is only just beginning. In 1992, radio astronomers Aleksander Wolszczan and Dale Frail serendipitously discovered the first extrasolar planets when they observed a sinusoidal variation in the arrival time of pulses from the millisecond radio pulsar PSR1257+12 (Wolszczan & Frail 1992). Wolsczan and Frail attributed the timing variation to the presence of two or more planets in the PSR1257+12 system. They calculated that both planets were in roughly circular orbits and that the less massive planet had a period of 98.2 days while the more massive planet orbited slightly closer to the star in a 66.6 day or-

bit. Follow-up studies constrained the masses of the planets to 3.9±0.2 $M_\oplus$ and 4.3±0.2 $M_\oplus$, respectively. Although astronomers were initially surprised to discover planets around a non-main-sequence star, the subsequent detection of mutual gravitational perturbations in the orbits of the objects confirmed that both planets were bound to the star (Rasio et al. 1992; Malhotra et al. 1992; Peale 1993; Wolszczan 1994; Konacki et al. 1999) and provided an early clue that extrasolar planets are more varied than one might expect based on the properties of our own solar system.

Three years later, Michel Mayor and Didier Queloz of the Geneva Observatory announced the detection of the first extrasolar planet orbiting a main sequence star (Mayor & Queloz 1995). The 0.468 M_J planet was detected using the radial velocity technique explained in Section 1.2.1, and orbits the G5 star 51 Peg on a 4.32-day orbit. Since the discovery of 51 Peg b, over 440 planets have been detected around main sequence stars.[1] Several notable landmark discoveries include 47 Uma b, Gliese 876 b, Iota Draconis b, and HD 209458 b. The detection of 47 Uma b in a nearly circular orbit (e=0.032) at 2.1 AU (Butler & Marcy 1996) proved that not all exoplanets orbited their host stars at the extremely small separations observed for previously known exoplanets (a=0.051 AU for 51 Peg b, a=0.48 AU for 70 Vir b). The subsequent detection of the $M\sin i = 2M_J$ giant planet Gliese 876 b around an M4 dwarf by Delfosse et al. (1998) and the detection of the $M\sin i$=8.9 M_J planet Iota Draconis b around a KII giant star by Frink et al. (2002) demonstrated the remarkable diversity of planetary host stars and indicated that astrophysicists might be able to find planets orbiting a wide range of compact objects. The 0.62 M_J planet HD 209458 b had been previously detected in radial velocity observations, but made history in 1999 when it became the first exoplanet observed to transit its host star (Castellano et al. 2000; Charbonneau et al. 2000; Henry et al. 2000). Although the planet was already known, the detection of the transit marked a crucial development in exoplanet detection

[1] www.exoplanet.eu

capabilities and presented a new way to detect and confirm planets.

The accelerating rate of planet discoveries in recent years is largely due to the increased baseline for planet surveys, the improved precision of radial velocity surveys, the launch of dedicated planet-hunting missions such as *CoRoT* (Barge et al. 2008) and *Kepler* (Borucki et al. 2010), and advances in adaptive optics as well as the inception of large-scale ground-based planet surveys. Several of the most notable planet surveys are the Anglo-Australian Planet Search[2] (Tinney et al. 2001), the California and Carnegie Planet Search[3] (Boss et al. 2009), the Geneva Extrasolar Planet Search[4] (Queloz et al. 2000), the Hungarian Automated Telescope Network[5] (Bakos et al. 2009), the MEarth project[6] (Charbonneau et al. 2009), the Optical Gravitational Lensing Experiment[7] (Albrow et al. 2000), the Super Wide Angle Search for Planets[8] (Cameron et al. 2007), and the Trans-Atlantic Exoplanet Survey[9] (Alonso et al. 2004). This paper will concentrate on a relatively new survey, the Subaru Strategic Exploration of Exoplanets and Disks project. The SEEDS survey saw scientific first light in 2009, and is described in detail in Chapter 4.

1.2 Planet Detection Methods

The majority of exoplanets have been discovered via radial velocity measurements, but transit measurements, gravitational microlensing, and direct detection have also been successful in detecting planets. Although the focus of this paper is direct detection, a basic understanding of other planet detection methods is necessary in order to appreciate the biases and advantages inherent in each detection technique. Accord-

[2] http://www.phys.unsw.edu.au/~cgt/planet/AAPS_Home.html
[3] http://exoplanets.org/
[4] http://obswww.unige.ch/exoplanets/
[5] http://www.hatnet.hu/
[6] http://www.cfa.harvard.edu/~zberta/mearth/
[7] http://ogle.astrouw.edu.pl/
[8] http://www.superwasp.org/
[9] http://www.lowell.edu/Research/OtherResearch/index.html

ingly, an explanation of each of the main planet detection methodologies follows.

1.2.1 Radial Velocity

As Isaac Newton wrote in the *Principia* (Newton 1687), two orbiting bodies exert forces on each other and rotate around their mutual center of gravity, which is known as the barycenter. In planetary systems the star is typically much more massive than the planet, so the barycenter is much closer to the star than to the planet. Quantitatively, if the mass of the planet is $M_{\rm p}$ and the mass of the star is $M_{\rm s}$ and the two systems are separated by distance r, then the positions $R_{\rm p}$ and $R_{\rm s}$ of the planet and star, respectively, with respect to the barycenter, are given by

$$R_{\rm p} = \frac{M_{\rm s}}{M_{\rm p} + M_{\rm s}} r \,, \qquad R_{\rm s} = \frac{M_{\rm p}}{M_{\rm p} + M_{\rm s}} r \,.$$

For the Sun-Jupiter system, $M_{\rm p} = 9.54 \times 10^{-4}\,{\rm M}_\odot$, $M_{\rm s} = {\rm M}_\odot$, and $r = 5.4$ AU, so the barycenter is $R_{\rm p} = 5.199$ AU from Jupiter and $R_{\rm s} = 0.0049$ AU (7.4×10^5 km) from the Sun. Comparing the position of the barycenter to the radius of the Sun (4.379×10^6 km), we see that the barycenter for the Sun-Jupiter system is only 17% of the Sun's radius from the center of the Sun. Although the distance from the center of the Sun to the barycenter is a factor of 10^3 smaller than the separation between Jupiter and the Sun, the fact that the gravitational influence of a planet causes a star to orbit around a point that is not its own center means that exoplanets can be detected indirectly by looking for slight shifts in stellar position.

If the system is edge-on, meaning that the orbital plane of the planet lies along to our line of sight (orbital inclination $i = 90°$), then the star will alternatively move towards us and away from us as it orbits the barycenter. While the shift in the position of the star might not be detectable, the change in the velocity of the star can be measured to high precision by comparing the observed frequency of

spectral lines to their known rest-frame positions. After observing a star for several orbits, astronomers then subtract out the velocity signature corresponding to the space velocities of the star and the observer to isolate any possible periodic variations in the stellar velocity that might be caused by planets. Next, astronomers analyze the resulting radial velocity curve and attempt to fit planetary or stellar companions to the system to explain the radial velocity variations. In the case of an edge-on, single planet system, the period of the oscillation will be determined by the semimajor axis of the planet's orbit, and the magnitude of the oscillation will be a simple function of the mass and eccentricity of the planet. In more realistic cases, however, astronomers have to allow for a range of viewing angles, inclinations, and eccentricities. For extremely precise analyses of radial velocity curves, the gravitational interactions between the planets in a multi-body system must also be considered.

Despite the complicated nature of unraveling radial velocity curves in the face of stellar variability and unknown orbital parameters, radial velocity surveys have been incredibly successful. To date, over 350 planets ($\sim$80% of all known exoplanets) have been detected by radial velocity surveys, and radial velocity measurements are frequently used to confirm planets detected by other means and to provide additional information about planetary properties. Current radial velocity surveys are able to determine velocities with $<$1 m/s precision at visible wavelengths (Mayor et al. 2009) and with $\lesssim$10 m/s precision at infrared wavelengths (Figueira et al. 2010b). Both visible and infrared surveys are precise enough to detect the $\sim$28 m/s radial velocity signature of a $\sim$1 $M_{\rm J}$ planet in a circular orbit 1 AU from a Sun-like star, but only visible surveys are presently able to detect a $\sim$0.1 $M_{\rm J}$ planet at the same orbital radius (Cumming 2004).

While radial velocity surveys have detected a phenomenal number of planets, they do have limitations. The primary limitation is that in order for a radial velocity survey to detect a planet, the system must be oriented so that the star moves towards and

away from the observer. Consequently, planets in face-on and near face-on systems are invisible to radial velocity surveys. The second limitation is that the magnitude of the star's radial velocity motion must be above the current detection limit of $\sim$1 m/s for surveys at visible wavelengths or $\sim$10 m/s for surveys at infrared wavelengths. Since the gravitational force exerted on the star increases with increasing planet mass, radial velocity surveys are therefore more sensitive to Jupiter-mass planets than to Earth-mass planets. A related limitation is that radial velocity surveys are only sensitive to planets around stars with narrow absorption or emission lines. The Doppler shifts in line frequency due to the presence of a planet may be several orders of magnitude smaller than stellar line widths (Herbig & Spalding 1955), so stellar line position must be measured to high accuracy in order to detect the presence of a planet. Accordingly, current radial velocity surveys cannot yet detect planets around stars with high intrinsic radial velocity variability due to activity (Santos et al. 2000), or around stars with few spectral lines (Griffin 1973) or gravitationally- or rotationally-broadened spectral lines (Griffin 1973).

Additionally, radial velocity surveys are more sensitive to planets in shorter-period orbits because the time required for repeat observations is shorter than the time required to confirm radial velocity perturbations caused by more distant planets. The final limitation of radial velocity surveys is that they provide only a minimum measurement of the planet mass because the orbital fit yields a measurement of $M \sin i$ rather than M. If the inclination of the system can be constrained by other means, then the measurement of $M \sin i$ can be converted to a measurement of the actual planetary mass M, but in most cases the upper limit of the mass remains unconstrained.

1.2.2 Astrometry

Like the radial velocity method, astrometry surveys also detect planets indirectly by looking for perturbations in the motion of the star. The difference between radial velocity surveys and astrometric surveys is that radial velocity surveys work best for edge-on or near edge-on systems while astrometric surveys favor face-on or near face-on systems. If a system is face-on, meaning that the orbital plane of the planet is perpendicular to our line of sight (orbital inclination $i = 0°$), then the star will appear to trace a small circle or ellipse in the sky as it orbits the center of mass of the planet-star system. Since larger mass planets at greater separations move the center of mass outward away from the center of the star, astrometric surveys are most sensitive to massive planets at relatively wide separations compared to the planets detected by radial velocity and transit surveys. However, because orbital period increases with semimajor axis, a longer period of observation is required to confirm the orbital motion of planets detectected by astrometry than to confirm the orbital motion of shorter-period planets detected via radial velocity or transit measurements.

Despite the theoretical promise of astrometry, the difficulty of accurately constraining stellar positions to the required extreme subpixel precision has (as of April 2010) precluded the identification of new exoplanets using astrometry (Anglada-Escudé et al. 2010; Bean et al. 2010). Several astrometric planet candidates have been announced, but all of the candidates have been later retracted when they failed to appear in follow-up radial velocity observations. One recent example is VB 10b, a 6.4 $M_{\rm J}$ planetary candidate in a 0.7444 year orbit detected via astrometry by Pravdo & Shaklan (2009). Although the candidate was observed over 9 years and appeared to be a strong candidate during the astrometric survey (Pravdo & Shaklan 2009), the lack of detection in subsequent radial velocity observations suggests that VB 10b does not actually exist (Anglada-Escudé et al. 2010; Bean et al. 2010).

While astrometry has failed to detect any new planets, it has been a useful way to

place upper limits on the planetary mass of planets detected via the radial velocity method (Han et al. 2001). As explained in Section 1.2.1, radial velocity surveys measure $M_{\rm p} \sin i$ rather than $M_{\rm p}$, so the mass of planets could differ significantly from the minimum possible value. Conducting follow-up observations with astrometry is one way to reduce the possible uncertainty in companion mass and determine whether a possible companion is stellar or substellar in nature. For example, astrometric measurements by McGrath et al. (2002, 2003) revealed that the $M_{\rm p} \sin i = 0.84 M_{\rm J}$ object detected by Butler et al. (1997) around the G8 star HR 3522 (ρ^1 Cnc) has an upper mass limit of 30 $M_{\rm J}$, confirming that it is a substellar object ($M_{\rm substellar} \lesssim 80 M_{\rm J}$) and not a low-mass star ($M_* \gtrsim 80 M_{\rm J}$).

Future generations of astrometric surveys will likely be useful for detecting new planets as well as constraining the masses of previously detected planets. Although current and past surveys have measured stellar positions on the milliarcsecond level, future surveys will be capable of determining positions at microarcsecond resolution (Sozzetti 2009). The sensitivity of astrometric surveys to exoplanets can be approximated by computing the "astrometric signature" of a planet of a certain mass at a given separation. If the planet is on a circular orbit, then the magnitude of the astrometric signature in arcseconds is given by the scaling relation:

$$\alpha = \frac{M_{\rm P}}{M_*} \frac{a}{D} \ ,$$

where a is the separation in AU between a planet of mass $M_{\rm P}$ (in $\rm M_\odot$) and a star of mass M_* (in $\rm M_\odot$) and D is the distance to the star in parsecs (Sozzetti 2005). Consequently, a Jupiter-mass planet in a circular orbit around a 1 $\rm M_\odot$ star with a semimajor axis of 1 AU would produce an astrometric signature of 100 μas assuming that the system was 10 pc from Earth. A Jupiter-mass planet at 10 AU would produce a signature of 1000 μas, but an Earth-mass planet at 1 AU would result in a

signature of only 0.33 μas, which is far below the $\sim$mas precision of current astrometric surveys. With the advent of next-generation space-based astrometry surveys like the European Space Agency's Gaia (Perryman et al. 2001) and the National Aeronautics and Space Administration's Space Interferometry Mission PlanetQuest (Unwin et al. 2008), massive planets at wide separations ($\gtrsim$0.1 AU for $M_{\rm P} \sim M_{\rm J}$) will no longer lie beyond the detection limits of astrometry.

1.2.3 Microlensing

Unlike other planet detection methods, microlensing is an effective way to detect a remarkable variety of planets (Gaudi 2010). The theory of microlensing was first established by Einstein (1936) and follows naturally from the theory of gravitational lensing first published by Chwolson (1924). During gravitational lensing events, the gravitational influence of a foreground object bends the path of light rays from a more distant object so that the background object appears to be at a different position in the sky. Depending on the orientation of the observer, foreground object, and background object and the density structures of the two objects, the observer may see multiple images of the background source or even a continuous ring of images surrounding the foreground object (Refsdal 1964). In gravitational *micro*lensing events, the multiple images of the background source are too close together to be resolved, but because the total surface area of the images is greater than the surface area of the unlensed source, the background source appears brighter during a microlensing event (Einstein 1936).

In the context of exoplanets, if a background source is lensed by a foreground star with a planet, then the gravitational influence of the planet can cause a secondary spike in source brightness during the microlensing event as shown in Figure 1.1 (Mao & Paczynski 1991; Gould & Loeb 1992). A planet-induced microlensing event will only occur if the planet is located near one of the lensed images of the background

source, but planetary microlensing events are sensitive to a wide range of planetary masses and separations. Due to the geometry of the event, although the duration of the planetary microlensing event scales as $M_{\rm P}^{1/2}$, above a ~1-5 $M_\oplus$ lower limit based on host star mass, the magnitude of the brightness amplification is independent of planet mass (Gaudi 2010).

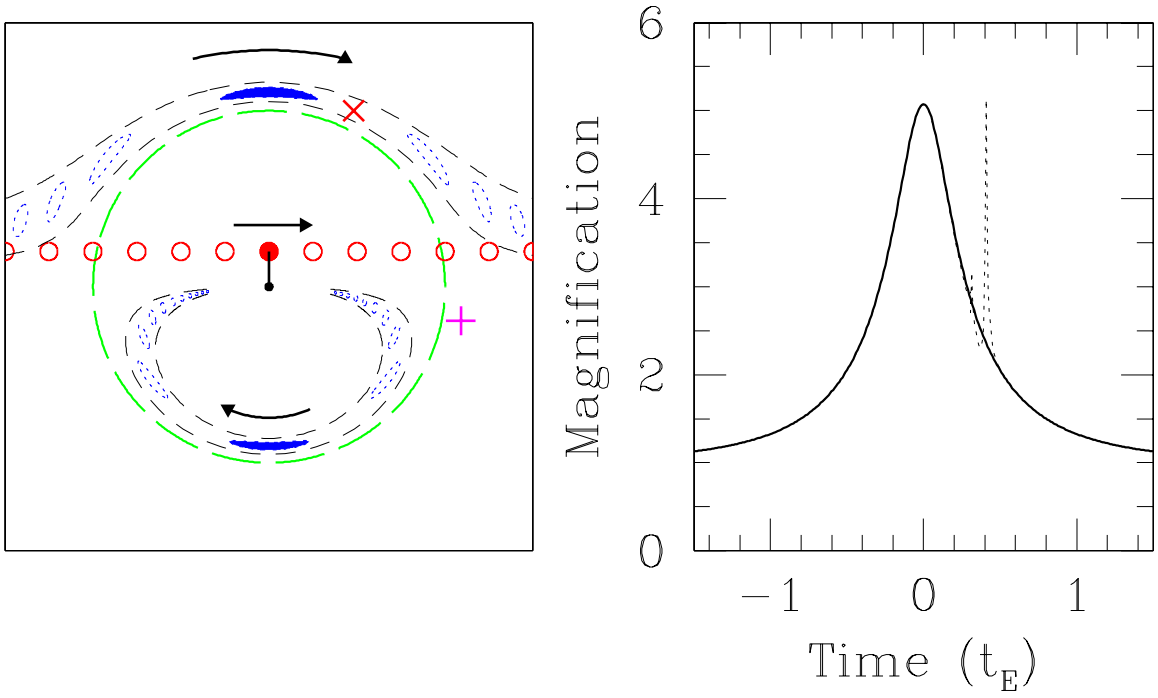

Figure 1.1: Schematic of planetary microlensing event from Gaudi (2010). **Left:** Cartoon depicting the configuration of the lensing system. The lens star is represented by the black dot at the center of the figure, and the blue ovals display the location of the lensed images for several possible locations of the source (red circles). The dashed green circle is the Einstein ring radius of the source, and the images depicted by solid blue ovals correspond to the position of the images when the source is located at the filled red dot. If the lens star has a planet located within the dashed black lines (e.g., at the red ×), then the gravitational influence of the planet will cause a spike in the microlensing light curve. However, if the planet is located outside of the black lines (e.g., at the pink +), then the planet will not affect the microlensing light curve. **Right:** Light curve depicting the brightness of the system as a function of time. The dark solid line is the magnification in brightness due to the presence of the host star alone, and the dashed line is the additional spike in brightness that will occur if the host star has a planet that lies within the dashed black lines shown in the left-hand figure.

Unlike radial velocity and transit surveys, which are most sensitive to planets close

to the star, microlensing surveys are best at detecting planets near the Einstein ring radius of the star, which typically lies beyond the snow line (Mao & Paczynski 1991). The "snow line" is the distance from a star at which the temperature first becomes low enough that water ice is stable. Accordingly, characterizing planets on either side of the snow line is important for understanding planet formation (e.g., Kennedy & Kenyon 2008). Microlensing surveys are also uniquely capable of detecting planets around stars at large distances from Earth, including planets in the bulge of the Milky Way (Kiraga & Paczynski 1994). The farthest planet detected lies 6500 pc from Earth (OGLE-05-390L b: Beaulieu et al. 2006), and microlensing surveys may even be able to detect planets in M31 by observing the changes in brightness of a single pixel (Covone et al. 2000; Chung et al. 2006; Ingrosso et al. 2009).

The drawback to microlensing surveys is that the planets detected by microlensing cannot be re-observed because they are typically much too far from Earth to be observed by another method and the chance that the star will participate in another microlensing event are very low. Despite the inability to re-observe planets, however, microlensing light curves contain a significant amount of information about the planet and host star. The planetary mass and the projected separation between the planet and the star can be determined from the shape of the light curve, and multiple planets can even be detected around a single star depending on the alignment of the system during the microlensing event. Information from the light curve can then be combined with data acquired during follow-up observations of the star to determine the mass, spectral type, and approximate age of the host star (Gaudi 2010). Although this subsection has characterized planet detection via microlensing events as a rather straightforward process, the actual work of detangling light curves to produce an image of the lensing system is quite complicated because of the degeneracies between the distance of the lens and the mass of the lensing system (Loeb & Sasselov 1995; Gaudi & Gould 1997). See Bennett (2008) for a more thorough discussion of the

intricacies of microlensing planet surveys.

1.2.4 Transits

Of all of the current planet detection methods, transit surveys are the only method that provides a measurement of the planet's radius as well as its orbital period. An astronomical transit occurs when one celestial body moves between an observer and a background celestial body and blocks some of the light from the background object. Unlike microlensing surveys, the primary concern in transit surveys is not the gravitational effect of the planet's mass on the path of the light, but the physical obstruction of light from the host star by the planet. Just as in a binary star system, astronomers observe a transit by monitoring the brightness of a target star and looking for periodic dips in brightness.

An example schematic of a planetary transit and the corresponding light curve are displayed in Figure 1.2. Neglecting variations in stellar luminosity due to starspots or other astrophysical processes, the brightness of the star is roughly constant when the planet is not transiting (point 1). Once the planet crosses the edge of the star (point 2), the brightness of the star decreases as more of the stellar surface is blocked. For the transit of a planet-sized object across a much larger star, the center of the transit (point 3) will be approximately flat because the stellar area blocked by the planet remains constant during the middle of the transit. At the end of the transit, the planet crosses the other edge of the star and the brightness increases to the pre-transit level. By carefully studying the slope of the light curve during transit ingress and egress, astronomers can determine the relative sizes of the planet and the star. Since the radius and mass of the star can be determined from the star's spectral type, the radius and semimajor axis of the planet can be determined by combining the periodicity and depth information from the light curve with the results of spectroscopic analysis of the star. The mass of the planet can then be established by follow-up radial velocity

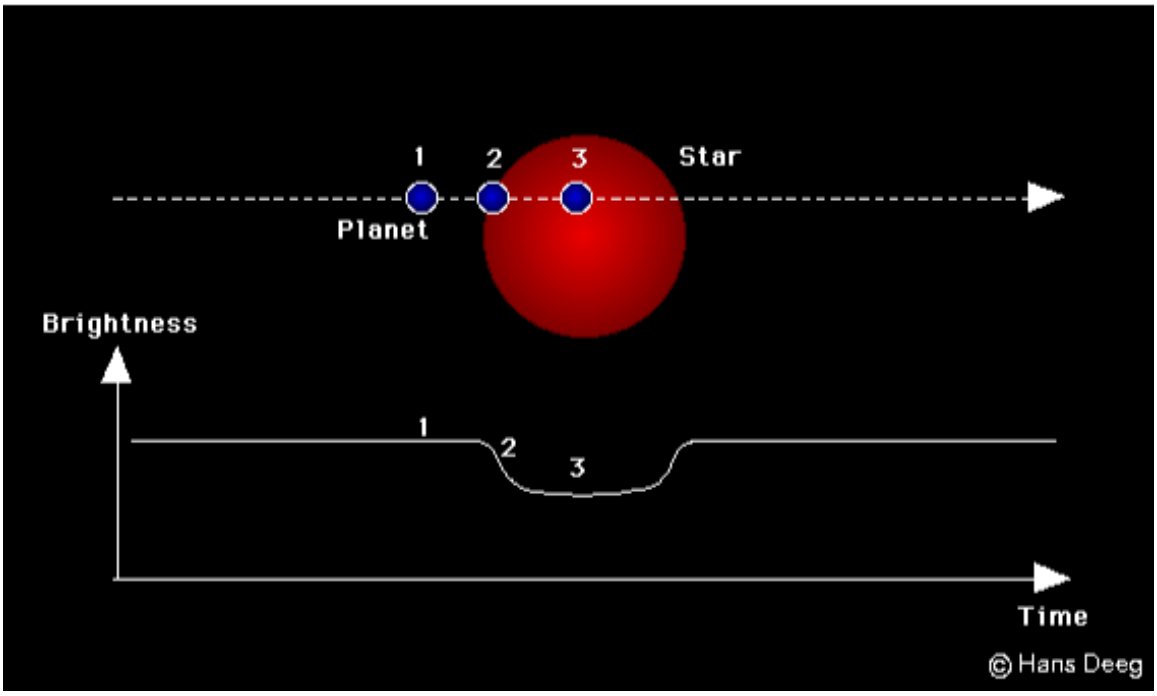

Figure 1.2: Artist's rendition of a planetary transit and the associated light curve. The brightness of the star is roughly constant when the planet is not crossing the surface (point 1), but once the transit begins (point 2), the brightness drops. Since the cross-section of the planet is much smaller than the cross-section of the star, the transit light curve reaches a flat bottom for the majority of the transit (point 3). After the planet reaches the far side of the star, the brightness begins to increase, and the full brightness of the star is restored when the planet is no longer blocking the star. This figure was produced by Hans Deeg.[11]

observations as explained in Section 1.2.1.

The transit method of detecting exoplanets has been incredibly successful, but planets detected via transit surveys must be verified by other means given the high rate of false positives in transit searches (Brown 2003). The false positives are due to starspots on the target star, spectroscopic "blends" of eclipsing binary stars in the field of view, and other astrophysical phenomena. Despite the risk of false detections, the transit method has resulted in the discovery of 71 exoplanets[12] and allowed scientists to compute planetary densities for the first time. In addition, comparison of spectra obtained during the course of a transiting planet's orbit has even allowed astronomers to probe exoplanet atmospheres (Charbonneau et al. 2002).

Since the detectability of a transit is proportional to the ratio of the cross-sectional area of the planet to that of the star as seen by an observer at Earth, transit surveys, like radial velocity surveys, are most sensitive to large planets very close to their host stars. Such planets have temperatures as high as ∼2300 K (Harrington et al. 2007), and are known as "Hot Jupiters." These planets are certainly not the place to search for life in the universe, but by closely measuring the timing of consecutive transits, astronomers can detect additional planets around the same star through transit timing variation measurements (Holman & Murray 2005). These additional planets may be observable with radial velocity, astrometry, or direct imaging techniques. In special cases, additional planets may also be detected via transits if the additional planet also transits the host star and the observer knows the orbital period and phase of the predicted planet.

In addition to revealing the presence of additional planets, careful analysis of transit light curves can also yield information about the inclination of the system. As proposed by Rossiter (1924) and McLaughlin (1924), the inclination of a planetary orbit with respect to the star's spin axis can be determined by monitoring the redshift

[12] `exoplanet.eu`

of the light received during a transit. In the simple case where the star's rotational axis is perpendicular to an observer's line of sight, the rotation of the star causes half of the star to appear blueshifted and the other half to appear redshifted. As shown in Figure 1.3 (modified from Gaudi & Winn 2007), if a transiting planet orbits in the same direction as the stellar rotation, then the planet will block first blueshifted and then redshifted light during the course of the transit. The star will therefore appear first redshifted and then blueshifted. If the planet is in a retrograde orbit, then the star will appear blueshifted first and redshifted second. The situation is more complicated when the planet is on an inclined orbit or the stellar rotation axis is not perpendicular to the line of sight, but the projection of the angle between the star's spin axis and the planet's rotation axis can still be measured (Ohta et al. 2005; Gaudi & Winn 2007). This knowledge is important because orbital inclinations may provide clues about the dynamics of planetary formation and migration (Fabrycky & Winn 2009).

1.2.5 Direct Detection

Unlike other detection methods which can only detect planets indirectly through their gravitational influence and interference with light from their host star, the direct detection method takes advantage of advances in adaptive optics and high contrast imaging to produce actual images of exoplanets. Due to the brightness of the host star, direct detection is most sensitive to planets at wide separations where the flux from the star is reduced. Even at wide separations, however, the stellar flux can still be several orders of magnitude greater than the planetary flux (Oppenheimer & Hinkley 2009), so direct detection typically requires both adaptive optics and special observing techniques (see Section 3.2) to reduce the stellar flux to the point where planets can be detected.

Given the difficulty in detecting flux from a planet in close proximity to a bright

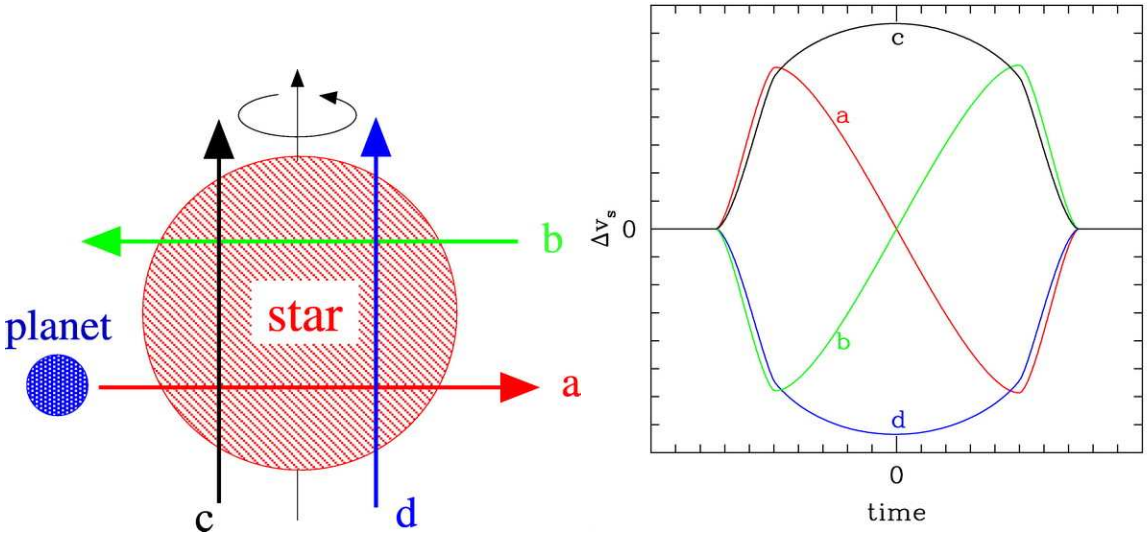

Figure 1.3: Diagram of the Rossiter-McLaughlin Effect from Ohta et al. (2005). **Left:** The colored lines indicate four possible paths of a transiting planet. As indicated by the rotational velocity vector, the left side of the star is moving out of the page while the right half of the star is rotating into the page. Accordingly, the light from the left half of the star appears blueshifted and the light from the right side of the star appears redshifted. **Right:** The deviations in the velocity curve seen by an observer for each of the possible paths of the transiting planet shown in the left panel. For the red path ("a"), the planet transits the star in a prograde orbit and blocks first blueshifted light and then redshifted light. The light seen by the observer during the transit is thus redshifted at the beginning of the transit and blueshifted at the end of the transit. If the planet orbited the star in the retrograde orbit indicated by the green path ("b"), then the observer would see blueshifted light first and redshifted light second. If the planet crosses only the left side or right side of the star, then the light appears only redshifted or only blueshifted, respectively.

star, direct imaging surveys usually conduct observations in the near-infrared to decrease the contrast ratio between the planet and star brightness, and because current adaptive optics technology works only at infrared wavelengths. As discussed in detail in Section 2, Jovian planets are hot when they are formed and then cool slowly for the rest of their lifetimes (Burrows et al. 1997). Accordingly, exoplanets are much easier to detect when they are young and still retain much of the heat from formation. Direct detection surveys therefore tend to target young ($\lesssim$100 Myr) stars in the hope of detecting planets that are still young enough to emit a significant amount of flux in the near-infrared. To avoid confusion with the "Hot Jupiters" detected by transit surveys, the young, hot Jovian planets imaged by direct detection surveys are referred to as "Young Jupiters."

As of April 2010, direct detection surveys have imaged twelve confirmed planets with semimajor axes ranging from <10 AU to several hundred AU.[13] The properties of all twelve directly detected substellar objects are shown in Table 1.1. The first directly imaged planet was 2M1207 b, which is a $5 \pm 2 M_{\rm J}$ planet in an orbit with a semimajor axis of $\sim$55 AU around a brown dwarf (Chauvin et al. 2004). The reduced brightness of the brown dwarf compared to a main-sequence star significantly decreased the contrast required to detect the planet, but the discovery was a remarkable feat for high-contrast imagers. Several years later, the discovery of a 1-42 $M_{\rm J}$ companion to the K-star GQ Lup was announced by Neuhäuser et al. (2005), but recent follow-up observations by McElwain et al. (2007) and Lavigne et al. (2009) suggest that the object actually has a higher mass of 8-60 $M_{\rm J}$ and is most likely a brown dwarf rather than a gas giant. In addition to refining mass estimates, follow-up observations of directly detected planets are necessary to ensure that the object is gravitationally bound to the star. For stars with high proper motions, determining that an object is bound to the star can be accomplished by checking whether the planet exhibits

[13] See www.exoplanet.eu

common proper motion, meaning that it moves relative to the background stars in the same manner as the likely host star.

As displayed in Table 1.1, the planets detected by direct detection have masses between $3M_{\rm J}$ and $21.5M_{\rm J}$, and appear 0.4-14.9" from their host stars. Interestingly, all of the planets listed were detected around either massive A stars or low mass K and M stars. The relatively low luminosity of K and M stars improves the contrast ratio between the star and planet and decreases the difficulty of detecting a planet, but the steep increase in stellar luminosity with increasing mass should make exoplanets much harder to detect around A stars than around sun-like stars. However, theoretical models (Kennedy & Kenyon 2008) and results from radial velocity surveys (Johnson et al. 2007) indicate that high mass stars may actually be more likely than sun-like stars to harbor long-period gas giants. Additionally, the short lifespan of A stars ensures that any planets orbiting A stars will be $\lesssim$5 Gyr old.

Even if widely-separated Jovian planets are more common around high mass stars than around low-mass stars, the lack of directly imaged planets around Sun-like stars is likely partially due to the small sample size and the relative youth of direct detection surveys. Consequently, the current census of directly detected planets should not be considered representative of the actual frequency of widely-separated Jovian planets around Sun-like stars. In fact, Thalmann et al. (2009) recently announced the discovery of a 10-40$M_{\rm J}$ companion in a $\sim$55 AU orbit around the G9 star GJ 758.[14] Although the companion may be a brown dwarf and not a giant planet, the detection of a substellar object in a wide orbit around a Sun-like star indicates that solar system type configurations with widely separated Jovian planets and inner terrestrial planets closer to the star might not be uncommon in the universe.

[14]GJ 758 b is not included in Table 1.1 because it is currently listed as a "controversial" planet on `exoplanet.eu` due to its 10-40$M_{\rm J}$ estimated mass range, which suggests that GJ 758 b may be a brown dwarf ($M_{\rm P} > 13M_{\rm J}$) instead of a planet.

Table 1.1: Properties of Planets Discovered Through Direct Imaging

Planet Name[a]	Planet Mass (M_J)	Semimajor Axis (AU)	Separation (arcseconds)	Star Spectral Type	Star Mass ($M_\odot$)	Star Distance (pc)	Star V-Band Magnitude
2M J044144 b	$7.5^{+2.5}_{-2.5}$	15	0.107	M8.5	0.02	140	13.72[b]
2M1207 b	4^{+6}_{-1}	46	0.878	M8	0.025	52.4	20.15
AB Pic b	$13.5^{+0.5}_{-0.5}$	275	6.031	K2	$\sim$0.76[b]	45.6	9.16
beta Pic b	8^{+5}_{-2}	8	0.415	A6	1.8	19.3	3.86
CT Cha b	17^{+6}_{-6}	440	2.667	K7	$\sim$0.6[c]	165	12.36
Fomalhaut b	$3^{+0.5}_{-1.3}$	115	14.935	A3	2.06	7.7	1.16
GQ Lup b	$21.5^{+20.5}_{-20.5}$	103	0.736	K7e	0.7	140	11.4
HR 8799 b	7^{+4}_{-2}	68	1.726	A5	1.5	39.4	5.96
HR 8799 c	10^{+3}_{-3}	38	0.964	A5	1.5	39.4	5.96
HR 8799 d	10^{+3}_{-3}	24	0.609	A5	1.5	39.4	5.96
SCR 1845 b	9 - 65	4.5	1.169	M8.5	$\sim$0.08[d]	3.85	17.4
UScoCTIO 108 b	14^{+2}_{-8}	670	4.621	M7	0.057	145	15.07[e]

[a]Unless otherwise noted, all parameters and list of confirmed planets are from `www.exoplanet.eu`.
[b]Mass for AB Pic is estimated from the masses of other K2 stars reported by (Popper 1993).
[c]Mass for CT Cha is estimated based on stellar masses and spectral types listed in Appendix G of Carroll & Ostlie (2007).
[d]Mass for SCR 1845 is estimated from the M dwarf mass models derived by Baraffe & Chabrier (1996).
[e]H-band magnitude is given for 2M J044144 b and UScoCTIO 108 b.

1.2.6 Summary of Planetary Detection Methods

As discussed in Sections 1.2.1 - 1.2.5, each planet detection technique has strengths and disadvantages. Radial velocity surveys are ideal for detecting massive planets in relatively close orbits, but they cannot provide information about the planetary radius or inclination. Transit surveys provide the means to determine the radius and inclination of planets in short-period orbits, but they require precise alignment of the observer, planet, and star. Astrometry provides another way to determine the inclination of an orbit, but due to the high precision required for astrometric measurements, astrometry has not yet led to the discovery of any confirmed planets. Until the precision of astrometric surveys improves, microlensing, direct detection, and long-baseline radial velocity surveys are the only techniques that allow observers to probe the outer regions of stellar systems. Microlensing is sensitive to a phenomenal range of planetary masses and semimajor axes, but because microlensing events do not repeat, these planets cannot be re-observed. Current direct imaging surveys are only sensitive to massive planets, but re-observations of direct imaging targets constrain all of the orbital parameters, and spectroscopic observations can provide information about the planet's atmospheric structure and composition.

Although the vast majority of planets have been detected by radial velocity measurements, other methods have been increasingly successful in recent years. Additionally, the rate of planet detections is steadily increasing. Figure 1.4 displays the mass of all exoplanets discovered after 1995 as a function of discovery year. In addition to revealing that exoplanet detection techniques are probing smaller and smaller masses, the increasing density of points in the figure as time passes emphasizes the higher frequency of planet discoveries today compared to ten years ago. As time continues, the increasing sensitivity of planet detection surveys will result in the detection of even smaller planets.

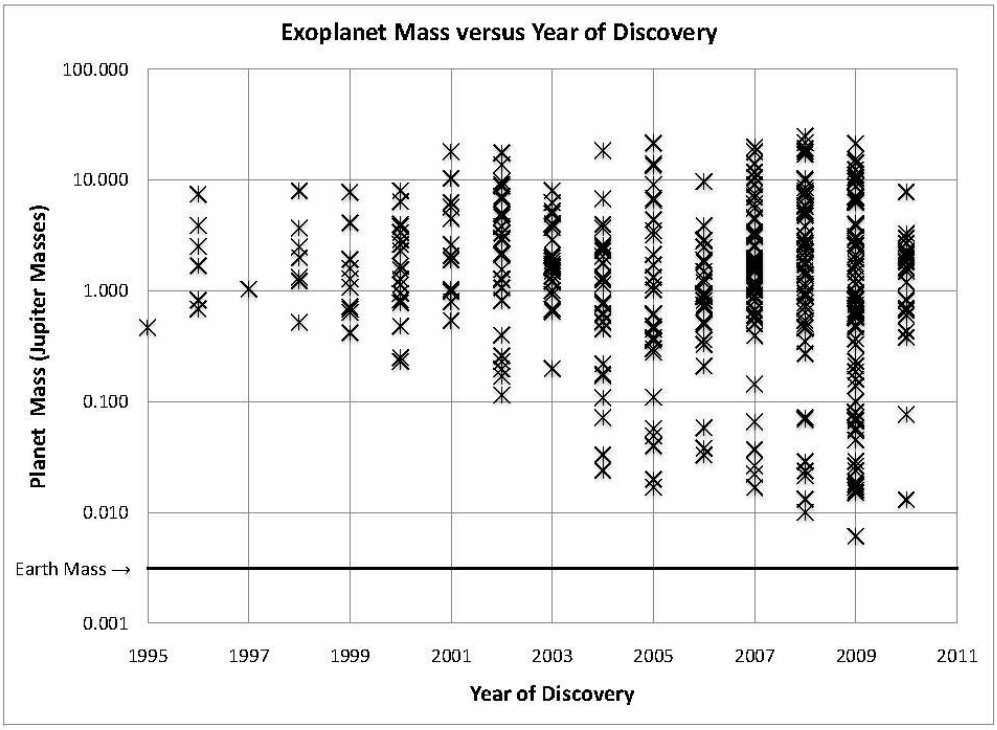

Figure 1.4: Exoplanet mass as a function of discovery year. Note both the trend toward smaller planets and the increase in the number of planet detections in recent years. The planet masses and discovery years were obtained from `www.exoplanet.eu`.

1.3 Exoplanet Demographics

Although each of the methods currently used to detect extrasolar planets introduces a strong selection bias, we can infer some general properties of extrasolar planets. For instance, we find that the eccentricity distribution of exoplanets is much more shifted toward higher eccentricities than would be expected by looking at our solar system. As shown in Figure 1.5, the average eccentricity of extrasolar planets is 0.2, and 11% of planets have eccentricities greater than 0.5. For comparison, the average eccentricity of the eight planets in our solar system is 0.068, and even the eccentricity of Pluto is only 0.244.[15] However, even though some extrasolar planets likely do have eccentricities much greater than the eccentricities of the planets in our solar system, Shen & Turner (2008) point out that eccentricity measurements converge toward the true value from above. Consequently, estimates of the eccentricities of exoplanets may be biased toward artificially high values until more observations are obtained at higher signal-to-noise levels.

Drawing conclusions about the mass distribution of extrasolar planets is even trickier than charactering orbital eccentricity because the current detection methods are much more sensitive to massive planets. Looking at the planets detected serendipitously by microlensing, which is the least biased of the detection methods (Gaudi 2010), we see that the median mass of planets detected via microlensing is 0.25 $M_{\rm J}$. In contrast, the median $M\sin i$ mass of planets detected via radial velocity surveys is 1.6 $M_{\rm J}$ and the median mass of all detected exoplanets is 1.5 $M_{\rm J}$. Figure 1.6 displays the range and median of planetary masses detected by each of the most common planet detection methods. As illustrated in Figure 1.6, the apparent mass distribution varies greatly depending on the particular detection method. Accordingly, accurate estimations of the true mass distribution of exoplanets must include a detailed treatment of the detection biases and sensitivities of each of the detection

[15]Based on planetary statistics at `http://nssdc.gsfc.nasa.gov/planetary/factsheet/`

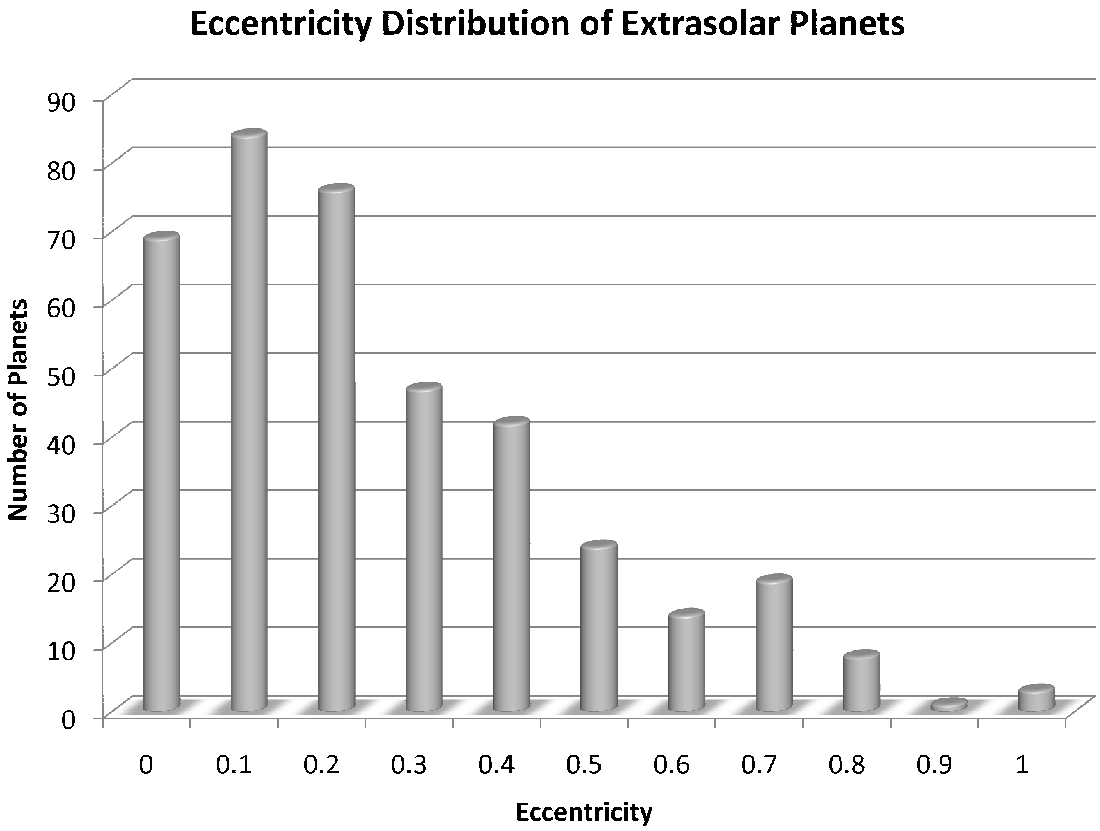

Figure 1.5: Eccentricity distribution of exoplanets detected as of April 4, 2010. All data were acquired from `exoplanet.eu` and only planets with measured eccentricity were included in the plot. The distribution peaks at moderate eccentricities ($\sim$0.1), but there is a significant tail toward higher eccentricities.

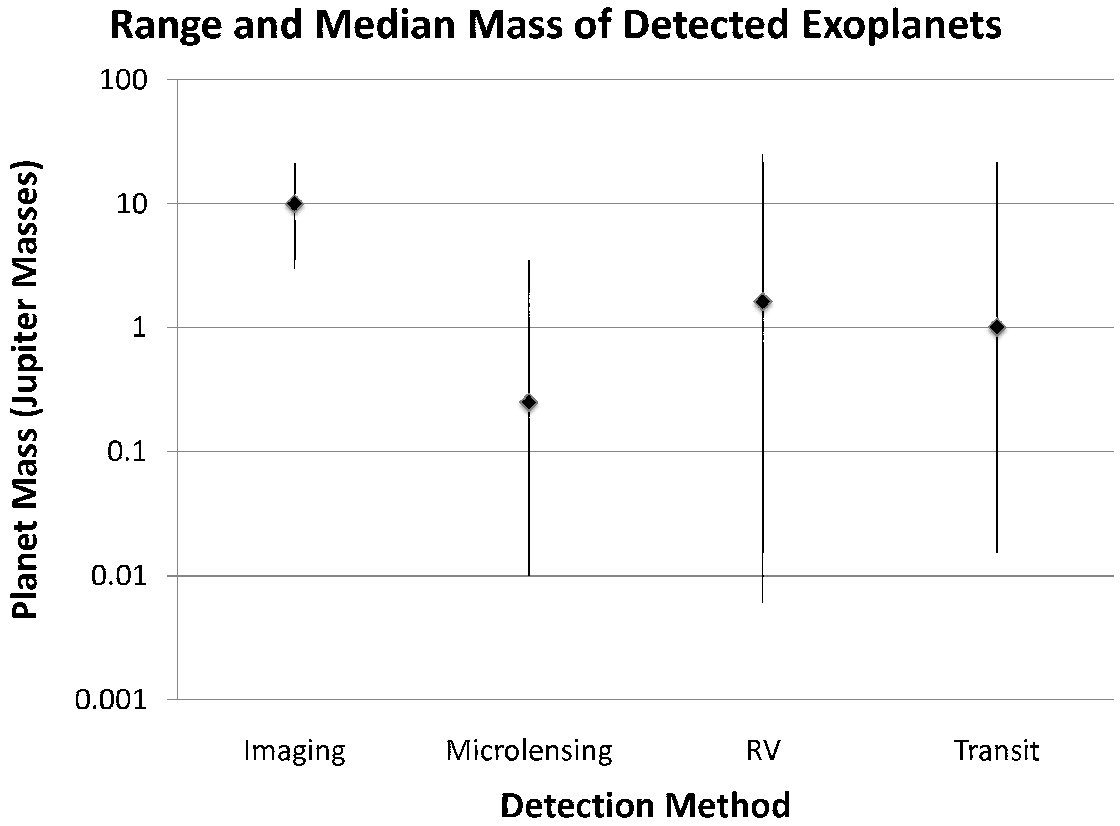

Figure 1.6: Full range and median mass of known exoplanets categorized by detection method. The diamonds indicate the median mass of the planets detected by each method and the lines indicate the full range of detected masses. All data for this figure were acquired from `exoplanet.eu`.

methods rather than naively inferring that the detected distribution of exoplanets is representative of the full population of exoplanets.

While constraining the global properties of exoplanets is difficult because of the strong influence of the detection biases, the existing census of exoplanets is large enough to identify several key types of planets. Beginning in our own solar system, we identify two distinct classes of planets:

1. **Rocky Terrestrial Planets:** Mercury, Venus, Earth, and Mars display a range of atmospheric compositions, but all four worlds have rocky surfaces and differentiated cores. The masses of the inner planets range from 0.33×10^{24} kg to 5.97×10^{24} kg ($1.7 \times 10^{-4} - 3.1 \times 10^{-3} M_{\rm J}$) as shown in Table 1.2 and their

Table 1.2: Properties of Rocky Planets

Planet	Mercury	Venus	Earth	Mars
Mass ($M_\oplus$)	0.055	0.815	1	0.642
Equatorial Radius (km)	2439.7	6051.8	6378.1	3396.2
Density (kg/m^3)	5427	5243	5515	3933
Semimajor Axis (AU)	0.387	0.723	1	1.524

Table 1.3: Properties and Atmospheric Composition of Jovian Planets

Planet	Jupiter	Saturn	Uranus	Neptune
Mass (M_J)	1	0.299	0.046	0.054
Equatorial Radius (km)	71492	60268	25559	24764
Semimajor Axis (AU)	5.204	9.582	19.201	30.047
Molecular Hydrogen (H_2)	89.8%	96.3%	82.5%	80.0%
Helium (He)	10.2%	3.25%	15.2%	19.3%
Methane (CH_4)	3000 ppm	4500 ppm	2.3%	1.5 %
Ammonia (NH_3)	260 ppm	125 ppm	-	-
Hydrogen Deuturide (HD)	28 ppm	110 ppm	148 ppm	192 ppm
Ethane (C_2H_6)	5.8 ppm	7 ppm	-	1.5 ppm
Water (H_2O)	4 ppm	-	-	-

average density is 5030 kg/m^3.[16] None of the planets have ring systems, but Earth and Mars both have moons.

2. **Gaseous Jovian Planets:** The four outer planets of our system are all balls of gas that might be considered more similar to the Sun than to the terrestrial planets. Jupiter and Saturn, the two innermost Jovian planets, are almost entirely hydrogen and helium, and are referred to as "gas giants." The outermost planets, Uranus and Neptune, also contain significant amounts of methane and have been named "ice giants." The compositions of the Jovian planets are shown in Table 1.3. Note that Saturn has a higher percentage of hydrogen than all of the other Jovian planets and is consequently much less dense than Jupiter despite having a similar radius ($M_\mathrm{S} = 0.3M_\mathrm{J}, R_\mathrm{S} = 0.84R_\mathrm{J}$).

Prior to the detection of exoplanets, scientists inferred from the properties of our

[16]NASA Planetary Fact Sheet: `http://nssdc.gsfc.nasa.gov/planetary/factsheet/`

solar system that other planetary systems would look much like ours and feature close-in terrestrial planets and more distant Jovian planets. Surprisingly, scientists instead found systems in which objects more massive than Jupiter orbited at separations much smaller than the orbit of Mercury. These worlds became known as "Hot Jupiters," and raised scores of questions about planet formation and migration. Many of the earliest planets detected were Hot Jupiters, but the advent of microlensing and direct imaging surveys and the increased sensitivity of radial velocity and transit surveys led to the discovery of gaseous planets at larger separations (like the Jovian planets in our solar system) as well as higher-density worlds with masses a few times larger than the mass of Earth (Beaulieu et al. 2006). This new class of planets became known as "Super-Earths," under the assumption that their higher density might be attributed to a rocky core (Valencia et al. 2007).

The newest additions to the remarkably diverse collection of exoplanets are the massive planets detected by direct imaging surveys in extremely wide orbits. As discussed in Section 1.2.5, direct imaging surveys are most sensitive to young, hot Jovian planets in orbits with semimajor axes of tens to hundreds of AU. The discovery of such massive planets greater than 100 AU from their host star (Chauvin et al. 2005; Neuhäuser et al. 2005; Béjar et al. 2008; Kalas et al. 2008; Schmidt et al. 2008) confounded planetary theorists because the timescales for accretion in the outer disk were too long to form planets at such large radii under the currently accepted core-accretion formation theory (e.g., Kratter et al. 2010). Since the planets clearly exist, theorists have been forced to modify planetary formation theories to account for the formation of widely-separated Jovian planets in addition to Hot Jupiters, Super-Earths, and "conventional" Cold Jupiters and inner terrestrial planets like those found in our solar system. The current planet formation theories, including the leading core-accretion model, are discussed in detail in Chapter 2. Section 2.2 focuses specifically on the problem of forming massive planets at large orbital radii.

Chapter 2

Planet Formation and Evolution

Astronomers, geologists, philosophers, and theologians have been contemplating the formation of the Earth and planets for millenia, but the fascinating success of exoplanet searches drastically complicated the field of planetary formation. Not only did planetary scientists have to explain terrestrial planets and Jovian planets, they also had to develop formation theories for Super-Earths (Rivera et al. 2005), Hot Jupiters (Mayor & Queloz 1995), and a whole slew of previously unimagined planets. The formation theories for all of these classes of planets are intriguing, but this Chapter will address only giant planet formation theories because terrestrial planets are currently beyond the detection limit of direct imaging surveys. For an introduction to terrestrial planet formation, see Kenyon & Bromley (2006), Kokubo et al. (2006), and Raymond et al. (2006). The leading theories of giant planet formation are introduced in Section 2.1 and the specific application of these theories to the formation of giant planets in widely separated orbits is discussed in Section 2.2. The evolution of giant planets after formation is reviewed in Section 2.3.

2.1 General Models of Giant Planet Formation

In addition to confirming that planetary formation is possible around other stars, the discovery of 443 additional planets[1] increased the number of worlds with which theorists could verify their models of planet formation by a factor of 50. Although the issue of giant planet formation is still unresolved, the influx of data from planet detection surveys has allowed theorists to develop two main models of planet formation: core accretion and gravitational instability. Both methods are described in detail in Sections 2.1.1 and 2.1.2, respectively. While core accretion is considered the leading model for planet formation, the diversity of exoplanets suggests that real planet formation involves a combination of both models. For instance, Matsuo et al. (2007) finds that 90% of all planets can be explained by the core accretion model of planet formation, but that the remaining 10% must have been formed through gravitational instability.

2.1.1 Core Accretion

The core accretion theory of planet formation was advanced by Mizuno (1980), Bodenheimer & Pollack (1986), and Pollack et al. (1996) and is currently the leading theory for giant planet formation. Under the core accretion theory, giant planet formation follows the following steps:

1. Small micron-scale dust grains in the protoplanetary disk collide and stick together to form kilometer-scale planetesimals.[2] Inside the Hill radius of the planetesimal, the gravitational influence of the planetesimal is stronger than the gravitational influence of the star, causing additional particles to accrete onto the growing planetesimal (Lissauer 1993). The Hill radius h of a planetes-

[1] Number of planets listed on `exoplanet.eu` on April 5, 2010.

[2] Actually, the evolution from centimeter-scale objects to kilometer-scale planetesimals is still unclear. See Levison et al. (2010) for a recent review of the problem.

imal of mass M in an orbit with semimajor axis a around a star of mass M_* is given by

$$h = \left(\frac{M}{M_*}\right)^{1/3} a \ .$$

2. The planetestimals collide to form a solid core approximately $10\,\mathrm{M}_\oplus$ in mass.

3. The rocky core accumulates a thin coating of gas.

4. The cooling gas condenses onto the solid core.

5. The core achieves critical mass and runaway gas accretion onto the core begins. The core continues to accumulate dust as well as gas, but the rate of gas accretion is much higher than the rate of dust accretion.

6. The planet collects gas and dust from the surrounding area until the disk dissipates. The typical timescale for disk dissipation is $\lesssim$10 Myr (Hillenbrand 2008).

According to the core accretion model, the final mass of the planet is limited by the relative rate of gas accretion into the core compared to the disk dissipation time or the time required for the planet to clear a hole in the disk so that no gas can reach the planet even though the rest of the disk still exists. Since the core mass must reach a critical threshold before runaway gas accretion begins, the time required to form the solid core also influences the final size of giant planets. The timescale for core formation decreases as the abundance of grains in the protoplanetary disk increases, so metal cores are expected to form more quickly around high-metallicity stars than around low-metallicity stars (Ida & Lin 2004; Alibert et al. 2004). Initial results confirm that the likelihood of planet detection increases with stellar metallicity (Gonzalez et al. 2001; Santos et al. 2001, 2004, 2005; Reid 2002; Fischer & Valenti 2005), and surveys of planet frequency as a function of stellar mass (Lovis & Mayor 2007; Johnson et al. 2007) also reveal that higher-mass stars are more likely to host

planets than low-mass stars. Both results are consistent with expections from numerical simulations of planet formation via core accretion (Ida & Lin 2004; Kornet et al. 2005; Benz et al. 2006).

2.1.2 Gravitational Instability

While core accretion theory easily supports the formation of the Jovian planets in our solar system (Benvenuto et al. 2009) and most exoplanets (Ida & Lin 2004), planets in the extreme outer reaches of a stellar system ($\gtrsim$100 AU) must be formed by another mechanism because the timescale for core accretion at those radii exceeds the timescale for gas depletion in the disk (Kenyon & Bromley 2008). The leading alternative method of planet formation is the gravitational instability theory introduced in Boss (1997). In the gravitational instability model, massive planets are formed directly from the fragmentation of the protoplanetary disk without a solid accretion phase. The timescale for planet formation via gravitational instability is significantly shorter than the timescale required for core accretion, so planets formed by gravitational instability can grow to several Jupiter masses before disk dissipation even at large orbital radii (Stamatellos & Whitworth 2008). The disadvantages of the gravitational instability model are that it does not predict the increased frequency of planets observed around stars of higher metallicity (Boss 1997) and it cannot be used to explain planet formation at orbital radii $\lesssim$100 AU because the gas in the inner regions of the disk will not be able to cool sufficiently to form giant planets on the required timescale (Rafikov 2005; Matzner & Levin 2005).

2.2 Planet Formation on Wide Orbits

Section 2.1 introduced the leading theories of giant plant formation and emphasized that core accretion is currently the leading planetary formation theory. However,

massive planets at extremely wide separations ($\gtrsim$100 AU) pose a challenge to core accretion theory because the timescale for core accretion at those radii is longer than the gas depletion timescale of the disk (Kenyon & Bromley 2008). The first detections from direct imaging surveys introduced a whole new category of giant planets in orbits with semimajor axes $\gtrsim$ 100 AU (e.g., Chauvin et al. 2005) and challenged planetary theorists to adapt their models of planet formation to produce massive planets at large radii. The question of how planets can exist at such large separations from their host stars is still under investigation, but the influx of data from direct imaging surveys and the concentrated efforts of theorists have helped clarify the process.

For example, Dodson-Robinson et al. (2009) conducted numerical simulations of planet formation and determined that the only way to create massive planets in stable orbits at wide separations was to form the planets from gravitational instabilities. However, they did not rule out the possibility that the planets detected by direct imaging surveys were formed in the inner disk and were now in the process of being scattered from the inner disk to the outer disk. Consequently, Dodson-Robinson et al. (2009) encourage observers to search for planets around a wide age-range of host stars to determine whether exoplanets are more likely to be detected around younger stars even after controlling for the decreased brightness of older planets. If observers discover that the corrected detection rate is lower for older stars then for younger stars, then the planets detected in imaging surveys are likely scattering outward from the inner disk. Since the planets will be scattered into unstable orbits, they will only remain in the outer disk for a finite period of time and they will therefore be noticeably absent in older systems. On the other hand, if observers discover that the corrected detection rate is the same for main-sequence stars of all ages, then Dodson-Robinson et al. (2009) are likely correct that Jovian planets on wide orbits are formed due to gravitational instabilities.

2.3 Giant Planet Evolution

The sensitivity of direct detection planet surveys is directly related to the luminosity of exoplanets as a function of age. Shortly after formation, planets are hot because the gravitational potential energy of the planetesimals that formed the planet has been converted to thermal energy (de Pater & Lissauer 2001). As time passes, planets become cooler and less luminous because they are not massive enough to generate additional energy by fusing hydrogen or deuterium.

While theorists agree that planets should decrease in temperature as they age, the exact temperature evolution of young Jovian planets is still not well understood. Early models of exoplanet formation (e.g. Burrows et al. 1997) initiated their models using a generic "hot start" condition and then allowed the models to relax according to the equations of state and thermodynamic laws of the system. Since the theorists were interested in planets much older than the relaxation time of their models, the exact initial conditions of the model were not a concern. However, relying on hot start models of planet evolution to determine the temperatures of young planets can lead to problems because the models may still remember the hot start initial condition.

For example, Figures 2.1 and 2.2 display two models of planetary luminosities as a function of mass and age. Figure 2.1 is from the hot start model of Burrows et al. (2001) and displays the luminosities of low-mass stars, brown dwarfs, and jovian planets for ages of 1 Myr to 1 Gyr. According to the (Burrows et al. 2001) model, a 1 M_J planet will have a luminosity of $\sim 10^{-5}\,L_\odot$ at an age of 1 Myr and a much fainter luminosity of $\sim 5\times10^{-10}\,L_\odot$ at an age of 1 Gyr. In comparison, a 13 M_J object near the brown dwarf/planet boundary will have a rather bright luminosity of $\sim 5\times10^{-3}\,L_\odot$ at 1 Myr and a luminosity of $\sim 5\times10^{-8}\,L_\odot$ at 1 Gyr. Current direct detection limits can achieve contrasts of approximately 10^{-6} at 1" separations (Biller et al. 2010), and are therefore sensitive to 1 M_J planets younger than $\sim$20 Myr if the Burrows et al. (2001) models can be applied to young planets.

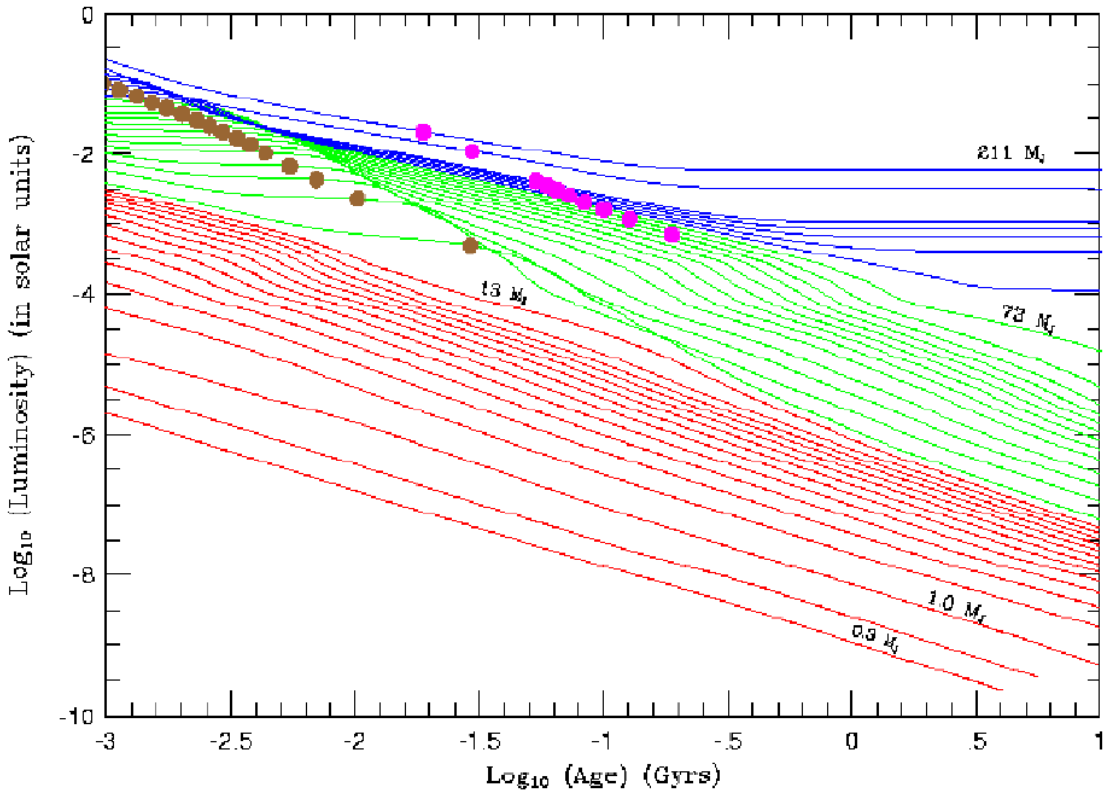

Figure 2.1: Planetary evolution models from Burrows et al. (2001). The blue, green, and red lines indicate the luminosity in units of solar luminosity for stars, brown dwarfs, and giant planets, respectively, as a function of age in Gyrs. The ages at which 50% of the deuterium has burned are indicated by gold dots, and the ages at which 50% of the lithium has burned are indicated by magenta dots. For the masses of all of the objects shown in the plot, see Burrows et al. (2001).

The cooling curves produced by Fortney et al. (2008b) and Marley et al. (2007) lead to more pessimistic results for direct detection surveys. Rather than begin with the conventional hot start model, Fortney et al. (2008b) and Marley et al. (2007) initiate their models using input from the core-collapse model of planet formation discussed in Section 2.1.1. The resulting planetary luminosities, which are displayed in Figure 2.2 are initially much fainter than those predicted by Burrows et al. (2001) but converge with the Burrows et al. (2001) model when the planets reach an age of $\sim$1 Gyr. According to the Fortney et al. (2008b) cooling curves, the luminosity of a 1 M_J planet is barely above the current 10^{-6} detection limit at ages as young as 3 Myr.[3] Even planets with masses of 10 M_J have luminosities below $10^{-5}\,L_\odot$ at an age of 3 Myr.

While observers hoping to directly image exoplanets will be significantly more successful if the Burrows et al. (2001) models are more accurate than the Fortney et al. (2008b) models, both models are still under consideration. Ideally, spectra and photometry from high contrast imaging detections will help constrain models of planetary evolution by providing information about the number of planets detected around stars of a given age. Relying on direct imaging surveys to constrain models of the early stages of planet evolution is complicated by the fact that many other aspects of exoplanet populations are also unknown. For instance, astronomers cannot know a priori whether they failed to detect a planet around a star because the planet was fainter than their detection limit or because there are no planets in orbit around that star. Within the next decade, however, the combined results of direct detection surveys, long-baseline radial velocity surveys, and high-precision astrometry surveys may provide a better census of long-period jovian planets that can then be used to constrain models of planetary evolution.

[3]As explained in the caption of Figure 2.2, the time shown in the x-axis of the figure is the time since formation. Because planet formation via core accretion requires $\sim$2.3-3 Myr, the planets initiated using the core accretion model are actually $\sim$2.3-3 Myr older than the x-axis suggests.

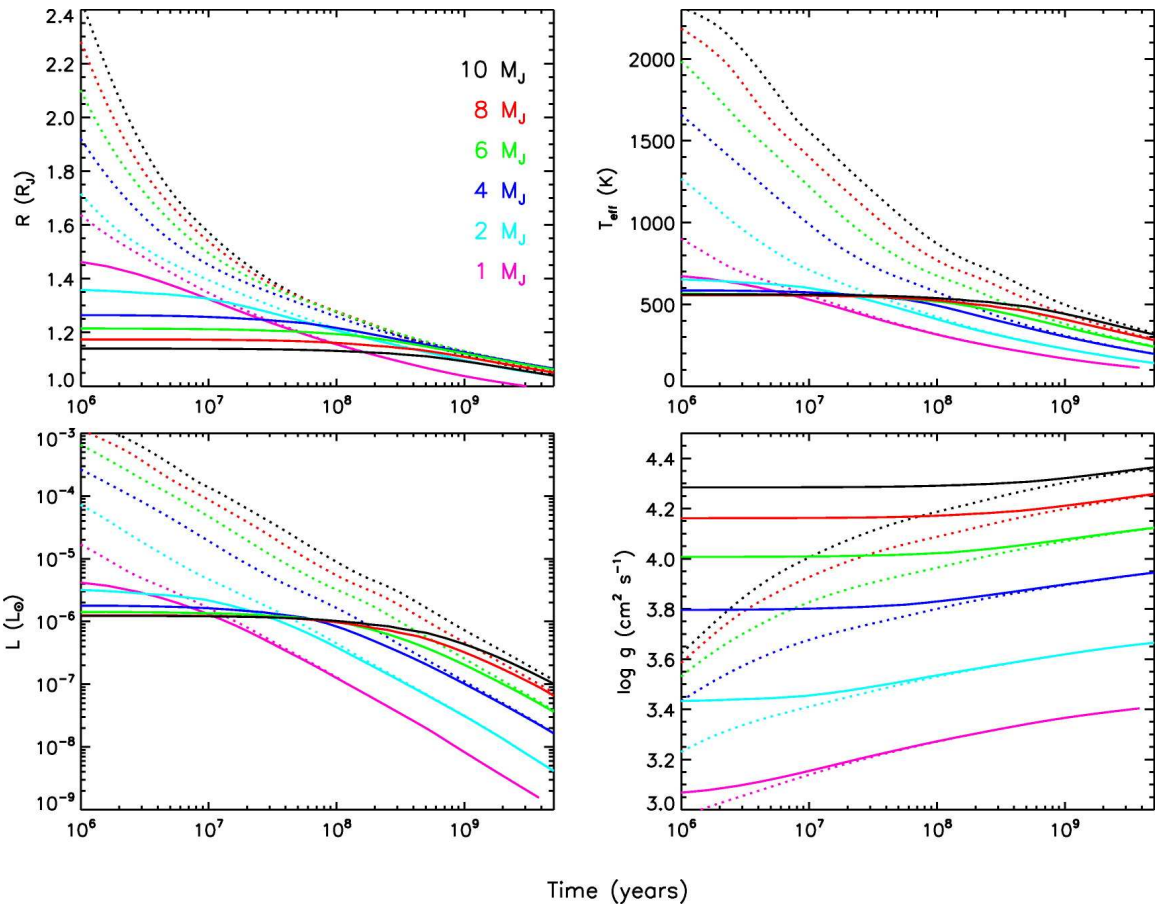

Figure 2.2: Planetary evolution models from Fortney et al. (2008b). In all four plots, the dotted lines display the evolution of planets initiated using a hot start model while the solid lines display the evolution of planets that were initated using the core accretion model from Hubickyj et al. (2005). The time given on the x-axis represents time since formation. The hot start planets are assumed to form instaneously, but the core accretion planets require ∼2.3-3 Myr to form. Accordingly, the ages for the core accretion planets should be adjusted upward by ∼2.3-3 Myr. **Top Left:** The radius evolution of giant planets as a function of age and mass. Note that the planets initiated with the hot start model have much larger initial radii than the planets initiated using the core accretion model. **Top Right:** The temperature evolution of giant planets as a function of age and mass. The hot start planets have a wide range of initial temperatures from 900 K to 2300 K, but all of the core accretion planets have cooler temperatures between 500 K and 700 K. **Bottom Left:** The luminosity evolution of giant planets as a function of age and mass. The core accretion planets are initially much fainter than the hot start planets and display less variation in luminosity as a function of mass. **Bottom Right:** The specific gravity evolution as a function of age and mass.

Chapter 3

High Contrast Imaging

As discussed in Chapter 1, the current frontier of exoplanet investigations lies in direct imaging. Since planets are many orders of magnitude fainter than their host stars, the process of acquiring direct images of exoplanets is classified as "high-contrast imaging" because of the large dynamic range required to detect both a bright star and its faint planetary companion. For comparison, the contrast ratio that would be required to observe Jupiter in its current orbit around the Sun from a distance of 10 pc is approximately 10^8 (Oppenheimer & Hinkley 2009), which is the roughly the same contrast as that required to spot a 1 μm long bacterium of *Vibrio cholerae* (Wachsmuth et al. 1994) on top of the 110.6 m tall Saturn V rocket that carried astronauts to the Moon (O'Connor 1966).

As an added difficulty, an exoplanet in a Jupiter-like orbit would be separated from its host star by only $\sim$5 AU. Even if this system were relatively close to Earth ($\sim$30 pc), the two objects would be separated by only $\sim$0.2 arcseconds. Given that the atmosphere blurs point-sources into disks $\gtrsim$0.5 arcseconds across (Racine 1989), astronomers must either conduct high-contrast observations of exoplanets from space or implement a means of correcting for the distortion created by the atmosphere. While avoiding the atmosphere entirely and conducting observations from space might

seem like a clear choice, the high cost of launching material into space means that space-based telescopes are typically much smaller than ground-based telescopes. For instance, the Hubble Space Telescope mirror is only 2.4 m across (Bahcall & Spitzer 1982), but the ten largest ground-based telescopes have apertures between 8.2 m and 10.4 m.[1] Recall that the diffraction limit of a telescope is given by the Rayleigh criterion:

$$\sin\theta = \frac{1.22\lambda}{D} \ , \tag{3.1}$$

where λ is the wavelength of the light observed, D is the telescope diameter, and θ is the minimum observable angular separation (Newton 1718). Accordingly, for near-infrared light at 1μm, the diffraction limit of the Hubble Space Telescope is 0.1" while the diffraction limit of an 8.2 m telescope is 0.03." Assuming that adaptive optics technology can be used to counter the $\sim$0.5" blurring caused by the atmosphere, the larger aperture of a ground-based telescope allows observers to study objects at higher angular resolutions. A second reason to develop adaptive optics technology to directly image exoplanets on the ground is that observing time on space-based facilities is expensive and difficult to acquire. Although this is not a scientific constraint, it is incredibly relevant to exoplanet direct imaging studies in which large surveys with extensive follow-up observations are necessary.

Now that the rationale for conducting direct imaging studies using ground-based telescopes has been established, we must consider the technology and techniques required to achieve the high contrast ratios necessary to directly image exoplanets. Assuming that the sky is clear, ground-based observers hoping to conduct high-contrast observations face two fundamental issues:

1. Atmospheric turbulence will distort point-sources into disks approximately 0.5" FWHM even in the case of perfect telescope optics.

[1] `http://astro.nineplanets.org/bigeyes.html`

2. Telescope optics are never perfect.

As hinted at earlier in this section, adaptive optics techniques can be used confront the first problem by applying a correction to the distorted wave front as it enters the system. The resulting image will be much cleaner than the image produced without adaptive optics correction, but the second issue still stands. Although astronomers are continually attempting to improve telescope optics and adaptive optics to reduce instrumentally-induced noise and residual wave-front error, astronomers have also developed specialized observing techniques that exploit the characteristic properties of speckles to remove them during image processing. These speckle suppression techniques will be discussed in Section 3.2 following the introduction to adaptive optics presented in Section 3.1

3.1 Adaptive Optics

Astronomers have been battling against the clouds and atmospheric turbulence since the dawn of astronomy, but only within the last two hundred years have telescopes and detectors evolved to the point where the distortions caused by the atmosphere exceed the distortion introduced by telescope optics. Thanks to the ingenuity of modern telescope designers, modern telescopes mirrors are perfectly shaped and polished to within 1 nm (ter Horst et al. 2008) and are covered by special coatings that significantly improve reflectivity (e.g., Shectman et al. 2009). Coupled with the parallel advances in detector technology and automated guiding systems, the advances in mirror technology have allowed astronomers to produce better images than ever before. The early telescopes of the Renaissance allowed Galelio to discover the moons of Jupiter (Galileo Galilei 1610); precision-manufactured, computer-guided telescopes have allowed modern planet hunters to directly image much more distant worlds (Mayor & Queloz 1995).

Even with the finest telescope in the world, however, conducting high contrast observations of exoplanets would be nearly impossible without the use of adaptive optics technology to correct for the blurring of the atmosphere. Although planets at extremely wide separations might be detectable, the ∼0.5" blurred disk of the star would conceal the inner 15 AU of the system for a target at a distance of 30 pc. For a system at 200 pc the situation is even worse: the inner 100 AU would be blocked by starlight. For comparison, the semimajor axes of Jupiter and Pluto are 5.2 AU and 39.4 AU (Newburn & Gulkis 1973), respectively, so planetary scientists are particularly interested in studying planet formation and morphology at the separations that would likely be blocked by an atmospherically-distorted PSF. To make matters worse, the quoted ∼0.5" disk refers only to the FWHM of the stellar PSF. In reality, light from a bright target star can interfere with the detection of planets out to several Airy disk radii.

3.1.1 History of Adaptive Optics

While high-contrast imaging of exoplanets has provided additional motivation for adaptive optics research in recent years, the concept of adaptive optics was first proposed in 1953 (Babcock 1953), well before the existence of exoplanets was confirmed. Babcock realized that atmospheric distortions might be removed by monitoring the incoming wave front for distortions and then altering the shape of a controlling element at the image-plane to introduce perturbations in the opposite direction to restore the wavefront to its initial, undistorted shape. Several years later, Russian scientist Vladimir Pavlovich Linnik independently developed the concept of adaptive optics and also suggested that astronomers could create artificial guide sources by placing a light beacon at 8-10 m altitude in the atmosphere (Linnik 1957). Although 1950's technology was not advanced enough to successfully implement Babcock's and Linnik's proposals, their work laid the foundation for modern adaptive optics. Unfor-

tunately, Linnik's work was not translated into English until 1994 (Linnik 1994), so many English-speaking scientists believed that the concept of an artificial guide star was first proposed by Foy & Labeyrie (1985) .

Despite the promise of adaptive optics for astronomy, the American and Soviet militaries were the first groups to actively utilize adaptive optics during the 1960s and 1970s (Max 2001). Rather than improve images of space taken from the ground, the militaries relied on adaptive optics technology to enhance their satellite images of each other's territory and to refine missile guidance systems (Duffner 2009). Nonetheless, the military AO groups faced many of the same challenges as the astronomical AO teams, and information on military AO systems was highly utilized by astronomers once the information was declassified and released beginning in 1991 (Benedict et al. 1994).

The first astronomical observation using adaptive optics system was completed by Buffington et al. (1977) using the Leuschner and Lick Observatories in California. Despite the 1.5-3" atmospheric seeing at both sights, Buffington et al. (1977) were able to produce diffraction-limited images of Sirius and Arcturus in approximately $^1/_3$ of their observations.

3.1.2 Modern Adaptive Optics Technology

Adaptive optics technology is still rapidly evolving, but modern systems share several basic characteristics because the principle of AO remains the same regardless of the exact system configuration. Since the distortions present in a wavefront must be identified before they can be corrected, a required component in any AO system is a wavefront sensor. Wavefront sensors utilize either charge coupled devices (CCDs)[2] or single avalanche photodiodes (APDs)[3] to monitor the incoming light from a guide

[2]CCDs are visible and infrared light detectors that are commonly used in digital cameras and astronomical instrumentation.

[3]APDs are photodetectors that initiate a cascade reaction when a photon is collected, thus amplifying the signal and allowing the system to count single photons.

star (Downing et al. 2008). Since the atmospheric conditions are constantly changing, the detector must be read out frequently to constantly monitor the disortions present in the wavefront. Based on the signal received from the wavefront sensor, the control computer for the AO system will determine the approriate correction and reshape the deformable mirror to flatten the wavefront (Feldt 2009).

3.2 Speckle Suppression Techniques

Although modern adaptive optics techniques have been incredibly successful in removing most of the atmospheric distortion from astronomical observations, the sensitivity of high-contrast observations is still limited by speckle noise. Unlike the atmospherically-induced speckles that are treated by adaptive optics (Roddier 1981; Racine et al. 1999; Macintosh et al. 2005), the remaining speckles are due to imperfections in the telescope and optics that introduce relatively long-term speckle patterns (Marois et al. 2003, 2005, 2008a; Hinkley et al. 2007; Lafrenière et al. 2007b). While atmospheric speckles typically evolve on timescales between a few milliseconds and ten seconds (Oppenheimer & Hinkley 2009), instrumentally-induced speckles evolve more slowly on minute- or hour-long timescales (Marois et al. 2006; Hinkley et al. 2007) and are therefore referred to as "quasi-static" speckles. Accordingly, although the noise due to random, quickly evolving atmospheric speckles can be reduced by taking a series of exposures and co-adding the frames, the central limit theorem does not hold for the instrumentally-induced quasi-static speckles because the speckles remain correlated between exposures and therefore the quasi-static speckle noise does not add to produce a Gaussian intensity distribution in the composite image (Marois et al. 2008a).

Since most confidence limit estimations rely on Gaussian statistics when calculating the significance of deviations from the expected brightness, the lack of a Gaussian

intensity distribution of quasi-static speckle noise in the final image presents a challenge to scientists attempting to exclude possible planet masses and separations based on a high-contrast observation. In response to this difficulty, Marois et al. (2008a) have developed an alternative method of computing confidence limits by first computing a probability density function for the ratio of pixel intensities in the image to the root-mean-squared value of the noise and then integrating the distribution over the desired detection threshold. Marois et al. (2008a) are therefore able to determine accurate confidence limits for non-Gaussian speckle noise distributions. They report that that images with non-Gaussian noise require detection thresholds $\geq$3 times higher than the detection threshold require for images with Gaussian noise in order to acheive the same confidence limit. This is an important result for high-contrast imaging surveys and demonstrates the importance of conducting rigorous analyses of speckle statistics.

Impressively, Marois et al. (2008a) also report that conducting high-contrast observations using a specialized angular differential imaging mode can result in near-Gaussian noise in the final image. As explained in Section 3.2.1, when observations are acquired in angular differential imaging (ADI) mode, the telescope rotates at a rate that causes the point spread function of the target star to remain fixed while the background field and any possible companions rotate across the field of view. Since the quasi-static speckles are due to imperfections in the telescope and optics, the speckles remain roughly fixed with respect to the stellar PSF and are therefore subtracted out when the individual frames are combined. The background stars and potential companions are preserved during frame subtraction because they lie at a different angular position in each frame. Angular differential imaging is frequently used in high contrast imaging to remove quasi-static noise speckles, and the results of Marois et al. (2008a) indicate that in addition to dramatically improving sensitivity to faint companions, ADI has the added advantage of simplifying the process

of determining confidence limits for high-contrast observations. Interestingly, even though space-based observatories do not have to contend with atmospheric disortion, they are confronted by quasi-static speckle noise due to imperfect optics and spacecraft "breathing," contractions and expansions caused by the differential heating the spacecraft experiences during its day-night cycles. Space-based observers cope with quasi-static speckles by rotating the spacecraft along the telescope axis in a manner similar to a ground-based telescope performing ADI observations (Schneider & Silverstone 2003).

In addition to allowing the field of view to rotate during an observation, astronomers can also reduce the influence of quasi-static speckles by comparing the speckle patterns produced in different spectral channels or polarizations. These high-contrast imaging methods are referred to as spectral differential imaging (SDI) and polarimetric differential imaging (PDI), respectively, and are explained in Section 5.4 along with ADI. All three techniques are currently in use in ground-based, high-contrast contrast planet imaging surveys: ADI: Apai et al. (2007); Janson et al. (2007); Lafrenière et al. (2007a); Artigau et al. (2008); Suzuki et al. (2009), PDI: Kuhn et al. (2001); Brandner et al. (2005); Suzuki et al. (2009), SDI: Biller et al. (2004); Lenzen et al. (2005); Biller (2007); Janson et al. (2007); Artigau et al. (2008); Suzuki et al. (2009); Jenkins et al. (2010).

3.2.1 ADI

As described in Section 3.2, ADI observations achieve high contrast ratios by allowing the field of view (including any possible companions) to rotate across the detector while holding the PSF of the telescope fixed as depicted in Figure 3.1. Since the positions of the speckles in the image plane is fixed for relatively long timescales, the speckles can then be subtracted out when the images are derotated and recombined.

Specifically, the derotated frames are divided into concentric radii as shown in

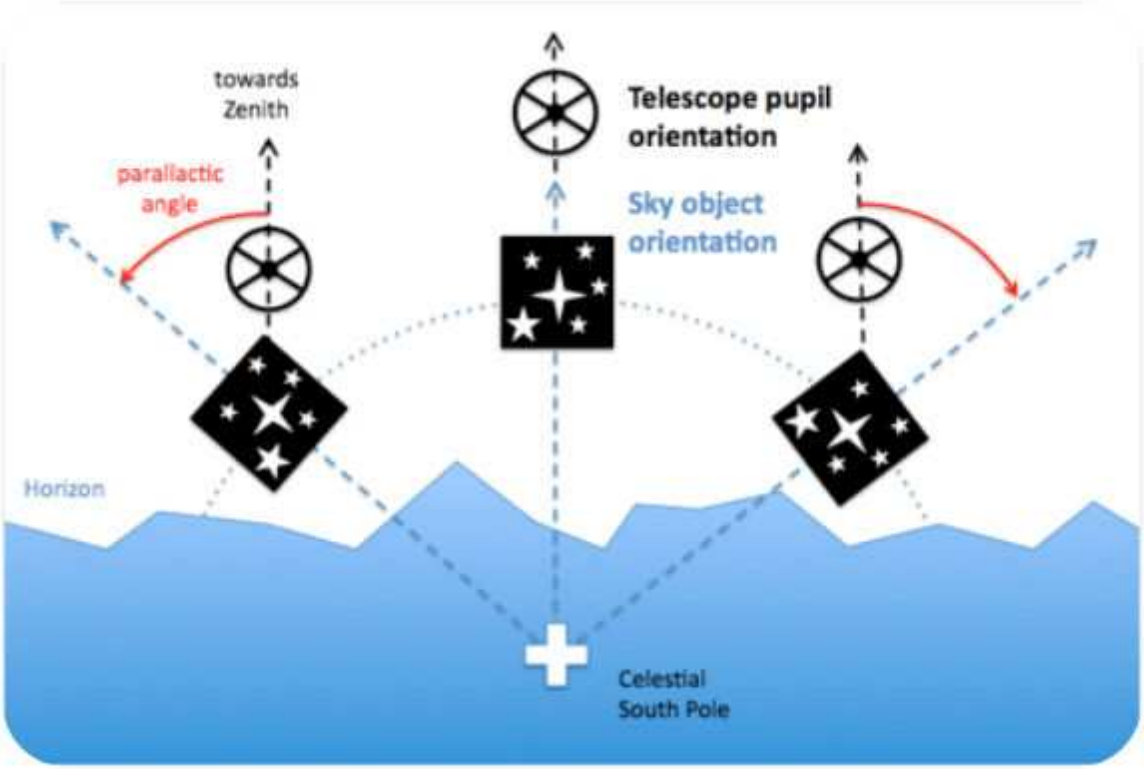

Figure 3.1: In ADI mode the orientation of the telescope pupil remains fixed while any stars or companions rotate in the field of view. Due to the quasistatic nature of speckles, the residual speckle pattern is diminished by subtracting the fixed reference PSF generated from ADI sequence and then derotating the subtracted images. Since ADI only requires specialized tracking, ADI mode may be used in conjunction with spectral differential imaging mode or polarization differential imaging mode. This diagram was prepared by Christian Thalman.

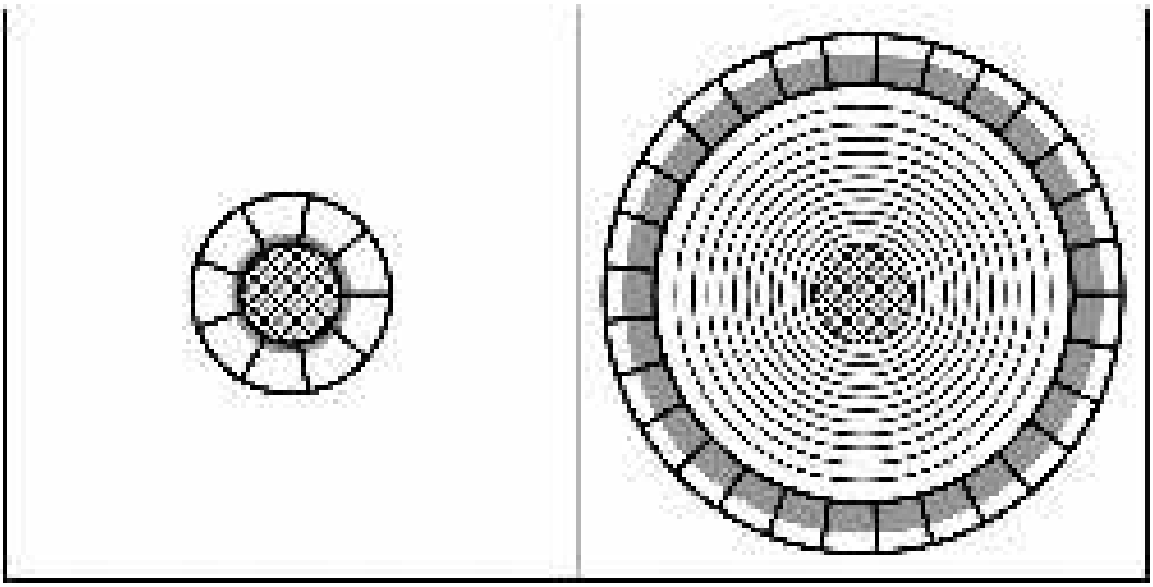

Figure 3.2: Subtraction and optimization regions for LOCI from Lafrenière et al. (2007b). The shaded gray regions are the subtraction regions and the regions separated by thick lines are the optimization regions. The panel on the left displays the subtraction and optimization regions for the first annulus and the panel on the right displays the regions for the thirteenth annulus. In both panels, the circular cross-hatched region at the center indicates the saturated region of the observation.

Figure 3.2 and recombined using the Locally Optimzed Combination of Image (LOCI) algorithm developed by Lafrenière et al. (2007b). Within each annulus, a separate reference image is created for each frame using the frames which have rotated enough that the companion PSF will not be removed during the subtraction process but not so much that the PSF behavior during one of the reference frames is no longer similar to the PSF for the observation.

3.2.2 PDI

In PDI mode, the incoming light is split into beams with different polarizations. Since speckles are due to residual wavefront error and instrumental effect, they are usually unpolarized and can be reduced by subtracting images acquired at two different polarizations (Hinkley et al. 2009). Although the subtraction procedure reduces the intensity of speckles, light scattered from debris disks and protoplanetary disks is

highly polarized and therefore survives the the differencing process. The sensitivity of PDI observations to disks can be further increased by taking a double difference of polarized images acquired at three different polarizations (Hinkley et al. 2009).

3.2.3 SDI

In SDI mode, the target is observed through several different wavelengths simultaneously and then the images are subtracted to remove the speckle noise while preserving the flux from any companion. Accordingly, the bandpasses selected for the SDI filters must be chosen so that the companion flux will not be subtracted along with the speckle noise during the subtraction step. Since the spectra of brown dwarfs and giant planets typically display methane absorption , SDI surveys often utilize filters spanning the CH_4 absorption feature near 1.6μm (Marois et al. 2000).

An added complication of SDI observations is that the speckle pattern scales with wavelength. Thus, simply subtracting the frame acquired from one filter from the frame acquired through a second filter will not remove the speckles. Instead, the frame must be rescaled prior to image subtraction. Since the scaling factor is known, this scaling does not significantly affect observation sensitivity, but variations in the lateral chromatism of the speckle pattern and the overall PSF shape as a function of wavelength can reduce the sensitivity of SDI observations. Conducting SDI observations is therefore a balancing act between selecting filters that are different enough that the planet is substantially brighter in one band relative to the other, and selecting filters at similar enough wavelengths that the speckle pattern is identical in both filters. In order to minimize the amplitude of the speckles that remain after image subtration, astronomers conducting observations in SDI mode often take a double difference so that frames taken at three different wavelengths are used to create the final image. This double difference method greatly reduces the amount of speckle noise in the final image (Marois et al. 2000) and allows SDI observations to

reach contrast levels of $\sim 10^{-4}$(Biller et al. 2006).

Chapter 4

The SEEDS Project

The Subaru Strategic Exploration of Exoplanets and Disks (SEEDS) project is a collaborative effort to improve our understanding of planetary formation, migration, and dynamics. The specific goals of the project are (1) to characterize the frequency and properties of Jovian planets at large (∼5–100 AU) distances from their parent stars; (2) to observe the structure and growth history of protoplanetary and debris disks; and (3) to determine the relationship between massive planets and circumstellar disks. The SEEDS project is sensitive to young giant planets at least as massive as Jupiter and will target both main-sequence stars and white dwarfs within 200 pc of the Sun (Tamura et al. 2004).

4.1 History

Inspired by the improvements in adaptive optics and advances in CCD technology, Dr. Motohide Tamura of the National Astronomical Observatory of Japan (NAOJ) envisoned the Subaru Strategic Exploration of Exoplanets and Disks (SEEDS) project to use a high-contrast instrument and coronagraph on a large telescope to directly image young, hot planets around other stars in the near-infrared. Through collaboration with the Exoplanet Project Office at the NAOJ and the University of Hawaii,

Dr. Tamura submitted a proposal to develope a High Contrast Instrument for the Next Generation Subaru Adaptive Optics (HiCIAO) and install the instrument on the National Astronomical Observatory of Japan's 8.2 meter Subaru telescope on the summit of Mauna Kea in Hawaii (Tamura et al. 2004). The proposal was accepted as the first project under the Subaru Strategic Observation Program, and the team began developing HiCIAO in 2004 (HiCIAO Team 2009). The instrument was delivered to the summit in November, 2007 (Hodapp et al. 2008) and saw first light in December, 2008. Since then, HiCIAO was officially commissioned in October, 2009 and has been used during several observing runs. Unlike the open-use instruments on Subaru which are available to the entire scientific community, HiCIAO is a PI-instrument and Dr. Tamura must approve all proposals to use HiCIAO.

The SEEDS collaboration aims to improve our understanding of planetary formation and diversity by conducting high-contrast observations of several hundred stars that are considered likely to host planets or disks revealing signatures of planet formation. Although the majority of the scientists involved in SEEDS are members of NAOJ, the project is an international collaboration that involves researchers from NAOJ, the Japan Aerospace Exploration Agency, the Graduate University for Advanced Studies (Sokendai), the Max Planck Institute for Astronomy, the University of Hawaii, Kanagawa Universeity, the Tokyo Institute of Technology, Nagoya University, Ibaraki University, the Academia Sinica Institute of Astronomy and Astrophysics, the University of Toronto, the University of Hawaii, the University of Washington, and Princeton University. Due to the involvement of NAOJ, the SEEDS collaboration is open to the entire Japanese community. The lead roles in the project are filled by the Principle Investigator Dr. Tamura, his postdoctoral research assistant Dr. Ryuji Suzuki, and Co-Principle Investigators Dr. T. Usuda and Dr. H. Takami.

4.2 Design Specifications

Since the goal of the SEEDS project is to detect extrasolar planets, the survey needed to be sensitive to planets at very narrow physical separations from the host star. The SEEDS project therefore relies on the HiCIAIO instrument designed by Klaus Hodapp and built by Dr. Suzuki to reduce the inner working angle so that planets can be detected as close to the star as possible. The instrument can be used with or without a coronograph to maximize the sensitivity to faint planets around bright host stars. The engineering details of HiCIAO are discussed in Chapter 5 and the possible observing modes are explained in Section 5.4.

4.3 Target Categories & Goals

During 120 nights over the next five years, the SEEDS project will observe approximately 500 stars from several different categories: nearby stars, moving groups, white dwarfs, young stellar objects, open clusters, and debris disks (Tamura 2009a,b). These categories were designed to maximize the number of planets detected given our current knowledge of exoplanet formation and the capabilities of HiCIAO and the AO188 adaptive optics system (HiCIAO: Critical Design Review 2006). The adaptive optics system, which is explained in detail in Section 5.2, significantly improves the performance of HiCIAO by removing most of the distortion and blurring caused by atmospheric turbulence.

4.3.1 Nearby Stars

The Nearby Stars category is led by Dr. Ryo Kandori, and consists of young ($\lesssim$1 Gyr) stars within 30 pc of the Sun. The Nearby Stars group has created a master target list containing 153 potential targets and expects to observe $\sim$100 of those targets during the next five years (Kandori et al. 2009). Nearby stars are exciting targets for the

SEEDS project because the proximity of these stars to the Earth causes the ∼0.3" inner working angle (IWA)[1] of HiCIAO to correspond to physical separations from the star of only ∼2–9 AU instead of the ∼10–60 AU inner limit typically possible around more distant SEEDS targets. The disadvantage of observing nearby stars is that the population of stars in the solar neighborhood is dominated by older M dwarf stars, so most of the planets in the solar neighborhood are likely old enough that they have cooled to the point that their thermal emission is below the SEEDS detection limit. See Section 2.3 for a review of planetary temperatures and cooling curves as a function of age.

The nearby stars target list is divided into six subcategories. The first subcategory consists of 63 Sun-like F, G, and K stars. Due to the proximity of these stars, this subgroup of Sun-like nearby stars is most likely to yield Jupiter-mass giant planets at Jupiter-like (∼5 AU) separations. Subsequent follow-ups of these target stars with radial velocity or transit searches might then result in the detection of additional inner planets and the first discovery of a true solar system analog with Jovian planets at Jupiter-like separations and terrestrial planets at Earth-like separations.

The second subcategory is the M stars group, which consists of 15 young M stars. The relatively low brightness of M stars makes them an excellent target for direct imaging studies because the contrast required to detect a Jovian planet in orbit around an M star is significantly less than the contrast required to detect a planet around a more massive star at the same distance. Young M stars are also an exciting choice because they have not featured prominently in previous exoplanet searches because their strong coronal activity and large star spots introduce frequent false positives in transit searches and their intrinsic faintness requires large-aperture telescopes (Endl et al. 2003).

[1]The quoted 0.3" IWA for HiCIAO assumes that the 0.3" coronagraphic mask is in use. If a larger mask is used for brighter targets, then the IWA will be greater. Conversely, the IWA might be <0.3" for faint targets observed without a coronagraphic mask.

The third nearby stars subgroup is the Brown Dwarfs subgroup which contains 15 L and T dwarfs (Kandori et al. 2009). The term "brown dwarf" was created by Jill Tarter in her 1975 PhD thesis to describe substellar objects that are too massive to be considered planets, but are not massive enough to fuse hydrogen into helium like stars (Tarter 1975, 1986). These objects were first hypothesized by Kumar (1963), who referred to them as "black dwarfs." Since then, numerous brown dwarfs have been discovered, and astronomers have subdivided them into L and T dwarfs based on their temperatures and spectral features.

Both L and T dwarfs fuse deuterium into helium and can distinguished from late-type M dwarfs by the presence of lithium in their spectra[2] (Rebolo et al. 1992). L dwarfs have masses of $\sim$60 $M_{\rm J}$ and effective temperatures of 1300–2200 K (Martin et al. 1997; Kirkpatrick et al. 1999). Consequently, imaging planets around L dwarfs should be much easier than finding planets around Sun-like stars because L dwarfs are several magnitudes fainter than Sun-like stars. Similarly, the contrast ratio required to detect planets around T dwarfs is much more acheivable than the contrast ratio required to image planets around Sun-like stars because the effective temperature of T dwarfs is only $\lesssim$1300 K compared to the $\sim$6000 K temperatures expected for F, G, and K stars (Kirkpatrick et al. 1999; Geballe et al. 2002). However, while the low luminosity of L and T dwarfs decreases the contrast ratio required to detect exoplanets, most L and T dwarfs (as well as fainter M dwarfs) cannot be observed with the AO system because they are not bright enough (R<14 mag) to serve as natural guide stars. A laser guide star (LGS) system for Subaru is currently undergoing testing, and M, L, and T dwarfs will become popular targets for the SEEDS survey once the LGS system is implemented.

The next subcategory is a group of 30 nearby stars that are already known to

[2]The spectra of young main-sequence stars also contain lithium, but stars burn their supply of lithium within the first 200 Myr of their main-sequence evolution (Burrows et al. 2001), so the presence of lithium in the spectrum of an older object is a good indication that the object is a brown dwarf.

host planets. Since the previously detected planets were detected via radial velocity and transit surveys, the known planets are most likely too close to the star to be seen by direct imaging. However, the radial velocity curves for these stars display long-term variations that could be indicative of additional planets in longer-period orbits (Kandori et al. 2009). The Nearby Stars group will attempt to image those planets in order to improve our knowledge of multi-planet systems.

The fifth nearby stars subgroup consists of thirty A stars. This high-mass stars group was created in order to better understand planet formation around more massive stars. Due to the reduced amplitude of the radial velocity reflex motion for massive stars and the relative lack of spectral lines in high-mass star spectra, A stars are more difficult to observe with radial velocity techniques than Sun-like stars. Achieving the high contrast ratio required to detect planets around such a bright star is also challenging for direct imaging studies, but the A stars chosen by the Nearby Stars group are so close to Earth that even angular separations of 1" only correspond to 30 AU, which is the orbital distance of Neptune.[3] Consequently, even if the brightness of the A star prevents HiCIAO from finding planets <1" from the star, the regions of the system probed by greater angular separations are still interesting for planet detection. Furthermore, half of the directly detected exoplanets orbit A stars (HR8799 bcd: Marois et al. 2008b, Fomalhaut b: Kalas et al. 2008, and beta Pictoris: Lagrange et al. 2009), which is consistent with theories that widely-separated giant planets may be more frequent around massive stars than around Sun-like stars (Kennedy & Kenyon 2008).

The final nearby stars category consists of stars that are likely targets for future space-based planet-finding missions. These targets are the closest F, G, and K stars to the Sun and all lie within 4–13 pc (Kandori et al. 2009). In addition to the Sun-like stars included in the first nearby stars subgroup, this subgroup contains the

[3]http://nssdc.gsfc.nasa.gov/planetary/factsheet/

stars around which the SEEDS project is most likely to find analogs of our own solar system.

4.3.2 Moving Groups

The Moving Groups team is led by Dr. Michael McElwain. The category consists of 40 stars that are associated with stellar moving groups. Moving groups are populations of stars that are dispersed over the sky but share the same velocity through space (Zuckerman & Song 2004). Due to the difficulty of determining the actual space velocity of stars, the identification of moving groups requires high precision astrometric data, such as that acquired by the Hipparcos mission (Dehnen 1998). Despite the accuracy of the Hipparcos data, group membership can not be determined absolutely, so there is only a probability that a given star is associated with a certain moving group. The contour plot in Figure 4.1 displays the major known moving groups in the Milky Way Galaxy. As shown in Figure 4.1 the dominant moving groups in the solar neighborhood are the Arcturus Moving Group, the Coma Berenices Moving Group, the Hercules Moving Group, the Hyades Moving Gruop, the NGC 1901 Moving Group, the Pleiades Moving Group, and the Sirius/Ursa Major Moving Group.

The SEEDS Moving Group target list includes stars from the AB Doradus, Beta Pictoris, Castor, Hercules-Lyra, Tucana Horologium, TW Hydrae, and Subgroup B4 moving groups (McElwain et al. 2009). These stars were chosen because they are bright enough to be observed by SEEDS and young enough to harbor planets that are still detectable at infrared wavelengths due to their own thermal emission. Stars in moving groups are attractive targets for the SEEDS project because the stars within a moving group have approximately the same age and co-evolve together. Accordingly, the age estimates for all of the stars in a moving group can be refined by measuring the

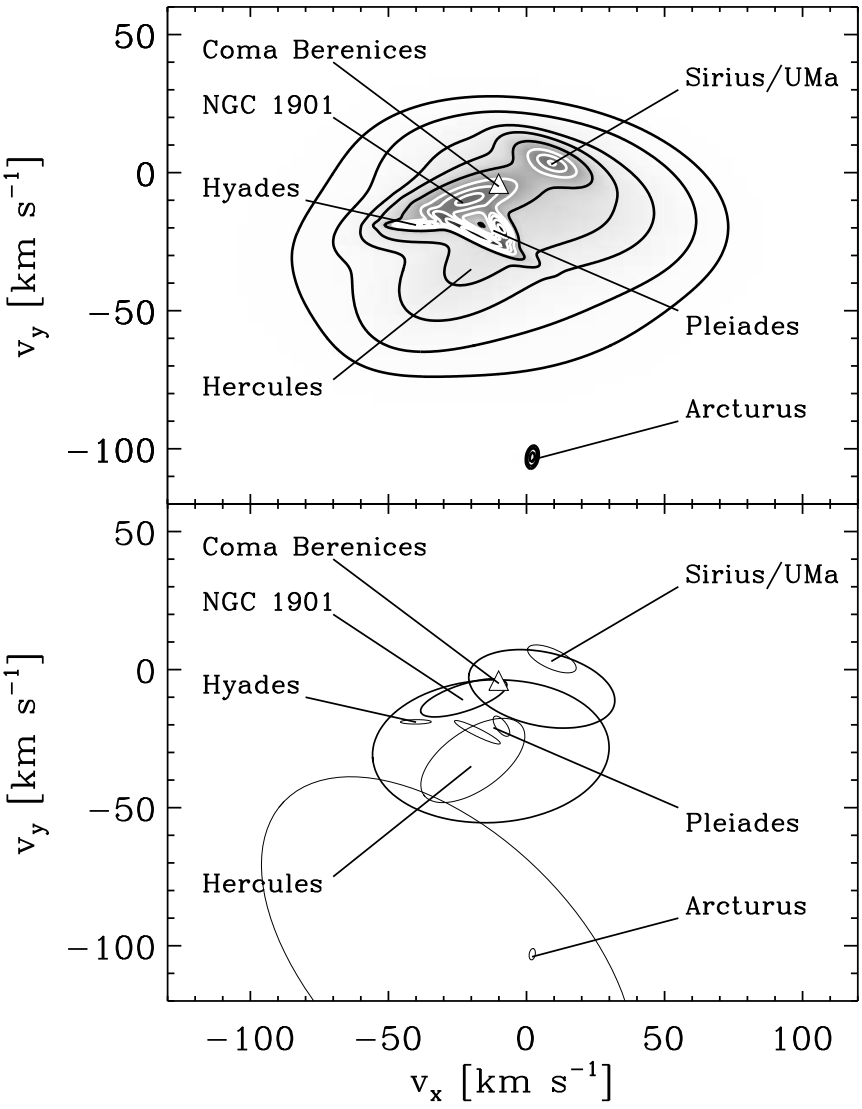

Figure 4.1: Projected velocities of nearby moving groups in the $v_x v_y$-plane from Bovy et al. (2009). The x-velocity is plotted on the x-axis and the y-velocity is plotted along the y-axis. The primary moving groups are labeled. **Top:** Contour plot showing the actual velocity distribution of nearby stars. The shading indicates the number of stars within the contour. **Bottom:** The Gaussians fit to each moving group. The thickness of the line is proportional to the amplitude of the Gaussian and the size of the ellipse indicates the 1σ covariance ellipse. The triangle marks the velocity of the local standard of rest as determined by Hogg et al. (2005).

ages of each member using a variety of age diagnostics such as kinematic dating, X-ray activity, lithium abundance, and cluster dating using HR diagrams. For a review of stellar age determination methods, see Barnes (2007), Cardini & Cassatella (2007), Mayne et al. (2007), Serra & Trager (2007), Koleva et al. (2008), and Hillenbrand (2009).

4.3.3 White Dwarfs

The White Dwarfs team is led by Drs. Gillian Knapp and Cullen Blake at Princeton University. The White Dwarfs team will conduct observations of white dwarfs in order to investigate the frequency and characteristics of planetary systems around white dwarfs. Many of the targets are too faint to be seen without the laser guide star system, so the number of white dwarf targets observed will increase significantly once the laser guide star system becomes operational.

4.3.4 Young Stars

The Young Stars team is led by Dr. Hiro Takami, Dr. Motohide Tamura, and Taro Kudo (Tamura 2009a). The team aims to clarify the connection between disks and planet formation by imaging transition disks around young stars. Transition disks are donut-shaped protoplanetary disks that have been depleted in the inner regions closest to the star, possibly due to the presence of a planet (Absil & Mawet 2009). The Young Stars team will identify stars that are likely to host transition disks using four methods. First, they will examine Spitzer data and other IR data to search for objects with no or little IR excess at 10 μm but with strong excess at longer wavelengths. Second, they will inspect visible data from the Hubble Space Telescope and the CIAO archive to determine whether region around the target star contains any structure. Third, they will look for objects with optical jets that might be indicative of accretion disks. Fourth, they will prioritize observations of targets with emission at wavelengths

longer than 850 μm. Using these critera, the team has identified 25 targets for the first two years of the SEEDS project and plans to observe a total of 65 targets during the five year project. In addition to observing targets that are likely to host transition disks, the Young Stars group also hopes to image planets in binary star systems (YSO Category Team 2008).

4.3.5 Open Clusters

The Open Cluster group falls under the Planet Searches category and is led by Taro Matsuo. The group plans to observe 60 solar-type and early-type stars in the Pleiades open cluster during the five-year SEEDS project. As one of the goals of the SEEDS project is to constrain models of planet formation, observing stars from a single open cluster is advantageous because all of the selected stars will have the same age and metallicity, thus reducing the influence of secondary factors that may influence planet formation. The open cluster team selected the Pleiades open cluster for their observations because the Pleiades are young stars ($\sim$115 Myr: Basri et al. 1996) that are closer to the Earth than other young open clusters. For example, the stars in the Alpha Perseus open cluster are younger (77 Myr: Martín et al. 2001), but they are located 184 pc from the Earth while the Pleiades are only 125 pc from Earth (Matsuo 2009a).

The target selection critera for the open cluster group require that (1) the target star is close enough that planets could be detected between 10 and 500 AU from the target star; (2) the target star is proven to be a member of the Pleiades open cluster; (3) the star is bright enough (R magnitude $<$14) that the adaptive optics system can use the target star as a natural guide star; (4) the target is not in a binary or multiple-star system; and (5) no other objects lie within 2.5" of the target (Matsuo 2009b). The requirement that the target star is a proven member of the Pleides open cluster ensures that the age and composition of the target star is well-defined, and the

final two requirements reduce the chance that a background star or widely separated binary star will be mistaken for a planet.

4.3.6 Debris Disks

The Debris Disk group is led by Category Chief Dr. Tomo Usuda and Semi-Chief Dr. Amaya Moro-Martin (Tamura 2009a). The team aims to directly image stars with debris disks in order to better understand planet formation and the properties of the dust grains that compose debris disks. The team will utilize PDI mode in order to best determine grain size and composition.

The Debris Disk team will select targets that meet all of the required criteria listed below and all of the optional criteria in order to compare the performance of HiCIAO with HST. The team will also select targets that meet only the required criteria in order to detect new disks (Moro-Martin 2008).

1. *Required:* Declination limits due to the latitude of Mauna Kea.
2. *Required:* The star must be bright enough in R band (R<17) to serve as a natural guide star for the AO system until the laser guide star system comes online.
3. *Required:* The dust in the disk must be at least 5×10^{-5} as luminous as the star.
4. *Required:* The dust must lie outside the 0.08" inner working angle of HiCIAO.
5. *Optional:* The star must be faint enough in H band to avoid saturating the detector.
6. *Optional:* The disk must be spatially resolved.

Chapter 5

Instrumentation

5.1 The Subaru Telescope

The Subaru Telescope was commissioned by the National Astronomical Observatory of Japan and has been used for scientific observations since January 1999. Mitsubishi Electric Corporation was the main contractor for the construction, which began in 1991. The monolithic primary mirror has a physical diameter of 8.3 meters and an effective aperture of 8.2 meters. The mirror was manufactured by Corning Glass Works, Inc. and then polished by Contraves Brashear Systems before being aluminized in the basement of the building housing the Subaru Telescope (Kaifu et al. 2000). Until the construction of the twin 8.4 meter mirrors for the Large Binocular Telescope, the 8.2 meter Subaru mirror was the largest monolithic mirror in the world (Hill & Salinari 2004).

5.2 Subaru Adaptive Optics System

Because the goal of the SEEDS project is to detect faint objects at small angular separations from bright stars, SEEDS operations require the use of adaptive optics to reduce atmospheric distortions. HiCIAO's predecessor CIAO was used with the orig-

inal 36-element adaptive optics system on Subaru (Tamura et al. 1998), but HiCIAO was designed for use with the upgraded 188-element AO188 system (Tamura et al. 2006). As reviewed in Section 3.1, adaptive optics is an advanced imaging technique that reduces the effect of atmospheric blurring in astronomical images by monitoring the incoming wave front for distortions and modulating the shape of a deformable mirror to apply a compensating distortion to the incoming light (Beckers 1993). The number of "elements" in an adaptive optics system refers to the number of actuators that change the shape of the deformable mirror, so adaptive optics systems with a higher number of elements tend to remove atmospheric distortions more effectively than systems with a lower number of elements because they can control more spatial frequencies (Beckers 1993). Using the original 36-element adaptive optics system, CIAO achieved a Strehl ratio[1] of 0.1 in H-band (Tamura et al. 2006), and the introduction of the 188-element system allowed HiCIAO to achieve a Strehl ratio of 0.3 in H-band (Suzuki et al. 2009).

5.3 Differential Imaging Science Camera

The workhorse of the SEEDS project is the HiCIAO (High Contrast Imager for Next Generation Subaru AO188 Adaptive Optics) imaging system, which is the next generation of the original CIAO (Coronagraphic Imager with Adaptive Optics) imaging system that was installed on the telescope as one of the first generation AO instruments in 1998 (Takami 2008). Like many instruments on large telescopes, the HiCIAO imaging system is located at the infrared Nasymth focus of Subaru instead of at the prime focus of the telescope. The decision to place the instrument at the Nasymth focus instead of at the prime focus was motivated by the weight and size constraints applied to instruments at the prime and Cassegrain foci as well as the

[1] As explained in Chapter 3, the Strehl ratio is a measure of how well the produced point-spread function reproduces the theoretical capability of a system.

ease of access to instruments at the Nasymth focus, which is located in a room on the second floor of the telescope building and is easily accessible to workers. Figure 5.1 displays the design of the telescope and indicates the position of HiCIAO at the Nasymth focus. The positions of several other commonly used instruments such as the Fiber Multi-Object Spectrograph (FMOS) and the Multi-Object InfraRed Camera and Spectrograph (MOIRCS) are also indicated in the schematic.

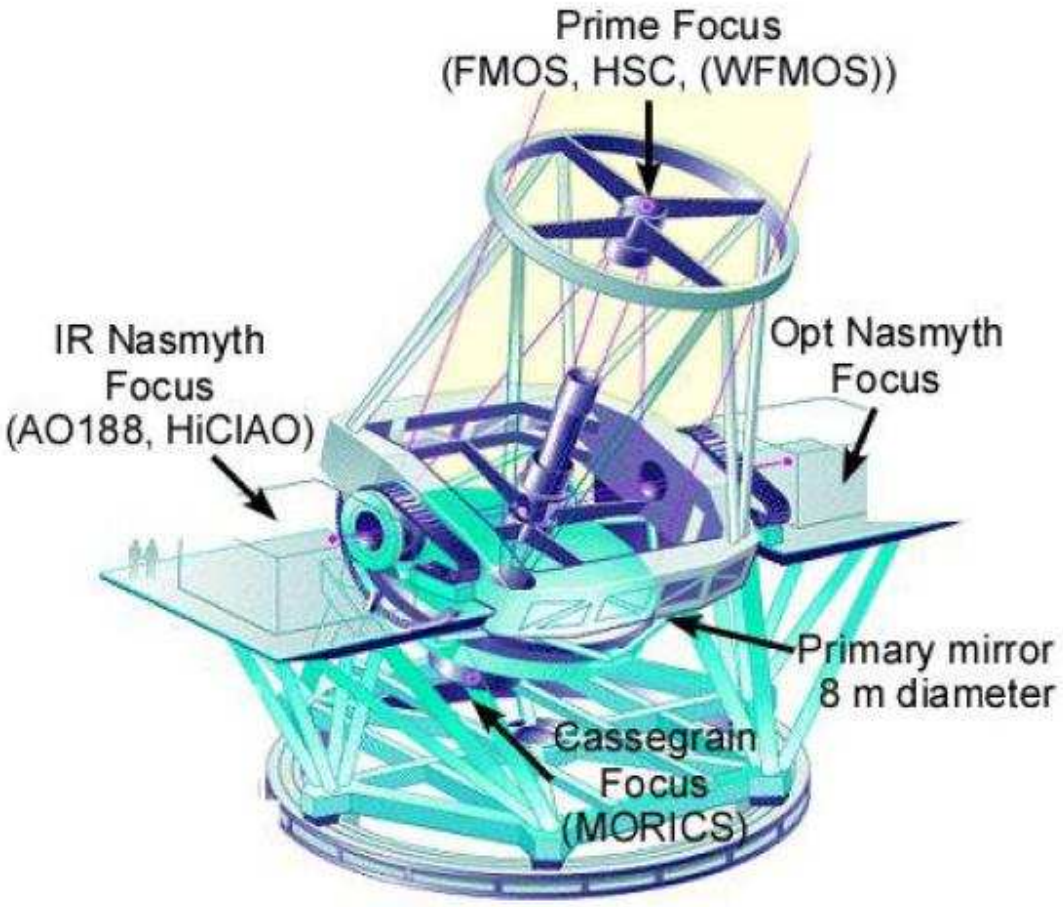

Figure 5.1: Schematic of the Subaru Telescope from Takami (2008). HiCIAO (High Contrast Imager for Next Generation Subaru AO188 Adaptive Optics) and the AO188 adaptive optics are located at the infrared Nasmyth platform to the left of the telescope. The Multi-Object InfraRed Camera and Spectrograph (MOIRCS) is located at the Cassegrain focus at the base of the telescope, and the Fiber Multi-Object Spectrograph (FMOS) is located at the prime focus. The Hyper Suprime-Cam (HSC) and the Wide Field Multi-Object Spectrograph (WFMOS) will also be installed at the prime focus and should see first light in 2012 and 2015, respectively. Note the two figures at the back corner of the infrared Nasmyth platform for scale.

HiCIAO was designed by Klaus Hodapp and built by a team of engineers and scientists from NAOJ, the University of Hawaii, Subaru Telescope, Okayama Astrophysical Observatory, Université de Nice-Sophia Antipolis, the Space Research Institute, and the Graduate University for Advanced Studies. The finished instrument measures 2.06 meters wide, 1.53 meters long, and 1.8 meters high including the support frame and consists of three modules: a cryogenically cooled camera module, a room-temperature coronograph module, and an instrument support frame module (HiCIAO Team 2009).

As shown in Figure 5.1, the camera module contains the camera optics, three separate filter wheels, and the Teledyne HAWAII-2RG 2048×2048 pixel detector (Tamura et al. 2006; Suzuki et al. 2009). The first filter wheel is the common path filter wheel and is used for broadband filters when the instrument is operated in direct imaging or polarimetric differential imaging modes. This filter wheel is currently fitted with Y, J, H, and K broadband filters and could hold up to eleven filters (Hodapp et al. 2008). The next filter wheel is the pupil wheel and contains an achromatic double lens system used to re-image the pupil plane onto the focal plane to perfect the alignment of the Lyot stop with the telescope. The third filter wheel is the differential path filter wheel. As the name suggests, this filter wheel is used to insert different narrowband filters into the path of each of the four beams of light when the instrument is operated in differential imaging mode. The differential path filter wheel currently contains one set of filters sensitive to methane absorption and one set of filters sensitive to H_2 emission. The differences between direct imaging, polarimetric differential imaging, and spectral differential imaging modes as well as the justification for searching for methane absorption and H_2 emission will be explained in Section 5.4.

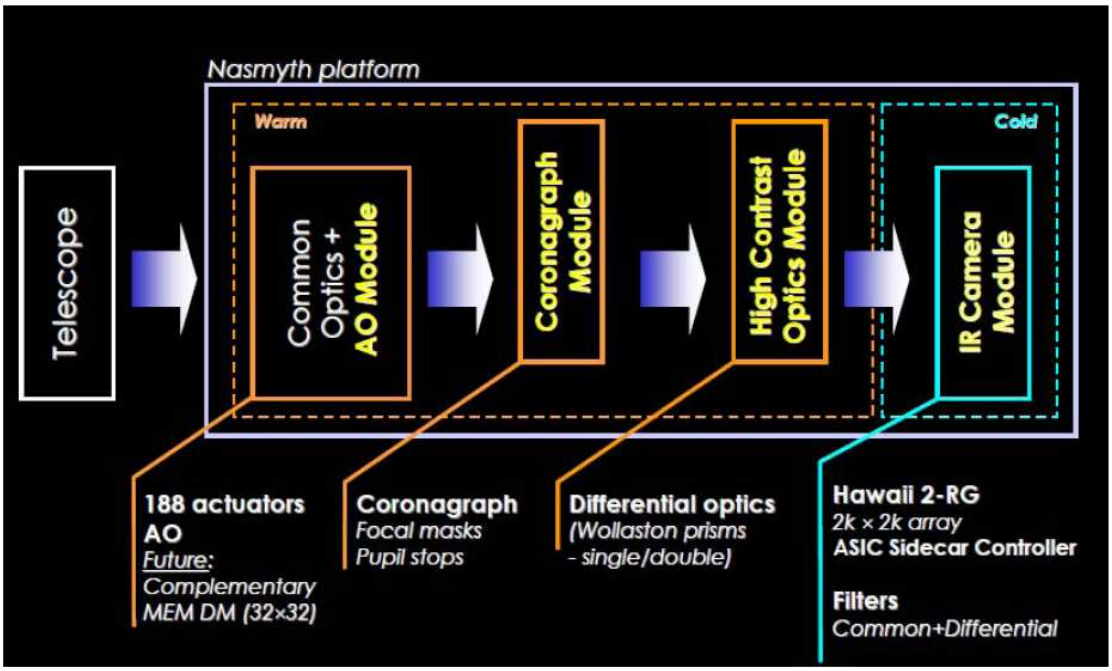

Figure 1.1: *(top)* Whole picture of the HiCIAO instrument. A black box and a blue box on the top are the warm coronagraph module and the cryogenic camera module, respectively. *(bottom)* Schematic diagram of the HiCIAO system.

Figure 5.2: Schematic of the HiCIAO imaging system from (HiCIAO Team 2009). Light entering the system from the telescope first encounters the common optics and AO module. Some of the light is diverted to the adaptive optics system while the remainder of the light continues onward to the cornograph module. The light then passes through the high contrast optics module, where the beam is split by a single Wollaston prism for PDI operations or double Wollaston prism for SDI operations. When HiCIAO is operated in DI or ADI mode, the beam passes straight through the high contrast optics module without being split. After exiting the high contrast optics module, the beam enters the IR camera module, which is the only part of the HiCIAO imaging system that is kept cold. The IR camera module contains the Hawaii 2-RG infrared detector as well as three filter wheels described in Section 5.3.

5.4 Observing Modes

In order to maximize the versatility of HiCIAO and increase its sensitivity to exoplanets, HiCIAO can be operated in several different observing modes. As introduced in Section 3.2, there are three techniques commonly used to remove the quasi-static speckles that are the primary source of noise in high contrast images once most of the atmospheric distortion has been reduced by adaptive optics. The theory behind polarization differential imaging (PDI), spectral differential imaging (SDI), and angular differential imaging (ADI) was explained in Section 3.2; this section focuses on how the HiCIAO camera specifically operates in each observing mode. Subsection 5.4.1 discusses the default Direct Imaging mode and Subsections 5.4.2, 5.4.3, and 5.4.4 cover PDI, SDI, and ADI observations, respectively. Since only PDI and SDI modes require special filters, HiCIAO can be operated in any combination of observing modes except for PDI+SDI mode.

5.4.1 Direct Imaging

The Direct Imaging (DI) mode is the simplest observing mode for HiCIAO and results in the largest possible field of view (20" × 20"). In DI mode, the light from the target is sent to the detector without passing through any filters or polarization spliters. Since all of the light from the source reaches the detector, DI mode can be used on fainter sources than PDI or SDI or with shorter integration times on sources of the same brightness. The disadvantage of DI mode is that it does not take advantage of spectral or polarization differences to distinguish the light from planets or disks from starlight. Accordingly, DI mode is usually used in combination with PDI mode or SDI mode as explained in Subsections 5.4.2 and 5.4.3, respectively.

5.4.2 Polarization Differential Imaging

The Polarization Differential Imaging (PDI) mode on HiCIAO is designed to exploit the fact that light scattered by disks is usually polarized while starlight is typically unpolarized. In PDI mode, light from the target is split by a single Wollaston prism and forms two separate 10"×20" images on the detector. Although operating HiCIAO in PDI mode sacrifices some of the field of view available in DI or ADI mode, PDI mode is particularly useful for highlighting polarized sources in close proximity to the star. A fraction of light is lost when the beam passes through the Wollaston prism, so integration times for PDI mode tend to be slightly longer than integration times for DI mode.

PDI mode can be used in conjunction with either ADI mode or DI mode. PDI+ADI mode is best for identifying edge on disks and planets within the same field of view, but PDI+DI is far superior to PDI+ADI for observing face-on disks because the azimuthal symmetry of the disk can cause face-on disks to be subtracted out of the final image in PDI+ADI mode. The PDI+ADI data reduction pipeline is still being improved, however, and PDI+ADI imaging might become appear advantageous once the full potential of PDI+ADI data is realized.

5.4.3 Spectral Differential Imaging

Like stars, brown dwarfs and giant planets have several characteristic absorption lines. Spectral Differential Imaging (SDI) mode takes advantage of the spectral differences between substellar objects and main sequence stars to separate light from the target star from light from brown dwarfs or planets. Any spectral filters could be inserted in the differential path filter wheel in the HiCIAO science camera, but the system is currently set up to work with methane filters because methane absorption is one of the key differences between stellar and substellar spectra.

The methane filters used by SEEDS have central wavelengths of 1575 nm, 1600 nm,

1625 nm, and 1644 nm, and and bandwidths of 25 nm. The narrow bandwidth of the filters has posed a problem for the SEEDS project because so few photons reach the detector that integration times must be substantially increased. The SEEDS team has ordered broader-band replacement filters that should separate planet light from star light without reducing the throughput as dramatically as the original SDI filters. The new filters should allow a much larger fraction of the light to reach the detector so that fainter planets and disks can be detected in SDI mode.

5.4.4 Angular Differential Imaging

Operating HiCIAO in Angular Differential Imaging (ADI) mode alters the speed of the image rotator so that the PSF remains fixed while the field of view and any possible companions rotate across the detector. Since ADI mode does not require any special filters, ADI mode can be used in conjunction with DI, PDI, or SDI mode. ADI+PDI mode should allow the SEEDS team to detect planets and disks in the same system. ADI+SDI mode will be useful for revealing planets with methane absorption features once the new, wider SDI filters have been installed.

Chapter 6

Data Reduction

As explained in Chapter 5, the HiCIAO camera acquires data in DI, PDI, SDI, and ADI modes. Although the basic calibration is the same for images acquired in any of these modes, the specifics of the reduction sequence vary based on how the image was acquired. In Sections 6.1 and 6.2 we present a brief overview of the DI+ADI and PDI+ADI data reduction pipelines, respectively, followed by a thorough discussion of each of the subroutines involved in the reduction process in Sections 6.3.

6.1 DI+ADI Pipeline Overview

In DI+ADI mode, a set of broadband images is acquired while the image rotator is adjusted so that the stellar PSF remains stationary on the detector as the background stars and any companions rotate across the field of view. Each frame in the observation sequence is therefore rotated from the other frames and must be derotated before producing a composite image. Since the observation is acquired in DI mode, the full 20" × 20" field of view is preserved and the maximum amount of flux reaches the detector because only broadband filters are used. These broadband filters allow approximately 20% of the light to pass through the spectral bandpass and are available in Y, J, H, and K.

Prior to image derotation, each frame is destriped to correct for systematic offsets in detector response. The destriped images are saved with the extension "_ds.fits" and then flat-fielded, dark-subtracted, and corrected for hot pixels. Since the gravitational torque on the detector can alter the position of objects on the detector, the dewarping routine designed by Sebastian Egner (Egner 2009) is applied to correct for possible distortion in the field. Next, a reference image is shifted so that the target star is at the center of the frame and all other all of the other frames in the sequence are aligned to the reference image. The centered and corrected images are saved under the same filenames as before but with a "_r.fits" extension.

A radial profile is then constructed from the "_r.fits" frames and subtracted from each frame. The resulting files are saved with the extension "_f.fits" and then derotated and combined in annuli to produce the reduced "final.fits" image. Next, fake companions are inserted into the dataset and the reduction process is completed. Finally, a contrast curve is computed for the dataset based on the brightness of the artifically inserted companions at the end of the reduction process.

6.2 PDI+ADI Pipeline Overview

The PDI+ADI data reduction pipeline is slightly more complicated than the DI+ADI pipeline because frames are acquired in two polarizations. In order to maximize the sensitivity of HiCIAO and fully utilize the power of ADI to reduce the noise due to quasi-static speckles, the frames from the two polarizations are reduced separately and then combined after the usual DI+ADI reduction procedure has been completed for each polarization.

6.3 Explanation of Pipeline Subroutines

This section provides a brief overview of the primary IDL routines used in the SEEDS data reduction pipeline for ADI+DI and ADI+PDI data. More detailed information for each routine can be found in Appendix A.

6.3.1 see_fits.pro

This routine was written by Courtney Dressing and allows the user to visually examine frames before begining the reduction process. The program works with all types of observations, including photometry frames, and can be used with either destriped or non-destriped frames. *See_fits.pro* displays each frame sequentially in an IDL window and produces the text output files "good_frames.txt" and "bad_frames.txt" containing the filenames of the user-identified good and bad frames.

6.3.2 setupdir.pro

This simple routine sets the stage for the rest of the data reduction by establishing the data, reduction, and calibration directories and setting the name of the log file. *Setupdir.pro* is called by many of the other pipeline subroutines so that the user does not have to constantly input the locations of the data and calibration files and the desired locations for the reduced frames. Currently, *setupdir.pro* must be edited by hand for each reduction, but it would be trivial to write a short program to change the directories and filenames automatically based on user-provided keywords.

When *setupdir.pro* is called by other routines, it returns the values of the indicated keywords. The keywords currently in use are explained below. For all directories, the user must remember to include the final slash ('/') or problems may result in errors farther down in the pipeline.

6.3.3 mkobslog.pro

This short routine calls *setupdir.pro* to determine the data directory and the desired logfile name and then produces a log containing a list of all of the FITS files in the data directory. The logfile is written to the working directory, so the user should call *mkobslog.pro* from the reduction directory.

6.3.4 newobs.pro

This routine is the first stage in the reduction process at which the user must specify the target to reduce. *Newobs.pro* is called with only an optional keyword to specify the target database, but the user is required to input the date, object, filter, and suffix for the .info file after a series of prompts. Since the date, object name, and filter must match exactly, the user is encouraged to inspect the logfile produced by *mkobslog.pro* to verify the date and filter of the desired observation. As indicated by the prompt, the date should be entered in YYYY-MM-DD format. The optional "targetdatabase" keyword is only necessary if the target object cannot be found in the SIMBAD database. See Appendix B for instructions about how to create a target database.

The end result of calling *newobs.pro* is that a set of text files is produced containing lists of the saturated and unsaturated observations. For PDI reductions, *newobs.pro* also produces lists of the frames corresponding to each polarization. A brief overview of the names and contents of each text file is below. In all cases, the filename begins with "[name of object]+[optional suffix]" and the file is written in the main reduction directory set by "reducdir" in *setupdir.pro*.

6.3.5 destripe_alt3.pro

This routine cleans an image by removing horizontal and vertical stripes induced by instrumental defects. *Destripe_alt3.pro* is called with the target name (e.g., "GJ758") as well as the optional keywords "horizontal_only" and "fourier." The keywords are explained in Appendix A.2.

6.3.6 destripe_directory.pro

As an alternative to running *destripe_alt3.pro* for each target, the user could also run the modified version *destripe_directory.pro* created by Michael McElwain to destripe an entire directory at once. Since destriping does not depend on registration and image correction, images can be destriped before or after running *setupdir.pro*, *mkobslog.pro*, or *newobs.pro*, but destriping must be completed before running *reduc_sat_alt.pro*.

6.3.7 reduc_sat_alt.pro

This procedure was written by David Lafreniere for the Gemini data reduction pipeline and later modified by Markus Janson and Michael McElwain for use with Subaru data. The routine is called with the name of the info file corresponding to the the target (e.g., "GJ758.info") as well as numerous optional keywords. The purpose of *reduc_sat_alt.pro* is to correct and register the frames. The routine flat-fields, dark-subtracts, removes bad pixels, and applies a distortion correction to each frame before aligning the stellar point-spread function (PSF) in each frame with the stellar PSF in a reference frame. The optional keywords for *reduc_sat_alt.pro* are described in Appendix A.11.

6.3.8 filtseq.pro

This routine was written by David Lafreniére and subsequently edited by Markus Janson. *Filtseq.pro* reads in a group of files from the reduction directory and creates a radial profile using either *tt_radialize.pro* or *profrad.pro* based on the user's preference. The program then subtracts the radial profile from each frame and saves the resulting frames under new filenames. The only required input parameter for *filtseq.pro* is the name of the target to reduce ("pfname"), but the user may provide several optional input parameters and keywords as well.

6.3.9 subadi.pro

This step of the pipeline was written by David Lafreniére and modified by Markus Janson and Christian Thalmann. The routine is the core of the ADI pipeline and implements the Locally Optimized Combination of Images (LOCI) algorithm to remove speckles from each frame. The frames are then derotated and combined to produce a fully reduced image. The image is written to the file "final.fits" and is later used by *calc_contrast.pro* or *star_contrast.pro* to produce a contrast curve for the observation.

6.3.10 partial_sub.pro

Like *filtseq.pro*, this routine was written by David Lafreniére and later edited by Markus Janson. The program introduces fake companions into the dataset and then compares the amount of flux recovered by the ADI reduction to the original flux of the fake companions. The radii of the fake companions and the fraction of recovered flux at each radius are written to the file "partial_sub[IorP].dat" and then used by *calc_contrast.pro* or *star_contrast.pro* to produce a contrast curve.

6.3.11 calc_contrast.pro

This routine was written by David Lafreniére and commented by Miwa Goto. Once the "partial_sub.dat" file containing the amount of flux from a fake companion recovered at each has been created by *partial_sub.pro*, *calc_contrast.pro* can be used to produce a contrast curve that indicates the sensitivity of the data to extrasolar planets at each radius. In addition to the data from "partial_sub.dat," *calc_contrast* also relies on the "final.fits" reduced image produced by *subadi.pro* and requires an unsaturated image to determine the PSF of the target star. Accordingly, *calc_contrast.pro* cannot be used to produce contrast curves for datasets which lack unsaturated images of the target star. An alternative method of calculating the contrast curve is to run *star_contrast.pro* and use the PSF of an unsaturated background star instead of the target star.

6.3.12 star_contrast.pro

This routine was written by Christian Thalmann and Michael McElwain. Like *calc_contrast.pro*, *star_contrast.pro* uses the output of *partial_sub.pro* to determine the contrast of an observation. However, rather than use an unsaturated frame to determine the PSF, *star_contrast.pro* determines the PSF shape from the PSF of unsaturated background star in the frame. The user must explictly specify the coordinates of the background star by editing *star_contrast.pro* before calling the procedure.

Chapter 7

The Importance of Field Rotation

This chapter is devoted to exploring the effect of field rotation on sensitivity. Section 7.1 introduces the motivation for the study, Section 7.2 describes the datasets chosen for the study, and Section 7.3 provides an overview of the methodology. Finally, Section 7.4 presents the results of the study and discusses the implications of the findings for future SEEDS observations.

7.1 Exploring Rotation Rate: Motivation

As explained in Section 3.2.1, ADI cannot be used without field rotation. Changing the rotation rate of the image rotation allows the field of view to drift across the detector so that potential planets and disks are preserved during image subtraction instead of being removed along with the quasi-static noise speckles targeted by ADI. A natural conclusion from this explanation might be that field rotation correlates directly with image quality so that increasing field rotation will improve sensitivity because a higher fraction of the frames will have rotated enough to be included in the locally optimized combination of images (LOCI).

High contrast imaging is complex, however, and a variety of other factors complicate the relationship between field rotation and image quality. During a typical

night, an observer will not usually have the freedom to observe each target during the period of maximum field rotation or for the time required to capture the entire peak of the rotation curve. Rather, an observing team will face pressure to observe some targets at less-than-optimal rotation rates or for short time periods so that a larger number of targets can be observed during the observing run. Observers will be forced to strategically plan their observations in order to maximize the scientific returns from a restricted amount of telescope time. Although observers have a limited ability to foresee observing conditions or malfunctions during the observing run, observers can be prepared with a variety of observing plans designed to maximize the scientific yield under a range of observing conditions.

The first step in developing an observing plan is to determine a list of targets, but this chapter assumes that a target list has already been prepared. Once the targets have been selected, observers can easily use the coordinates of a target and the location of the observatory to produce plots of the predicted rotation rates of the object during the timeframe of the observing run. Dr. Miwa Goto of the Max Planck Institute for Astronomy has developed a particularly nice IDL widget to plot the rotation curves, so the user merely needs to supply the coordinates for each target and the date of observation. A screenshot of the IDL widget is shown in Figure 7.1.

The next step is significantly more challenging. Based on the resulting rotation curves and the scientific motivations behind each target, observers must devise an observing plan to best explore the selected targets. In most cases, this will involve making difficult choices about when to observe each target and how long to study each target. Due to the subjective nature of judging the scientific merit of each target, determining the observing schedule will likely be a detailed process for the duration of the SEEDS survey. However, quantitative data characterizing how image quality changes with increasing amounts of field rotation will help observers to determine the ideal observing plan. In this chapter, we investigate the connection between image

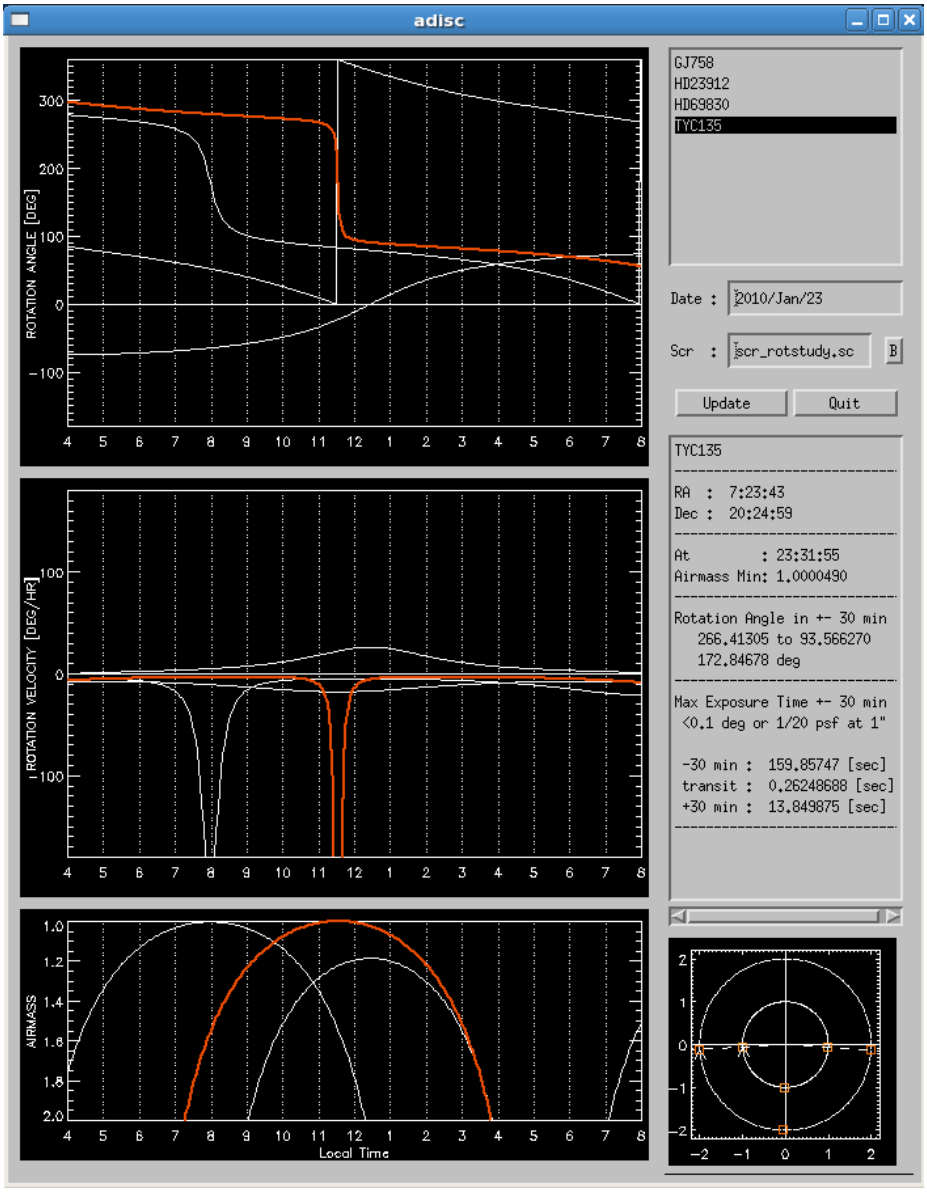

Figure 7.1: Screenshot of the field rotation IDL widget produced by Dr. Goto. The top panel of the widget plots the rotation angle in degrees versus the local time for each of the targets listed in the upper right corner. In this screenshot, the targets listed (GJ 758, HD 23912, HD 69830, and TYC 135) are the targets that were chosen for the rotation study. The highlighted red curve displays the rotation rate for TYC 135. From top to bottom at 5 PM local time, the three white curves indicate the rotation rates for HD 23912, GJ 758, and HD 69830. For this example, the date is set to January 23, 2010 even though GJ 758 was observed in August. The middle plot displays the rotation velocity in degrees per hour for each target and the bottom plot shows the airmass of each target as a function of time. Key information about the highlighted target is shown in the box in the middle of the right panel, and the small plot in the lower right indicates the range of telescope pointings required to track the object for the entire night.

quality and field rotation by comparing the resultant sensitivity produced by reducing various subsets of existing datasets covering a range of rotation angles.

7.2 Selected Datasets

The datasets chosen for the rotation analysis are the ADI observations of GJ 758, HD 23912, HD 69830, and TYC 1355-214-1. The rest of this section is devoted to a brief introduction of each dataset, and the main characteristics of each dataset are provided in Table 7.1. GJ 758 (also NLTT 47754, HIP 95319, and HR 7368) is a G9V star located 15.5 pc from Earth (Perryman & ESA 1997; Gray et al. 2003) and was imaged as one of the commissioning targets. The selection of GJ 758 as a commissioning target was promoted by Dr. Joseph Carson, who had previously observed GJ 758 using the Palomar 200" and suspected that the star might have a companion at a large separation. GJ 758 was also a favorable choice for the commissioning run because there are several background stars in the field of view, and those stars could be used as a test of the astrometric performance of HiCIAO.

GJ 758 has a V-band magnitude of 6.361 and an H-band magnitude of 4.743 (Cutri et al. 2003). The GJ 758 dataset consists of 47 science frames acquired during the August 2010 commissioning run. All of the frames were visually inspected, and 45 science frames were selected for the analysis. Although the GJ 758 data were acquired during the commissioning phase of the project, the data are high-quality and revealed the presence of the 10-40 $M_{\rm J}$ companion GJ 758 b discussed in Section **??** (Thalmann et al. 2009). Various age indicators place the age of GJ 758 between 0.7 and 8.7 Gyr (Duncan et al. 1991; Wright et al. 2004; Barnes 2007; Takeda et al. 2007; Mamajek & Hillenbrand 2008; Thalmann et al. 2009).

HD 23912 (also 2MASS J03493272+2322494) is an F3 star that was observed during the January SEEDS observing run. There is no measured parallax for HD 23912,

Table 7.1: Datasets Chosen for Rotation Analysis

		GJ 758	HD 23912	HD 69830	TYC 1355-214-1
Target Star Properties	Alternative Names	NLTT 47754 HIP 95319 HR 7368	2MASS J03493272 +2322494	LHS 245 HIP 40693 HR 3259	2MASS J07234358+2024588 BD+20 1790
	RA (ICRS, J2000)	19 23 34.0	03 49 32.7	08 18 23.9	07 23 43.6
	Dec (ICRS, J2000)	+33 13 19.1	+23 22 49.5	-12 37 55.8	+20 24 58.7
	Spectral Type	G8	F3	K0	K5
	H-Band Magnitude	4.743	8.097	4.364	7.032
	Distance (pc)	15.5	unknown	12.5	unknown
	Age (Myr)	0.7–8.7	115	2000	50
Dataset Properties	Date Observed	Aug 6, 2009	Jan 24, 2010	Jan 23, 2010	Jan 23, 2010
	Science Frames	10740-10770, 10772-10774[a] 10781-10791 (45 frames)	27624-27798[b] (175 frames)	26274-26379 (99 frames)	26129-26244 (101 frames)
	Science Integration (sec)	19.50	9.75	5.57	13.93
	Photometry Frames	10734-10735 (1.39 sec) 10738 (13.926 sec) (all saturated)	27617-27620 (1.39) 27621-27623 (9.75 sec) 27834-27838 (1.39 sec)	2658 (1.39 sec) 26259-62 (4.18 sec) 2663 (2.79 sec)	26119 (1.39 sec) 26121 (9.75 sec) 26122-26124 (1.39 sec) 26245-26247 (1.39 sec)
	Photometry Filter	none	ND10	ND1	ND10
	Total Integration Time (min)	14.63	28.4	9.2	23.4
	Total Field Rotation (deg)	31.0	72.8	26.0	168.1

[a] All filenames for GJ 758 data should be prefaced with "HICA900"

[b] All filenames for HD 23912, HD 69830, and TYC 1355-214-1 data should be prefaced with "HICA000"

but there is a 96% probability that the star is a member of the Pleiades cluster (Schilbach et al. 1995). Since HD 23912 is part of a relatively young cluster (age ∼115 Myr: Basri et al. 1996), any gas giants orbiting HD 23912 are likely to still be warm enough to be detected via direct imaging if they lie far enough away from the star. HD 23912 exhibits a measured proper motion of 20.90 mas/yr in right ascension and -42.70 mas/yr in declination (Høg et al. 1998), so potential companions could be distinguished from background objects by exhibiting common proper motion. The HD 23912 dataset consists of 175 science frames and twelve photometry frames aquired with the 10% neutral density filter (ND10). All of the science frames have exposures of 9.75 seconds, and the photometric frames have exposure times of either 9.75 or 1.39 seconds. Both the science and photometric frames were taken in H-band without a coronagraph.

HD 69830 (also LHS 245, HIP 40693, and HR 3259) is another of the nearby stars targets. HD 69830 is a K0V star located 12.5 pc from Earth (Perryman & ESA 1997; Cenarro et al. 2007) with an H-band apparent magnitude of 4.36 (Cutri et al. 2003). X-ray activity measurements yield an accepted age of approximately 2000 Myr years (Song et al. 2000), but other age measurements based on infrared emission from dust (Bryden et al. 2006) and Ca II H and K activity measurements (Wright et al. 2004) result in a range of age measurements between 600 Myr and 4.7 Gyr. The HD 69830 dataset was acquired on January 23, 2010 and includes 111 science frames and six photometry frames taken with the 1% neutral density filter (ND1). After removing frames with bad or extended PSFs, 99 frames remained for the rotation analysis. The science frames were integrated for 5.57 seconds, and the photometric frames have exposure times of 1.39, 2.79, and 4.18 seconds. All of the frames were taken in H band without a cornographic mask.

TYC 1355-214-1 (also 2MASS J07234358+2024588) is a variable star, a member of the AB Dor Moving Group (Zuckerman & Song 2004; López-Santiago et al. 2006), and

a possible host star of a controversial planet detected via radial velocity measurements (supporting data: Hernán-Obispo et al. 2009; Hernán-Obispo et al. 2010, challenging data: Figueira et al. 2010a; Heinze et al. 2010a,b). TYC 1355-214-1 is a K5 star with an apparent V-band magnitude of 9.93 and an apparent H-band magnitude of 7.032 (Cutri et al. 2003; Reid et al. 2004). There is no measured parallax for TYC 1355-214-1, but the star has a large proper motion of -65.8 mas/yr in RA and -228.1 mas/yr in Dec (Høg et al. 2000). The TYC 1355-214-1 dataset was acquired on January 23, 2010 and consists of 109 science frames and six photometry frames taken with the 10% neutral density filter (ND10). Visual inspection of the science frames revealed that eight frames had poor AO performance, so only 101 frames were suitable for the rotation study. All 101 science frames have exposure times of 13.93 seconds, and the photometry frames have shorter exposure times of 1.39 seconds and 9.75 seconds. Both the science frames and the photometry frames were taken in H band without a coronagraph.

7.3 Exploring Rotation Rate: Methodology

The first stage in the rotation analysis was to select several existing datasets on which to conduct the analysis. While using all of the SEEDS survey data may have increased the reliability of the rotation analysis, the time and processing advantages of using a subset of the data outweighted the potential increase in generalizability provided by reducing all of the survey data. In order to improve the applicability of the study without reducing all of the existing SEEDS observations, the rotation analysis was repeated using the three different datsets introduced in Section 7.2: GJ 758, HD 69830, and TYC 1355-214-1. All three datasets have high PSF stability and cover a wide range of rotation angles.

Once the datasets were chosen, all of the science and photometry frames of each

target were carefully inspected to remove frames with bad or off-center PSFs and frames in which the pupil viewer was still visible. The frames were examined visually using the program *see_fits.pro* and the FITS headers for each frame were checked using the observation log produced by *mkobslog.pro*. The main features of *see_fits.pro* and *mkobslog.pro* are explained in Sections 6.3.1 and 6.3.3, respectively, and a manual for both routines is provided in Appendix A.

After the bad frames were removed, each of the three targets was reduced according to the standard DI+ADI reduction procedure described in Section 6.1 using the full set of science frames. Since these reductions include the maximum possible field rotation for each target and the maximum number of frames, the full reduction of each dataset provides a baseline for subsequent comparison. Theoretically, reducing all of the frames for each target should produce the best possible contrast curve for an observation. If reducing a subset of images results in a higher quality final image than reducing the entire dataset, then changes in seeing, airmass, and other instrumental effects must outweigh the theoretical improvements provided by increased field rotation.

To test the hypothesis that decreasing the amount of field rotation would decrease the sensitivity of the final image, each dataset was subdivided into several smaller datasets of consecutive frames using the routine *make_redgrps.pro* written by Courtney Dressing. This routine is documented in Appendix A.5. For the HD 69830 dataset, for example, the smaller datasets contained either 50 frames or 90 frames. Since there are multiple ways to extract a smaller number of consecutive frames from the 99 total HD 69830 frames, there are ten different 90-frame reductions and 50 different 50-frame reductions for the HD 69830 dataset. To avoid confusion with terminology, the full set of frames for a target will be referred to as a "dataset" and the groups of sub-datasets containing n frames will be called "classes." Within a class, each set of n frames is a "subgroup." Accordingly, the HD 69830 dataset contains a

Table 7.2: Classes for Rotation Analysis

Target	Total Number of Frames	Number of Frames per Subgroup
GJ 758	45	25, 30, 35, or 40
HD 23912	175	50 or 100
HD 69830	99	50 or 90
TYC 1355-214-1	101	50 or 100

50-frame class with 50 subgroups and a 90-frame class with ten subgroups.

Physically, altering the number of frames within each reduction subgroup changes the total integration time for the target, and shifting the starting frame of the reduction subgroup affects the total field rotation of the target because the rotation rate is time-dependent. As shown in Table 7.2, at least two different sizes of subgroups were selected for each target. The HD 23912, HD 69830 and TYC 1355-214-1 datasets contain over twice as many frames as the GJ 758 dataset, so the subgroups used for those datasets are correspondingly larger than the subgroups used for the GJ 758 dataset. Furthermore, since the GJ 758 dataset is much smaller than the other three datasets, additional subgroups were created from the GJ 758 dataset to explore the relative influence of total integration time and rotation rate on sensitivity. Due to the large size of the HD 23912 dataset (175 frames) and the time that would have been required to reduce each set of consecutive frames, the 50-frame and 100-frame reduction subgroups for the HD 23912 dataset consist of every fifth set and every tenth set of consecutive frames, respectively. The decision to set the "spacing" keyword when calling *make_redgrps.pro* to create these datasets allowed the author to probe a wide range of rotation rates without devoting hundreds of hours to reducing the dataset.

The total integration time and range of field rotations for each class are displayed in Table 7.3. Since field rotation is greatest during transit (see Figure 7.1), the subgroups in each class with the maximum field rotation contain frames acquired closer to transit than the subgroups with lesser amounts of field rotation. As shown in Table 7.3, the smaller classes cover the widest range of rotation angles and are therefore

Table 7.3: Integration Time and Field Rotation for Rotation Classes

Target	Class	Total Integration Time (min:sec)	Minimum Field Rotation (deg)	Maximum Field Rotation (deg)
GJ 758	25	8:07	10.08	22.84
GJ 758	30	9:45	12.30	24.91
GJ 758	35	11:22	26.31	26.88
GJ 758	40	13:00	28.76	29.05
HD 23912	50	8:07	5.93	43.22
HD 23912	100	16:15	18.33	61.14
HD 69830	50	4:38	12.12	13.69
HD 69830	90	8:21	22.74	23.41
TYC 1355-214-1	50	11:36	12.28	156.36
TYC 1355-214-1	100	23:13	166.89	167.36

the most useful classes for determining the effect of field rotation on sensitivity. The subgroups in the larger classes have almost the same field rotation and should thus have nearly identical contrast curves if field rotation is the dominant factor affecting sensitivity. If the contrast curves differ significantly within the 90-frame GJ 758 class and the 100-frame TYC 1355-214-1 class, then that would indicate that atmospheric conditions and instrumental effects play an important role in limiting the achievable contrast and that field rotation alone is not a reliable predictor of sensitivity.

Once all of the required subgroups were created by *make_redgrps.pro*, each subgroup was reduced following the usual ADI+DI reduction procedure covered in Section 6.1. Although the standard pipeline uses *photo_contrast.pro* to determine the contrast, that routine could not be used with the GJ 758 dataset because *photo_contrast.pro* requires an unsaturated frame for photometry, and all of the GJ 758 frames are saturated. As an alternative, the contrast curves for the GJ 758 reductions were produced using the program *star_contrast.pro* developed by Drs. Michael McElwain and Christian Thalmann. This routine determines the effective Strehl ratio using the PSF of a background star rather than an unsaturated image of the target star. A brief summary of *star_contrast.pro* is provided in Section 6.3.12 and the routine is documented in Appendix A.14.

After the contrast curves for each subgroup were computed using *photo_contrast.pro* or *star_contrast.pro*, the routines *photo_con_curves.pro* and *comp_contrast_rotation.pro* were used to produce plots of sensitivity as a function of field rotation and angular separation. As expected, increasing field rotation enhanced the sensitivity of the observation, and field rotation had the strongest effect on the achieved contrast ratio at narrow separations. The intricacies of the relationship between sensitivity and field rotation are discussed in Section 7.4.

7.4 Results and Discussion

As explained in Section 7.2, observations of four targets were selected for inclusion in the rotation analysis. Two of the targets displayed relatively low field rotation (GJ 758: 31°, HD 69830: 26°), while the other two targets exhibited considerable field rotation (HD 23912: 73°, TYC 1355-214-1: 168°). For clarity, we will devote a separate subsection to the results for each target. Since the TYC 1355-214-1 dataset has the largest total field rotation, we will begin the discussion of the effect of field rotation on sensitivity by examinining the reductions of that dataset.

7.4.1 Reduction of TYC 1355-214-1

The contrast curves for each of the 50-frame reductions of TYC 1355-214-1 are displayed in Figure 7.2. The most noticeable feature of Figure 7.2 is that the achieved contrast ratio improves[1] as the separation from the star increases. Since the flux from the star decreases at wider separations, the result that fainter companions can be seen at greater separations is unsurprising. More interestingly, Figure 7.2 also reveals that the amount of field rotation during an ADI observation influences the sensitivity of

[1]The contrast ratio is the ratio of the brightness of the faintest companion that could be detected to the brightness of the star. Accordingly, "higher" contrast ratios refer to smaller numbers because the planet flux is a lower fraction of the star flux.

the observation. As shown in the legend, each of the contrast curves in Figure 7.2 corresponds to a different reduction of 50 consecutive frames of the TYC 1355-214-1 dataset. The contrast curves are color-coded based on the amount of field rotation in each reduction, so that the black lines indicate the contrast ratio for reductions with low amounts of field rotation ($\sim$12°–35°) while the red lines display the contrast ratio for subgroups with a large amount of field rotation ($\sim$150°). Beyond $\sim$0.8", all of the contrast curves are roughly similar, but at separations $\lesssim$0.8" the subgroups with higher amounts of field rotation have noticeably better contrast curves. At 0.4", for example, the reductions with $\gtrsim$150° of field rotation are sensitive to companions less than 10^{-5} times as bright as the star. However, the reductions with $\lesssim$40° could not detect a companion at 0.4" from the star unless it had a relative brightness of $\gtrsim 2\times10^{-5}$. Moving slightly closer to the star, the reductions with $\gtrsim$150° of field rotation could reveal a planet only 2×10^{-5} times as bright as the star at a separation of 0.3", but the reductions with $\lesssim$100° of field rotation are limited to companions at least 4×10^{-5} as bright as the star.

The factor of two difference in the sensitivity of the TYC 1355-214-1 reductions with the highest and lowest amounts of field rotation at both 0.4" separation and 0.3" separation raises the question of whether that scaling relation extends to other separations as well. In Figure 7.3, we plot the sensitivity of all of the 50-frame reductions of the TYC-1355-214-1 dataset relative to the sensitivity of the subgroup with the highest amount of field rotation (rot 15: 156.36°). Since the relative sensitivity is determined by dividing the contrast curve for each reduction by the contrast curve for rot 15, relative sensitivities close to 1 mean that the two contrast curves are very similar while higher relative sensitivities indicate that the reduction of rot 15 achieves significantly higher contrast. As illustrated in Figure 7.3, the importance of field rotation increases with decreasing separation from the star. At 0.25", for example, the reduction with 156.36° of field rotation is sensitive to companions eight times fainter

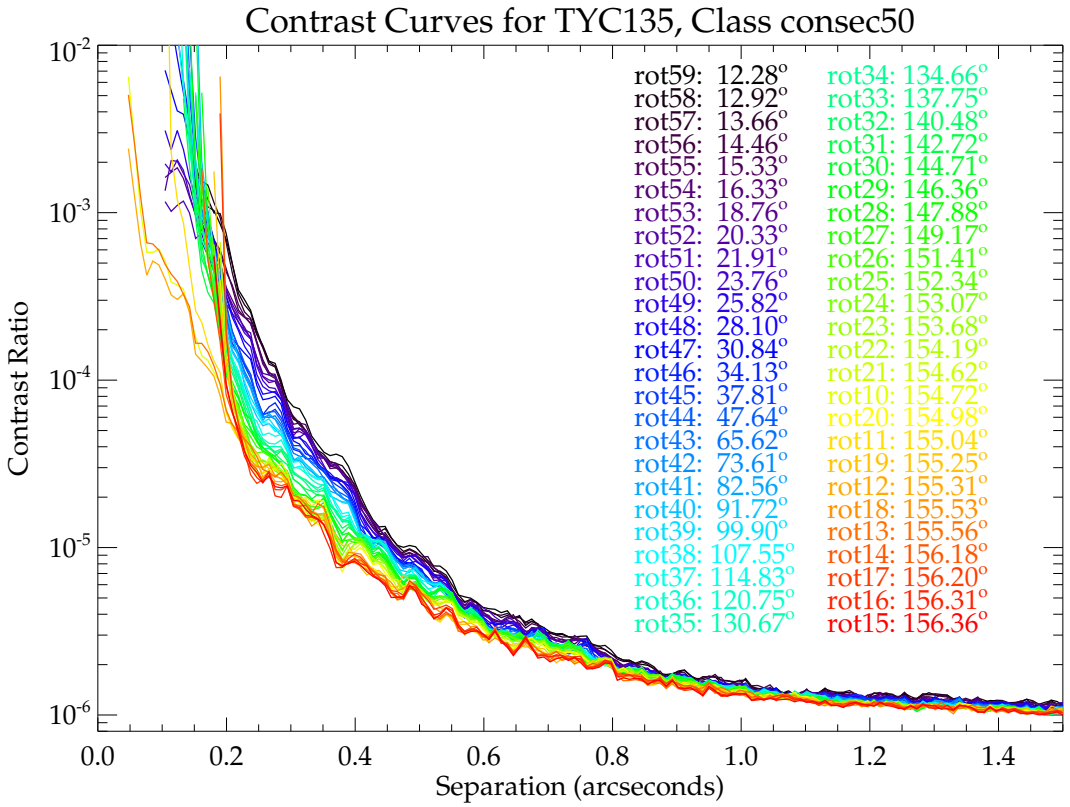

Figure 7.2: Contrast curves for 50-frame reductions of TYC 1355-214-1. For the rotation analysis, the TYC 1355-214-1 dataset was divided into fifty reduction subgroups with fifty consecutive frames in each group. The colored lines display the contrast curves for each of the reduction subgroups, color-coded and sorted in order of increasing field rotation. At wide separations ($\gtrsim$1"), all of the reduction subgroups reach a contrast ratio of 10^{-6} independent of the amount of field rotation in the subgroup. Closer to the star, the rotation groups with higher amounts of field rotation (represented by orange lines) are sensitive to less luminous companions than the reduction subgroups with less field rotation (indicated by blue lines). Only a few of the rotation subgroups with $\gtrsim$150° of field rotation are sensitive to companions within 0.1" of the star.

than the faintest companion that could be detected by the reductions with $<13^\circ$ of field rotation. At the same separation, the reductions with $\sim 100^\circ$ of field rotation are approximately half as sensitive as the reduction with the maximum possible field rotation for the class.

Closer to the star the influence of rotation rate is even more pronounced. Because a frame must rotate by a threshold level to be included in the image subtraction and optimization process at each annulus (see the discussion of the LOCI algorithm in Subsection 3.2.1), fewer frames can be used to optimize the innermost annuli for the reductions with relatively low amounts of field rotation. Accordingly, the inner working angle (IWA) for the reductions with relatively low amounts of field rotation is greater than the IWA for the reductions with relatively high amounts of field rotation. For the purpose of this rotation study, we will define the inner working angle as the closest angular separation at which a reasonable contrast curve is computed. Because the density of contrast curves plotted in Figure 7.2 makes it difficult to distinguish the starting point of each contrast curve, Figure 7.4 displays the angular separations corresponding to several different contrast levels as a function of the amount of field rotation. Each point along the x-axis therefore represents a different reduction of the TYC 1355-214-1 dataset. As shown in the top panel of Figure 7.4, the minimum separation from the star at which a contrast ratio of 10^{-5} is be achieved is $\sim$0.45" for the reductions with $\lesssim 30^\circ$ of field rotation, but decreases slightly to $\sim$0.42" if the dataset contains $\gtrsim 150^\circ$ of field rotation. Beyond $\sim 152^\circ$ of field rotation, the required separation seems to vary between $\sim$0.42" and $\sim$0.37".

The lower panel of Figure 7.4 provides a closer view of the contrast levels for rotation angles between 148° and 158°. The separation necessary to reach a contrast ratios of 10^{-5} is nearly constant ($\sim$0.42") for rotation angles between 148° and 154.5°, but the required separation decreases to 0.37" when the rotation angle increases past 154.5°. Aside from a slight jump back to 0.4" for the reduction with $\sim 155.3^\circ$ of

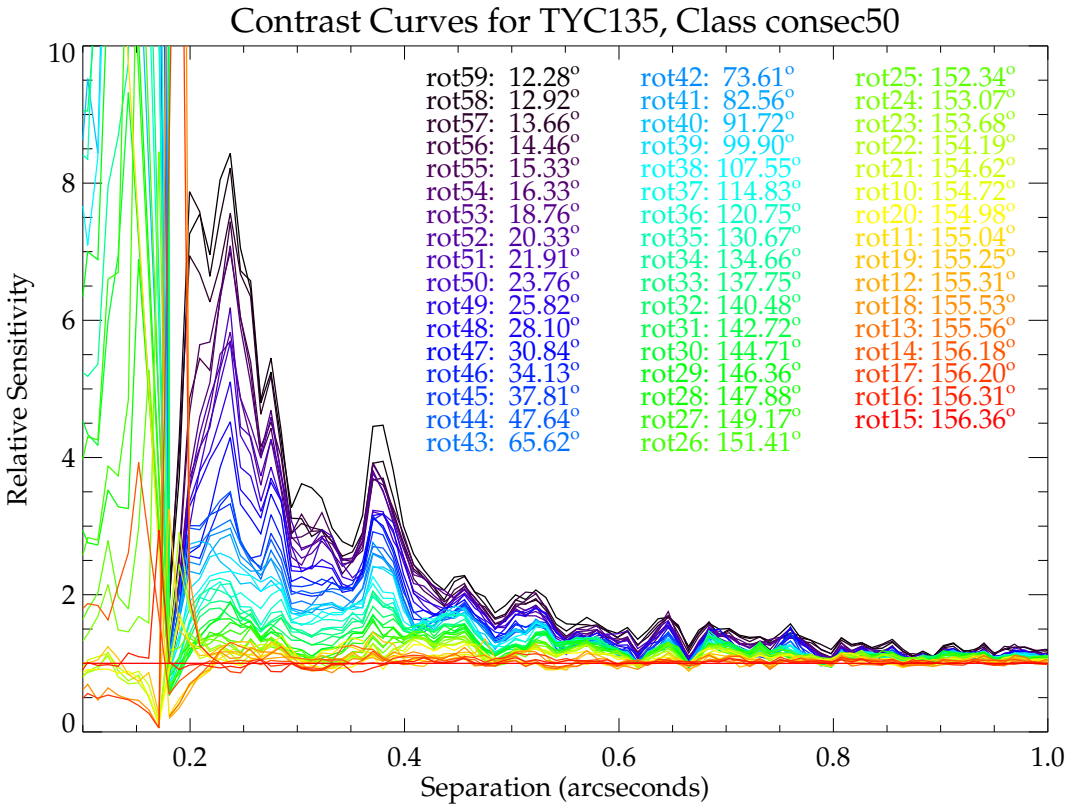

Figure 7.3: Relative sensitivity for the 50-frame reductions of TYC-1355-214-1. The colored lines displays the contrast ratio of each rotation group divided by the contrast ratio for the group with the largest amount of field rotation (rot 15: 156°). At small separations, the sensitivity of the reduction is highly dependent on field rotation. For instance, at 0.2" from the star, the reductions with smallest amount of field rotation ($\sim$12°) are less than eight times as sensitive as the reduction of group 15. As the separation from the star increases, the spread in the sensitivity of the reductions decreases. At separations of 0.5" all of the reductions are at least half as sensitive as the reduction of group 15, and the reductions have nearly identical contrast ratios for separations $\gtrsim$0.8".

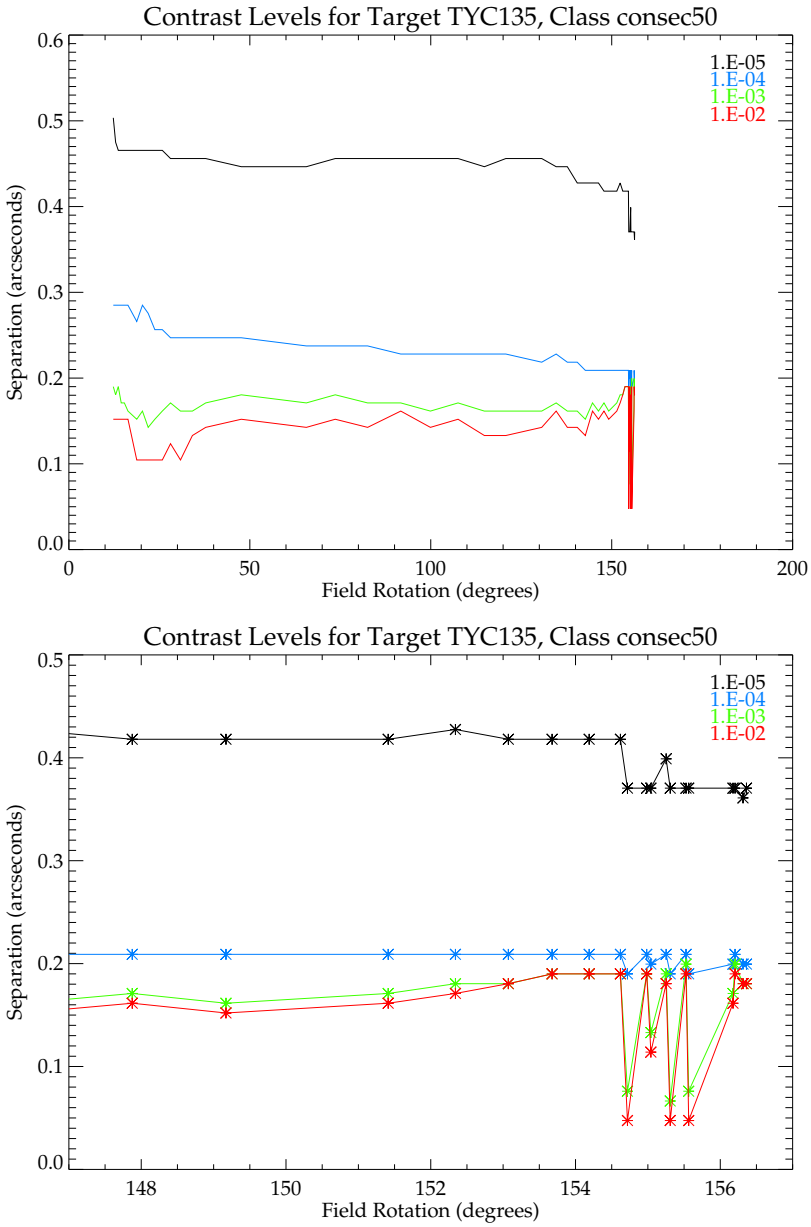

Figure 7.4: Contrast levels for 50-frame reductions of TYC 1355-214-1. **Top:** Each line plots the minimum angular separation at which the indicated contrast ratio is achieved as a function of field rotation. The black line representing the angular separation at which the contrast ratio first reaches 10^{-5} is roughly constant for field rotations between 10° and 130°, but the angular separation decreases from ∼0.45" to ∼0.42" for field rotation $\gtrsim$130°. **Bottom:** This plot shows a higher-resolution view of the top plot for field rotation between 146° and 156°. For the reductions with field rotations between 154.5° and 156°, the angular separation at which contrast ratios of 10^{-2} and 10^{-3} varies between ∼0.2" and ∼0.4". This odd behavior prompted the author to resort the reductions by time of acquisition.

field rotation, the minimum separation at which a contrast of 10^{-5} is achievable remains at 0.37" for the remainder of rotation angles in the sample. Although the separation required to reach a contrast ratio of 10^{-5} is approximately constant for rotation angles $\gtrsim$154.5°, the separations required to achieve lower contrast ratios of 10^{-2}, 10^{-3}, and 10^{-4} vary significantly for rotation angles between 154.5° and 156.4°. Since the fractional difference in field rotation is small ($\sim$1%), the variations in the required separation likely reflect small variations in the behavior of the PSF or a slight frame misregistration during the reduction process rather than the minute changes in the amount of field rotation.

We can test the hypothesis that the variability in the required separation is due to the changing shape of the PSF by sorting the reduction subgroups based on the time of acquisition instead of the amount of field rotation. As noted in the legend of Figure 7.4, the rotation subgroups with the largest amounts of field rotation were taken both before and after the transit of TYC 1355-214-1. Sorting the reduction subgroups by the total amount of field rotation therefore disrupted the temporal ordering of the subgroups (indicated by the "rot##" name of each subgroup listed in the legend).

After resorting the subgroups by name instead of by the amount of field rotation, we produce the plot of the contrast limits versus the rotation group number shown in Figure 7.5. Now that the original temporal sequence of the reduction groups has been reinstated, we see that the oscillatory behavior of the contrast levels has disappeared. Instead, Figure 7.5 clearly shows that the minimum separations at which contrast levels of 10^{-2} and 10^{-3} are achieved were much smaller before the peak rotation rate was reached (groups 10–13) than after the peak rotation was reached (groups 14–20). Accordingly, when the rotation subgroups were sorted by increasing amounts of field rotation, the increase in the minimum possible separations near group 14 caused the resulting plot of minimum separations versus total amount of field rotation to alternate between the larger separations required for groups 14–20 and the smaller

separations possible for groups 10–13. The slight jump in the minimum separation for rotation group 11 (0.13" for 10^{-3} contrast compared to 0.05" for groups 10, 12, 13, 14) is likely indicative of a slight misregistration error during the reduction of group 11. An alternative explanation is that one of the frames used in the reduction of group 11 suffered from poorer AO performance than the frames in groups 10, 12, 13, and 14, but given that all of the frames used in the rotation study were visually inspected, this explanation seems unlikely. Furthermore, since 49 of the 50 frames in rotation group 11 are identical to the frames included in groups 10 and 12, a registration error seems to be a more probable explanation for the increase in the required separation for group 11 than poor AO performance for one or more of the group 11 frames.

While the slight increase in the minimum separations required to achieve contrasts of 10^{-2} and 10^{-3} for group 13 appears unlikely to have been caused by a change in the shape of the PSF, the sustained jump in the minimum separation that occured between groups 13 and 14 might be due to changes in AO performance or atmospheric conditions. Since the total field rotation is nearly identical for groups 10–24, the increase in the minimum separation after group 13 is unlikely to be explained by a decrease in the number of frames that achieve sufficient field rotation to be included in LOCI. Rather, the most plausible explaination is that atmospheric conditions and/or AO performance worsened between groups 13 and 14 so that the minimum separations increased even though the total field rotation remained roughly constant. The difference in the minimum separations could also be explained by misregistration errors, but that explanation seems less likely because of the nearly flat nature of the 10^{-4} contrast level between groups 10 and 32. Another possible lesson that might be extracted from the variability of the 10^{-2} and 10^{-3} contrast levels for groups 10-15 is that contrasts ratios reported for separations of less than 0.2" are not as stable as contrast ratios determined for larger separations. This conclusion cannot be drawn from the 50-frame reduction of TYC 1355-214-1 alone, however, so we will reserve

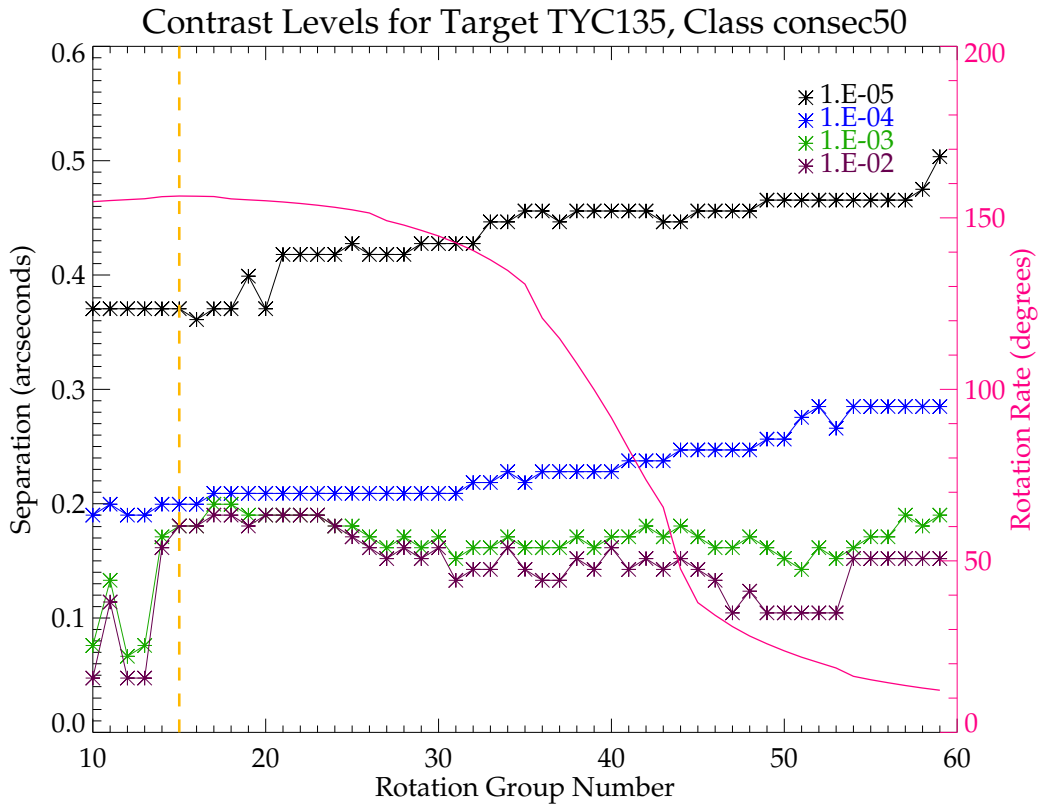

Figure 7.5: Contrast levels versus rotation group for 50-frame reductions of TYC 1355-214-1. The black, blue, green, and purple lines marked with asterisks are associated with the left axis and indicate the minimum separation at which the appropriate contrast is achieved for each of the rotation subgroups. The rotation subgroups were created numerically, so plotting them in numerical order is equivalent to plotting them in temporal order. The pink line is associated with the right axis and displays the total amount of field rotation for each of the rotation subgroups. For clarity, the dashed orange line indicates the rotation subgroup corresponding to the maximum amount of field rotation. As discussed in the text, decreasing the amount of field rotation causes the innermost separation at which a given contrast can be achieved to move outward to greater angular separations.

this question for after the contrast curves for the other reduction classes have been examined.

7.4.2 Reduction of HD 23912

The 175-frame HD 23912 dataset was reduced in classes of 50-frames and 90-frames. As mentioned in Section 7.2, the 50-frame (100-frame) HD 23912 reduction subgroups are offset by five (ten) frames instead of the usual one frame in order to reduce the computer time required to sample the full range of rotation angles present in the HD 23912 dataset. Accordingly, the twelve 50-frame reductions of the HD 23912 dataset probe rotation angles between 5.9° and 43.2°, and the sixteen 100-frame reductions cover rotation angles between 18.3° and 61.1°.

Due to the wide range of rotation angles investigated, the HD 23912 dataset is well-suited for examining the behavior of the inner working angle as a function of field rotation. In Figure 7.6, we plot contrast curves for the 50-frame reductions of HD 23912. The top panel of Figure 7.6 displays the contrast ratio determined by *photo_contrast.pro* for separations <1", and the bottom panel indicates the relative sensitivity of each reduction compared to the reduction of the group with the highest amount of field rotation (group 0, 43.2°). In both panels, the contrast curves are color-coded according to the total field rotation of each of the reduction groups.

Looking at either panel of Figure 7.6, we see that the reductions that span >20° of field rotation have contrast curves that extend to within 0.1" of the star. Once the field rotation decreases to ∼10°, however, the minimum separation at which a companion could be detected increases to ∼0.2". For the two reductions with the least amount of field rotation (rot 11: 6.59°, rot 12: 5.93°), companions cannot be detected at separations smaller than ∼0.3". Given the ∼4–200 pc distances to the stars targeted by the SEEDS project, an angular separation of 0.3" corresponds to a physical separation of 1.2–60 AU, while an inner working angle of 0.1" would allow the SEEDS team to image companions within 0.4–20 AU of the star. Since Jupiter and Neptune lie 5.2 and 30 AU from the Sun, respectively, reducing the inner working angle to 0.1" is preferable if the SEEDS team hopes to image Jovian planets at

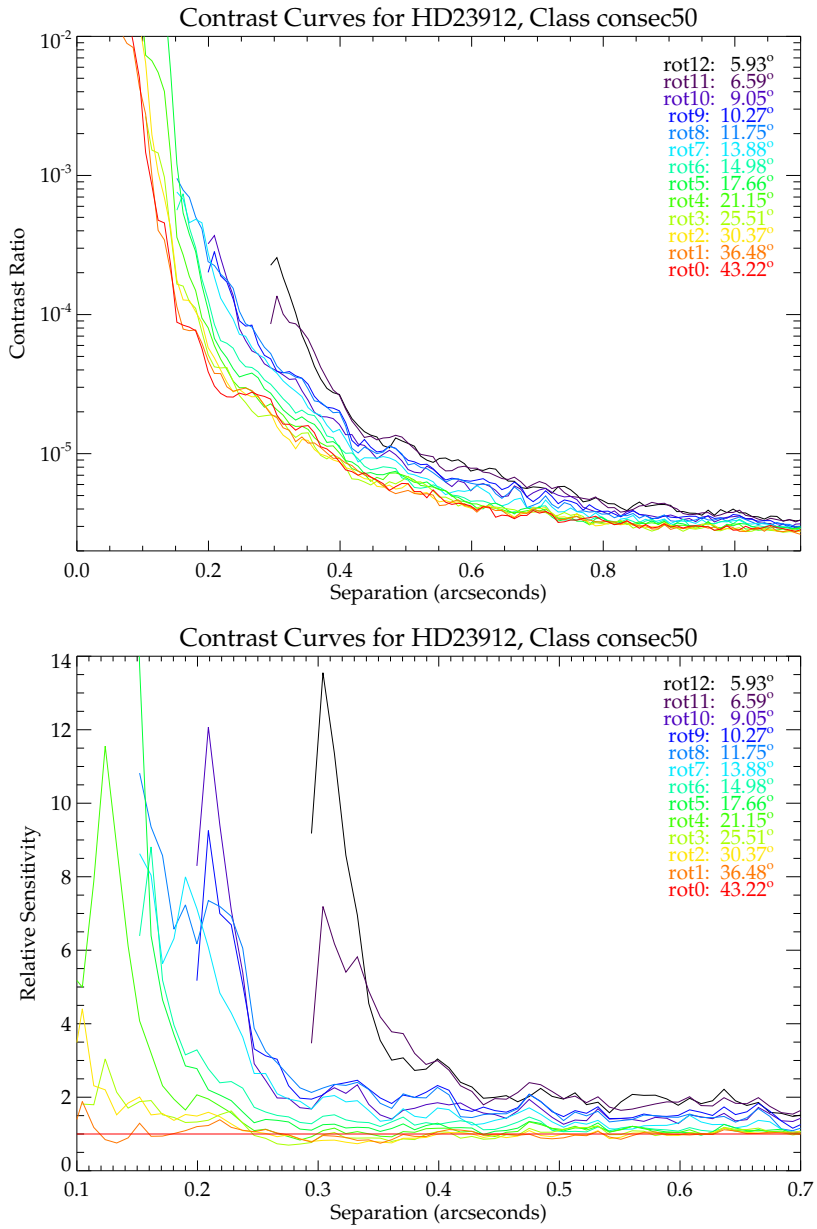

Figure 7.6: Contrast curves for 50-frame reductions of HD 23912. **Top:** The contrast ratio of each reduction as a function of separation. The reductions with the most field rotation achieve noticeably higher contrast ratios at all angular separations. **Bottom:** The relative sensitivity of each reduction as a function of separation. Note the poor performance of rot 12 and rot 11 relative to the other reductions.

separations like those observed in our solar system. While obtaining a smaller inner working angle is clearly desirable, deciding how much time to allocate to each target is a significantly more complicated issue and we will discuss that topic in more detail in Chapter 8.

In addition to reducing the inner working angle, increasing the total field rotation from 5.93° to 43.22° also improves the sensitivity of the final image as shown in the bottom panel of Figure 7.6. Relative to the reduction of rot 0, which has the highest amount of field rotation (43.22°), the other twelve reductions are as much as thirteen times less sensitive at separations less than 0.5". As expected, the least sensitive reductions are the ones with the lowest amount of field rotation (rot 12: 5.93°, rot 11: 6.59°), and the all of the reductions become more sensitive at higher separations.

An interesting question to consider when examining Figure 7.6 is at what separation do rotations with lesser amounts of field rotation reach the same sensitivity as reductions with significantly more field rotation. Looking at the lower panel, we see that the contrast curve for rot 1 (36.48°) is very similar to the constrast curve for rot 0 (43.22°). Between separations of 0.11" and 0.22" the contrast ratio for the rot 1 reduction is within a factor of 1.5 of the contrast curve for rot 0, and the two curves differ by even less than that for separations beyond 0.22". Accordingly, the additional 6.74° of field rotation in rot 0 do not seem to dramatically improve the contrast of the reduction relative to the contrast achieved by the reduction of rot 1.

For the 30.37° and 25.51° of field rotation sampled by rot 2 and rot 3, respectively, the contrast is within a factor of 2 of the contrast achieved by the rot 0 reduction for separations $\gtrsim$0.13", and the relative sensitivity drops to <1.5 for separations beyond $\sim$0.18". This strong similarity suggests that there is not a strong disadvantage to observing targets like HD 23912 with $\sim$25° of field rotation instead of $\sim$45° unless the goal of the observation is to detect objects within 0.18". In that case, the improvement in sensitivity caused by increasing the amount of field rotation might justify taking

time away from another target in order to increase the amount of field rotation in the observation. Once the amount of field rotation in the subgroup decreases to $\sim$21°, however, the difficulty of detecting companions within 0.18" increases dramatically, so observers wishing to search for companions at close separations should obtain at least $\sim$21° of field rotation in their dataset.

At wider separations, the subgroups with $\gtrsim$15° of field rotation all have relative sensitivities <2 for separations >0.24", and relative sensitivities <1.5 for separations >0.27". Accordingly, observations with only $\sim$15° of field rotation may be sufficient for observers looking for objects at separations $\gtrsim$0.24". Decreasing the amount of field rotation to $\sim$10° expands the IWA (from <0.1" to $\sim$0.2") and further reduces sensitivity, but the contrast curve reaches a factor of two of the rot 0 contrast curve at separations $\gtrsim$0.28". Depending on the goals of the observers, the increase in the IWA and the decrease in contrast caused by observing with only $\sim$10° of field rotation may be sufficient, but field rotations of $\lesssim$7° are unlikely to produce satisfactory results. The subgroups with the least amount of field rotation (rot 12: 5.93°, rot 11: 6.59°) are less than half as sensitive as the rot 0 subgroup for separations as large as $\sim$0.63". Even for the nearest SEEDS targets ($\sim$4 pc), an angular separation of 0.6" corresponds to a physical distance of 2.4 AU. The corresponding physical separation increases to 18 AU for the most distant (30 pc) stars in the SEEDS nearby stars category (see Section 4.3.1), so observations with $\lesssim$7° of field rotation are unlikely to be useful for the SEEDS project unless the targets observed are within $\sim$10 pc of the Earth.

Another area of investigation that can be explored with the HD 23912 dataset is whether longer sequences of frames taken when the target is rotating rather slowly can result in the same sensitivity as a smaller number of frames taken during transit. If so, then observers could conduct high-sensitivity ADI observations of several targets with similar right ascensions during a single night by altering the integration time for each

target to compensate for changes in the rotation rate at the time of the observation. To explore this issue, we compare the sensitivity of the 50-frame HD 23912 reductions with the 100-frame HD 23912 reduction.

We begin by discussing the results of the 100-frame reductions of HD 23912. The upper panel of Figure 7.7 displays the contrast curves for all sixteen 100-frame reductions, and lower panel plots the sensitivity of each reduction relative to rot 0, which covers 61.14° of field rotation. As shown in the upper panel, all of the reductions reach a contrast ratio of $\sim 2\times10^{-6}$ for angular separations $\gtrsim$0.8". Between 0.2" and 0.3", however, the lower panel of Figure 7.7 reveals that the reductions with the highest amounts of field rotation can detect companions 2–4 times fainter than the reductions with smaller amounts of field rotation.

Compared to the contrasts shown for the 50-frame reductions in Figure 7.6, the 100-frame reductions reach slightly higher contrast ratios ($\sim 2\times10^{-6}$ at 0.8" for the 100-frame reductions versus $\sim 3\times10^{-6}$ for the 50-frame reductions). Additionally, the relative sensitivities of the 100-frame reductions display less variation as function of field rotation compared to the 50-frame reductions. The higher contrast and increased similarity of the 100-frame reductions might be due to the greater number of frames in the frames in the 100-frame reduction or to the higher field rotations probed by the 100-frame class (18°–61°) compared to the 50-frame class (6°–43°).

Now that we have established that contrast curves of the 100-frame reductions exhibit the same general trends in sensitivity as a function of field rotation as the contrast curves of the 50-frame reductions, but at slighly higher contrast, we will turn our attention to whether an increased number of frames can compensate for a decreased amount of field rotation. In Figure 7.8, we plot contrast curves from the 50-frame and 100-frame rotation classes as well as the contrast curve produced by reducing the entire HD 23912 dataset. Rather than complicate the plot by color-coding the contrast curves by rotation rate, the color-coding in Figure 7.8 merely

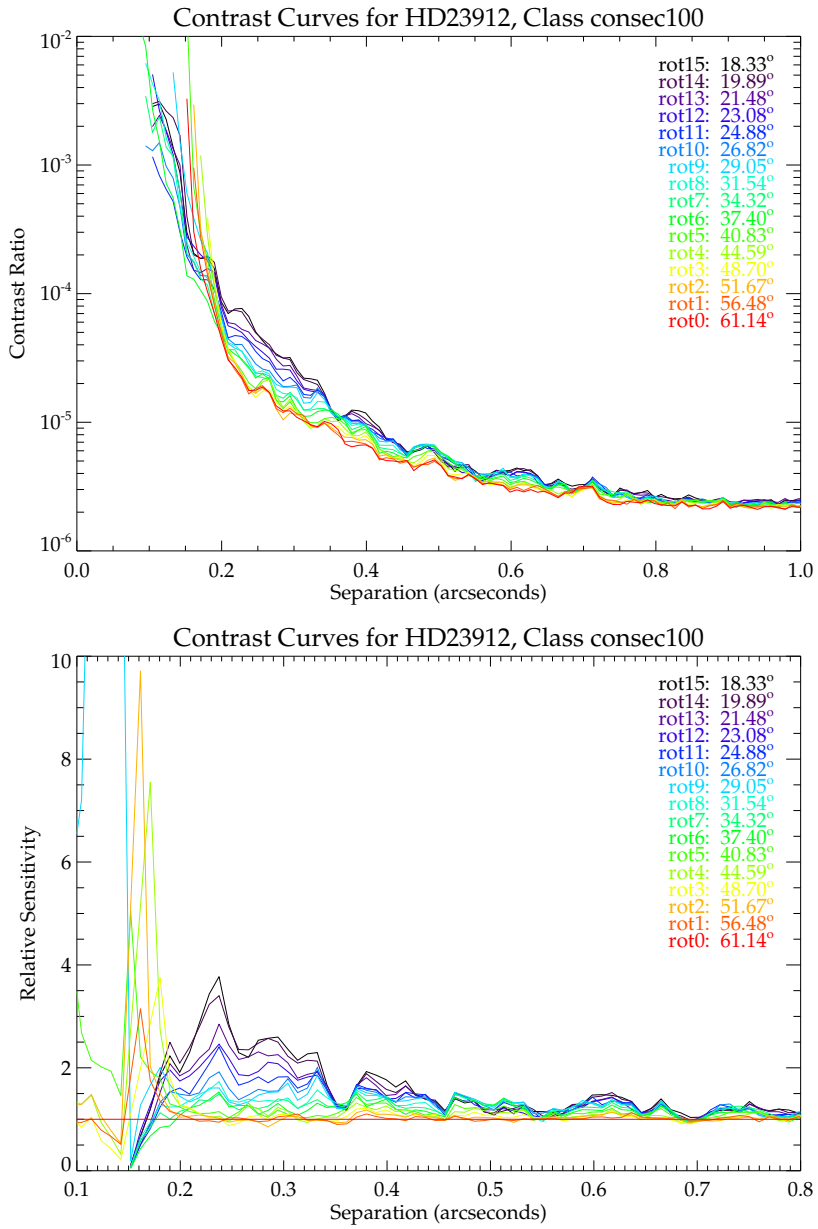

Figure 7.7: Contrast curves for 100-frame reductions of HD 23912. **Top:** The contrast ratios for each reduction as a function of field rotation. For separations $\gtrsim$0.8", all of the reductions have nearly identical contrast ratios. **Bottom:** The relative sensitivities for each reduction as a function of field rotation. The sensitivity at separations between 0.2" and 0.4" increases with increasing field rotation.

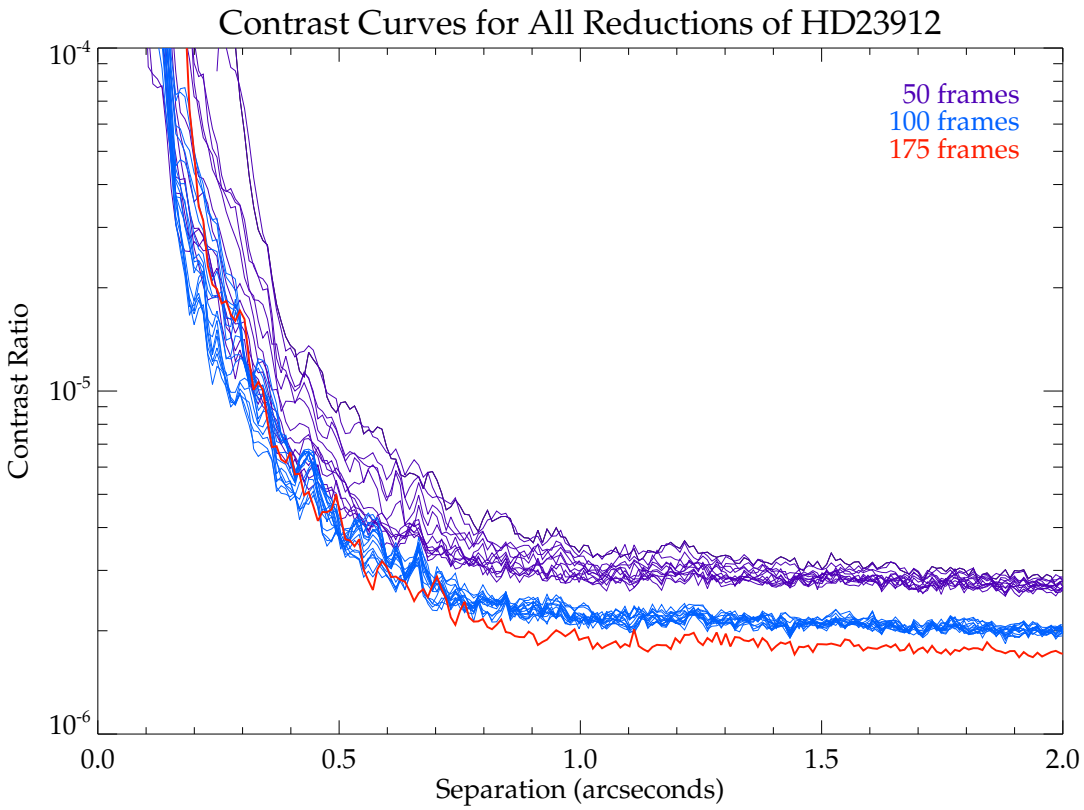

Figure 7.8: Contrast curves for all reductions of HD 23912. The purple lines display the contrast ratios for all of the 50-frame reductions of the HD 23912 dataset as a function of separation. The contrast ratios for the 100 frame reduction and the full 175-frame dataset are shown in blue and red, respectively. The 175-frame reduction achieves significantly higher contrast than the 100-frame or 50-frame reductions for separations $\gtrsim$1".

indicates the number of frames in each reduction. The differences between the contrast curves are most apparent at wide angular separations. Between 1" and 2", the 50-frame reductions reach a contrast ratio of $\sim 2.7\times10^{-6}$, while the 100-frame reductions have a higher contrast ratio of $\sim 2\times10^{-6}$. As expected, the reducing the full 175-frame dataset results in an even higher contrast ratio of $\sim 1.7\times10^{-6}$. At smaller separations, the 50-frame class still underperforms the 100-frame class and the full reduction, but the 100-frame class and full reduction yield overlapping contrast curves.

The similarity between the full reduction and the 100-frame reductions is strongest for separations of 0.3–0.5", which suggests that 16 minutes (100 frames) of integra-

tion might be as effective as 28 minutes (175 frames) for imaging companions at separations $\lesssim$0.5" around targets of the same luminosity as HD 23912 under similar observing conditions. If this conclusion holds, then the observing time for some targets could be significantly reduced without substantially decreasing the sensitivity of the observations at the innermost separations. However, shortening the integration time would decrease the contrast ratio achieved a wider separations and prevent the SEEDS team from making serendipitous discoveries of objects at greater separations. Additionally, although this analysis of the HD 23912 dataset suggests that the integration time for this particular target could have been reduced without decreasing the contrast inside 0.5", that statement may not hold in general. Additional observations of targets with a range of apparent magnitudes and rotation rates must be examined to investigate whether there is a universal threshold above which increasing the number of frames no longer improves the sensitivity of an ADI observation at small angular separations. Even if the threshold does not exist, such a study might reveal that there is a point at which the increase in sensitivity due to increasing the number of frames is small enough that the scientific value of further improving the sensitivity of one target is lower than the scientific value of devoting that time to observing another target.

7.4.3 Reduction of GJ 758

As discussed in Section 7.2, the GJ 758 dataset contains far fewer frames than the other three datasets. Accordingly, we divided the 45-frame dataset into rotation classes of 25, 30, 35, or 40 frames. The subgroups in the 25-frame class span $\sim$10° of field rotation (10°–22.8°), while the subgroups in the 35-frame class and the 40-frame class have total field rotations that differ by less than a degree. Accordingly, the subgroups in the 35-frame and 40-frame reduction classes are expected to yield very similar contrast curves while the subgroups in the 25-frame and 30-frame classes are expected to display more variation in sensitivity due to the wider range of field rotations in those classes.

For the 25-frame class, increasing field rotation does seem to increase sensitivity, as shown in Figure 7.9. The top panel of Figure 7.9 displays the contrast ratios for each of the 25-frame reductions of GJ 758, and the bottom panel displays the sensitivity of each reduction relative to the contrast ratio for the group with the largest amount of field rotation (rot 14: 22.8°). At separations $\gtrsim$0.4", the contrast curves for all of the reductions overlap and there is not significant improvement in sensitivity due to greater amounts of field rotation. Between 0.2" and 0.4", however, the groups with $\sim$22° of field rotation achieve noticably different contrast ratios than the groups with only $\sim$10° of field rotation.

The difference in the sensitivity of the reductions with $\sim$22° of field rotation and $\sim$10° of field rotation is particularly evident in Figure 7.10. The contrast curves and relative sensitivities displayed in Figure 7.10 are the same as those shown in Figure 7.9, but the color scaling has been redone so that all of the groups with $\sim$22° of field rotation are plotted in red while the groups with $\sim$10° of field rotation are plotted in blue. This simple color division clearly shows that the reductions with $\sim$10° of field rotation have inner working angles of $\sim$0.23", while the reductions with $\sim$22° of field rotation can reveal companions as close to the star as $\sim$0.13". Additionally,

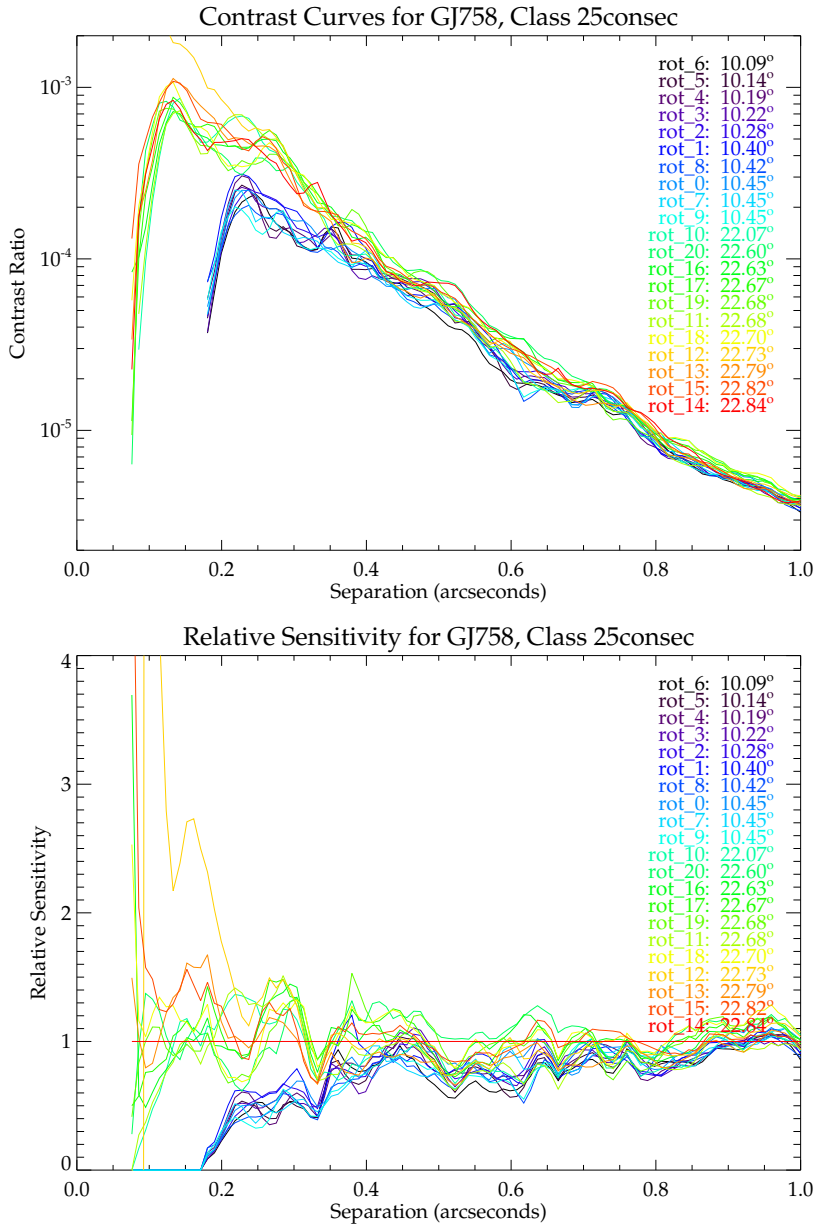

Figure 7.9: Contrast curves for 25-frame reductions of GJ 758. **Top:** Contrast ratios as a function of separation. Interestingly, the subgroups with less field rotation achieve higher contrasts ratios at separations between 0.2" and 0.4" than the subgroups with more field rotation. **Bottom:** Relative sensitivities as a function of separation. For separations $\gtrsim$0.7", all of the reductions acheive roughly the same contrast.

although the subgroups with ∼22° of field rotation are able to reveal planets at closer separation than the subgroups with only ∼10° of field rotation, the subgroups with less field rotation are actually more sensitive to planets at separations between 0.2" and 0.4". As shown in the bottom panel of Figure 7.10, the subgroups with ∼10° of field rotation reach contrasts 1.5–3 times higher than the contrasts reached by rot 14 for separations of ∼0.3".

The greater sensitivity of the reductions with less field rotation suggests that for the GJ 758 dataset, other factors might be more important than field rotation in determining image sensitivity. Although the reduction subgroups are only offset by one frame, all of the subgroups with ∼10° of field rotation begin earlier in the GJ 758 dataset than the subgroups with ∼22° of field rotation. Once possible explaination for the better performance of the subgroups with less field rotation at separations between 0.2" and 0.4" could be that the AO system performed better near the start of the GJ 758 observing sequence, which caused the frames in the subgroups with ∼10° of field rotation to have more stable PSFs than the frames in the subgroups with ∼22° of field rotation. As indicated before, however, the obvious weakness in this explanation is that most of the frames in each reduction group are shared by the other groups. In particular, the difference in the contrast ratios achieved for subgroups rot 9 (10.45°) and rot 10 (22.07°) would not be as sharp if the decreased sensitivity of the subgroups with ∼22° of field rotation at separations of 0.2"–0.4" is due to changes in the performance of the AO system. While changes in the AO performance may have contributed to the difference in the sensitivity of the subgroups with ∼10° and ∼22° of field rotation, AO performance is unlikely to be the sole explanation. After we examine the results of the reduction of the other GJ 758 classes, we will return to discussing the complicated relationship between field rotation and sensitivity for the GJ 758 dataset.

The next class of GJ 758 reductions is the 30-frame class including sixteen sub-

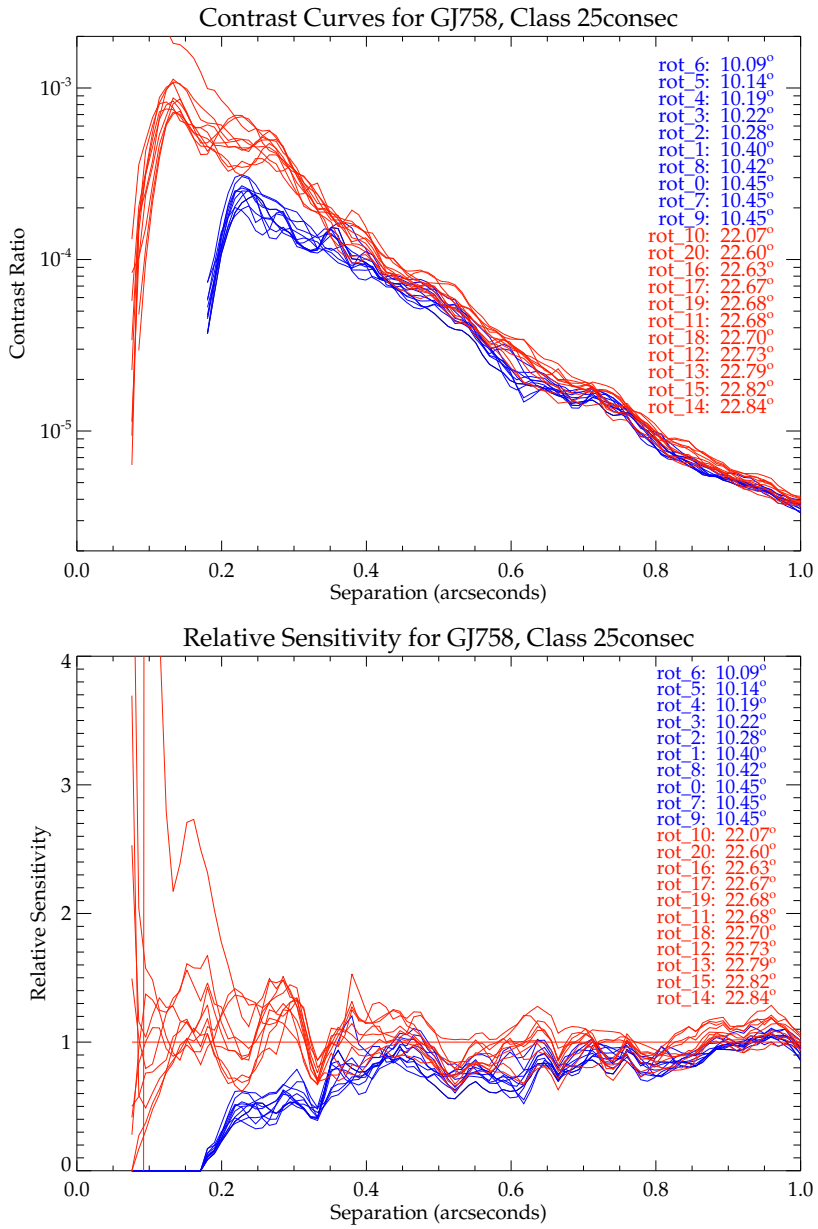

Figure 7.10: Contrast curves for 25-frame reductions of GJ 758. This figure displays the same data as Figure 7.9 but using only two colors. The blue lines represent subgroups with ∼10° of field rotation and the red lines represent subgroups with ∼22° of field rotation. **Top:** Contrast ratios as a function of separation. **Bottom:** Relative sensitivities as a function of separation.

groups with field rotations between 12.30° (rot 1) and 24.91° (rot 14). The contrast ratios for each of the subgroups are displayed in the top panel of Figure 7.11, and the sensitivity of each reduction relative to the reduction of rot 14 (24.91°) are shown in the bottom panel. Like Figure 7.9 for the 25-frame reductions, Figure 7.11 indicates that all of the subgroups reach approximately the same contrast ratio for separations beyond ∼0.5", but that the sensitivity at smaller separations depends on field rotation. As demonstrated for the 25-frame class, the contrast ratios for the 30-frame reductions follow two patterns: the subgroups with ∼24° of field rotations probe smaller separations than the subgroups with ∼12° of field rotation, but the subgroups with less field rotation reach higher contrast ratios for separations between ∼0.2" and ∼0.4".

The difference between the contrast ratios for the subgroups with ∼12° and ∼24° of field rotation is displayed more clearly in Figure 7.12. The contrast curves and relative sensitivities displayed in Figure 7.12 are the same as those shown in Figure 7.11, but the rainbow color-coding has been replaced by blue lines for reductions with ∼12° of field rotation and red lines for reductions with ∼24° of field rotation. Looking at the upper panel of Figure 7.12, we see that the subgroups with ∼24° of field rotation are sensitive to companions at separations as small as ∼0.13", but that the subgroups with only ∼12° of field rotation are limited to separations $\gtrsim$0.17". Since GJ 758 is 15.5 pc away, angular separations of 0.13" and 0.17" correspond to physical separations of ∼2 AU and ∼2.6 AU, respectively. All of the subgroups would therefore be sensitive to objects at Jupiter-like separations (∼5 AU) assuming that the objects were brighter than the contrast limit.

Focusing on the bottom panel of Figure 7.12, we see that the subgroups with ∼12° of field rotation are slightly more sensitive to objects ∼2–3 times fainter than the detection limit for rot 14 (24.91°) at separations near 0.3", but that the reductions with ∼24° of field rotation also display a range of sensitivities. For instance, Figure

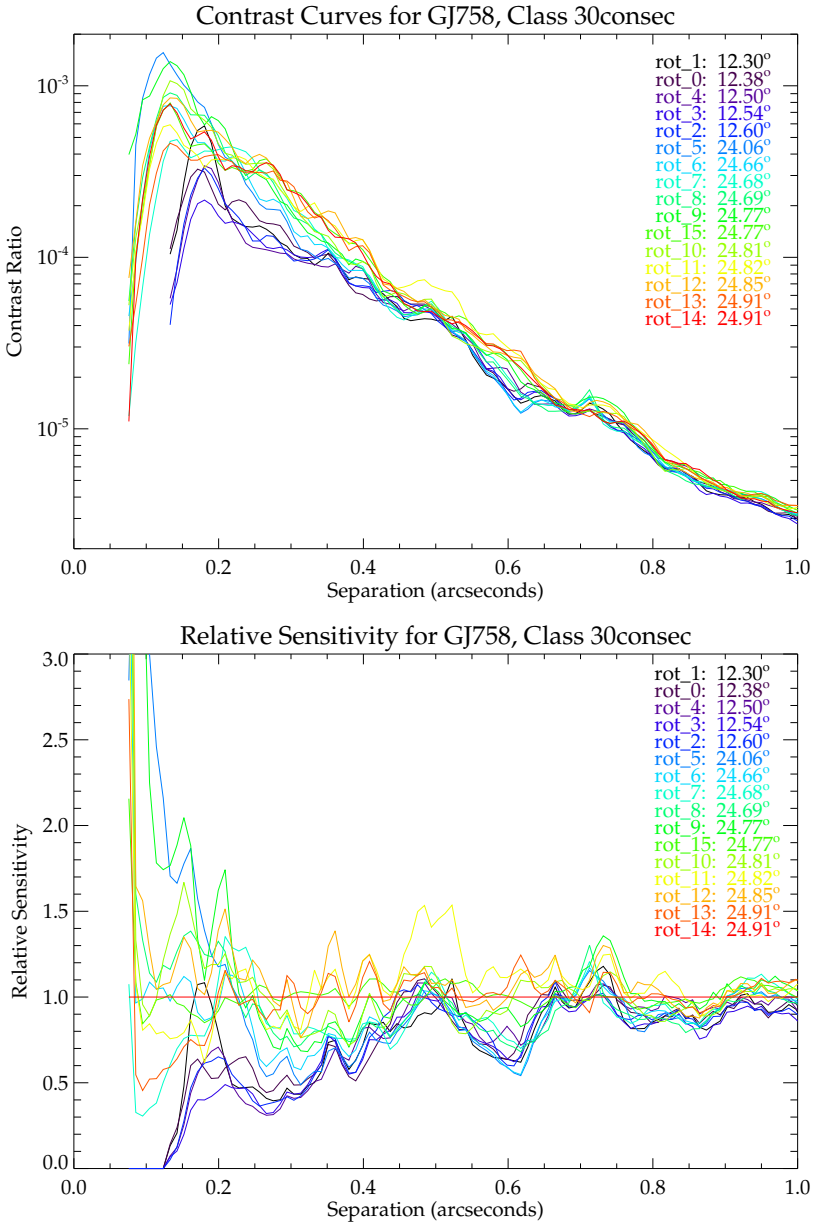

Figure 7.11: Contrast curves for 30-frame reductions of GJ 758. **Top:** Contrast ratios as a function of separation. The subgroups with ∼24° of field rotation are sensitive to companions ∼0.1" closer to the star than the subgroups with only ∼12° of field rotation. **Bottom:** Relative sensitivities as a function of separation. Note that as in Figure 7.9, the subgroups with less field rotation achieve higher contrast ratios at separations between 0.2" and 0.4".

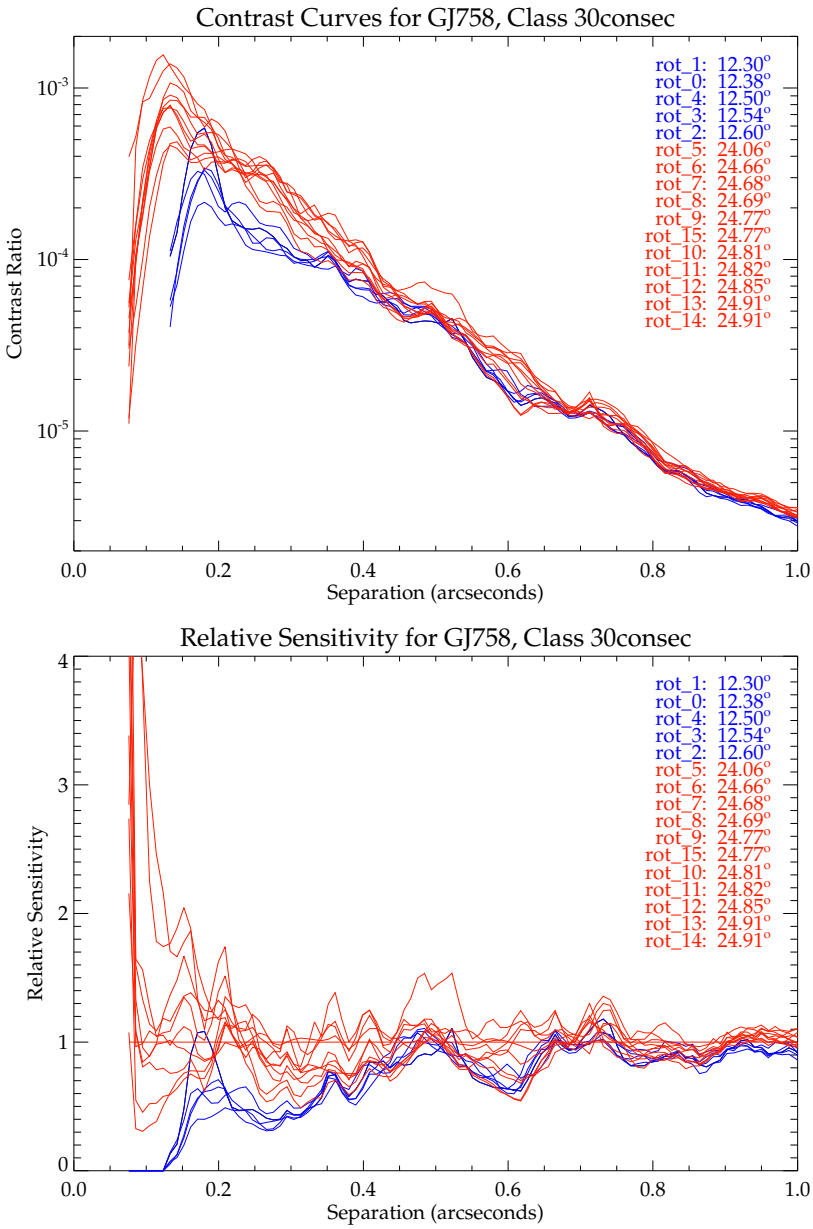

Figure 7.12: Contrast curves for 30-frame reductions of GJ 758. This figure displays the same data as Figure 7.11 but using only two colors. The blue lines represent subgroups with $\sim 10^{\circ}$ of field rotation and the red lines represent subgroups with $\sim 22^{\circ}$ of field rotation. **Top:** Contrast ratios as a function of separation. **Bottom:** Relative sensitivities as a function of separation.

7.11 reveals that rot 5 (24.06°) and rot 6 (24.66°) are approximately twice as sensitive as rot 14 (24.91°) at separations of ∼0.3". The decreased separation between the relative sensitivities of the subgroups with the lowest amount of field rotation and the highest amount of field rotation for the 30-frame reductions compared to the 25-frame reductions suggests that increasing the number of frames might help to reduce the influence of rotation rate on sensitivity.

Unfortunately, the total field rotations for the subgroups in the 35-frame (45-frame) class differ by less than 0.6° (0.29°), so we cannot determine whether the two distinct patterns of contrast curves observed for the reductions of the 25-frame class and the 30-frame class would also occur for reductions of subgroups with a larger number of frames. Instead, we will examine the contrast ratios for the 35-frame and 40-frame reductions to determine the relative influence of other factors on image sensitivity when field rotation is approximately constant. Figure 7.13 displays the contrast ratios and relative sensitivities for the 35-frame reduction, and Figure 7.14 presents the same information for the 40-frame reductions.

Looking first at Figure 7.13, we see that all of the 35-frame reductions have inner working angles of approximately 0.15". Additionally, the sensitivity of the reductions varies by a factor of 2 for angular separations between 0.2" and 0.6", but all of the contrasts curves lie within a factor of 1.5 of the contrast curve produced for rot 1 (26.88°) for separations beyond 0.6". In Figure 7.14, we see that the 40-frame reductions also have inner working angles of ∼0.15". Beyond that separation, the contrast curves for the 40-frame reductions are slightly more consistent than the contrast curves for the 35-frame reductions: the relative sensitivities of the 40-frame reductions are between 0.8 and 1.4 for separations between 0.2" and 1".

Although Figures 7.9–7.14 have revealed that the 35-frame and 40-frame classes are sensitive to companions at smaller separations than the 25-frame and 30-frame classes, it is easier to compare the relative sensitivities of each class by examining

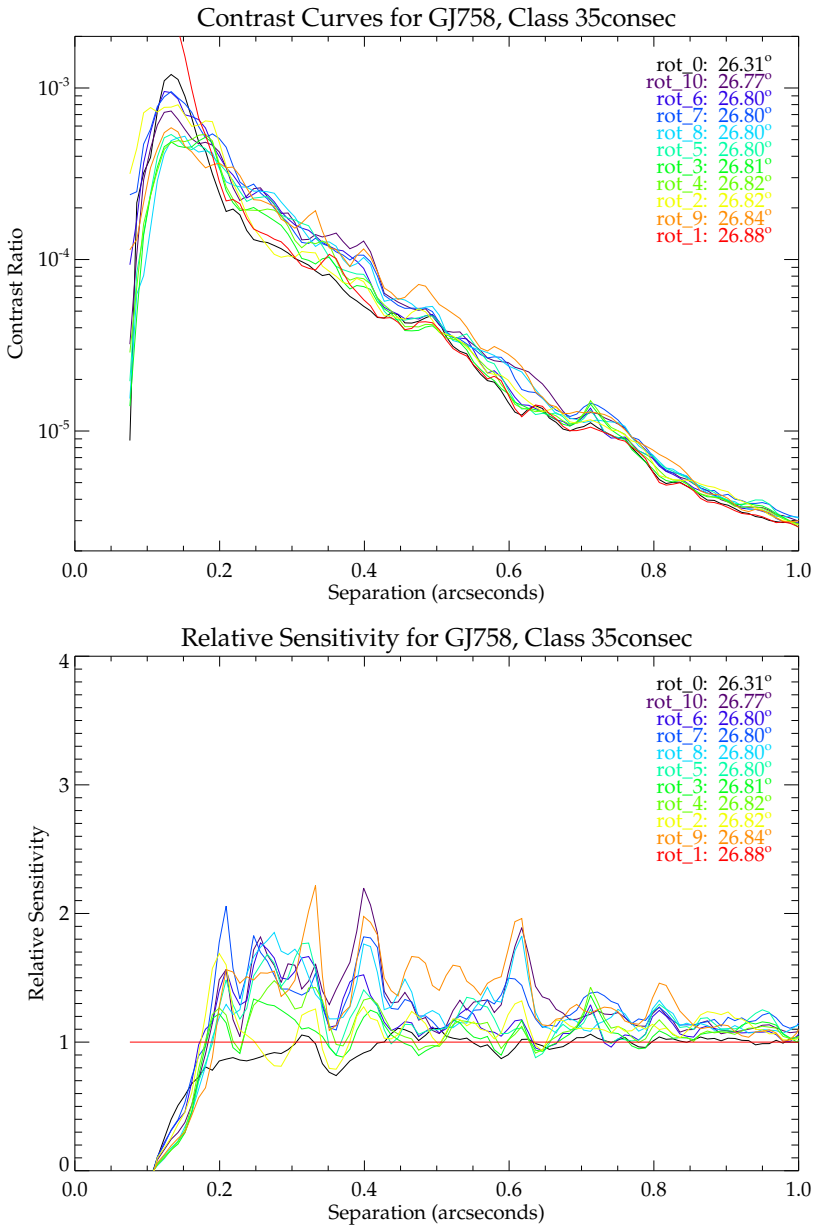

Figure 7.13: Contrast curves for 35-frame reductions of GJ 758. **Top:** Contrast ratios as a function of separation. All of the subgroups except for rot 1 achieve contrast ratios of $\sim 10^{-3}$ at separations of 0.2". **Bottom:**Relative sensitivities as a function of separation. The contrast ratios differ by a factor of two at separations $\lesssim$0.6", but they agree to within a factor of 1.4 at wider separations.

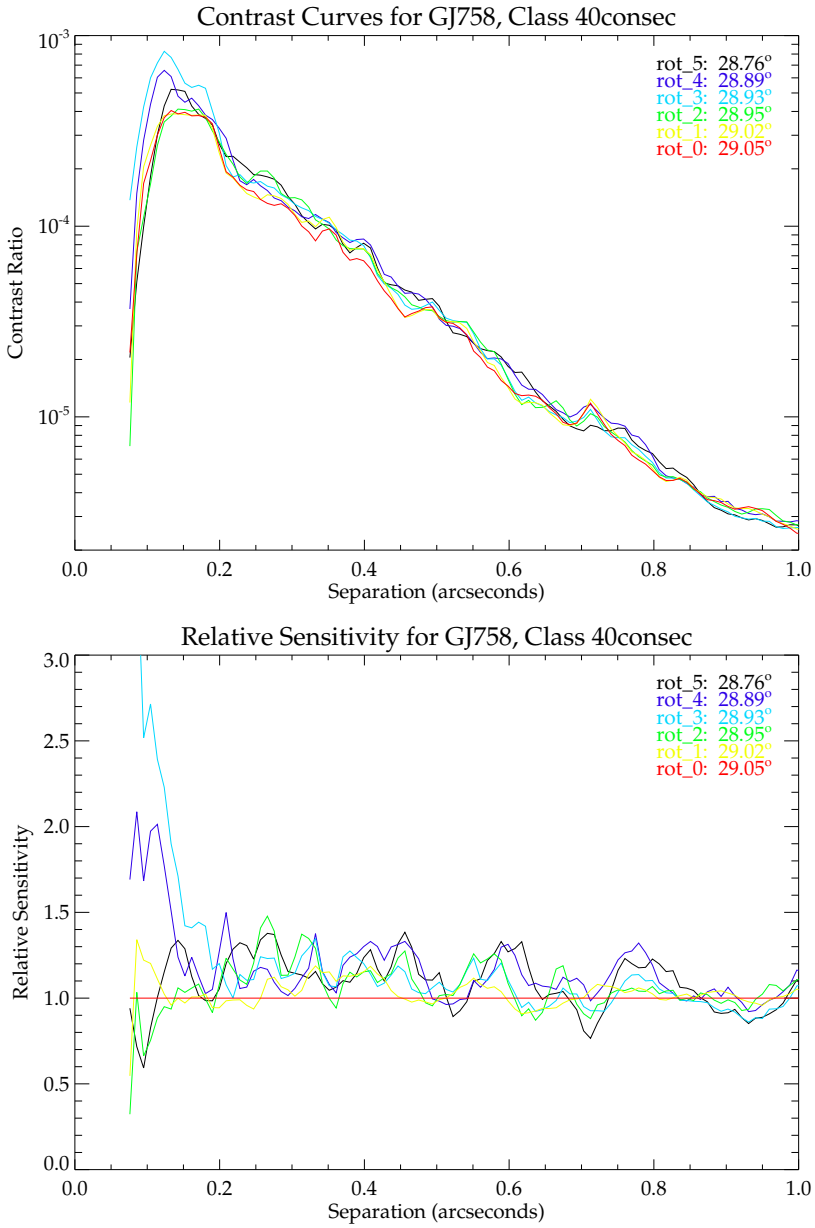

Figure 7.14: Contrast curves for 40-frame reductions of GJ 758. **Top:** Contrast curves as a function of separation. Note the high degree of similarity between the contrast ratios for separations $\gtrsim$0.2". **Bottom:** Relative sensitivities as a function of separation. For separations $\gtrsim$0.2", all of the contrast ratios agree to within a factor of 1.5.

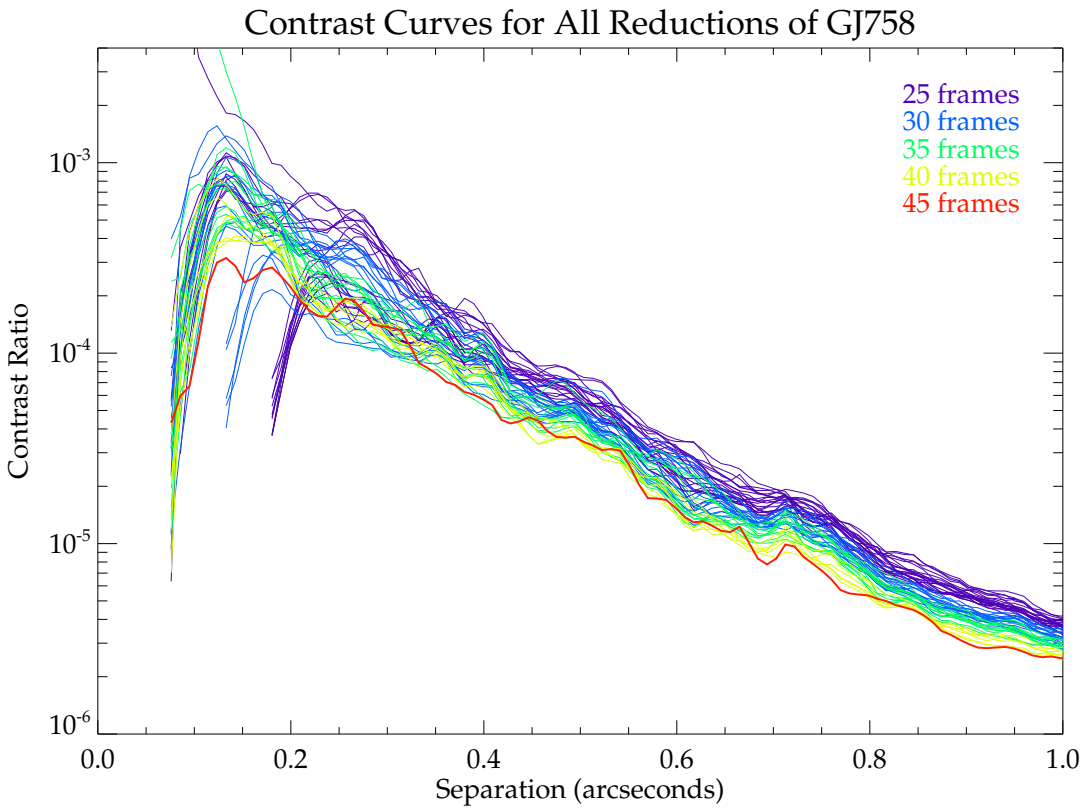

Figure 7.15: Contrast curves for all reductions of GJ 758. The purple lines display the contrast ratios for all of the 25-frame reductions of the GJ 758 dataset. The blue, green, yellow, and red lines display contrast curves for the 30-frame, 35-frame, 40-frame, and full 45-frame reduction, respectively. The dependence of sensitivity on field rotation is clearly reflected in the relative sensitivities of the contrast curves for separations $\gtrsim$0.4".

all of the contrast curves on the same plot. Accordingly, Figure 7.15 displays the contrast curves for all of the reductions of the GJ 758 dataset. The contrast curves for the 25-frame, 30-frame, 35-frame, and 40-frame groups are overlaid by a thick red line indicating the contrast ratio for the full reduction of all 45 GJ 758 frames. As expected, the full reduction has the smallest inner working angle ($\sim$0.1") of all of the reductions and achieves the highest contrast ratio at nearly all separations. Interestingly, the 35-frame reductions appear to reach slightly higher contrast ratios that the full reduction for separations near $\sim$0.25", but the full reduction still reaches a higher contrast ratio than the majority of the other reductions at that separation.

For the entire range of separations plotted in Figure 7.15, there is a clear trend toward higher contrast ratios as the number of frames increases. This trend is most apparent for separations beyond $\sim$0.7", where there is a pronounced layered color progression in the contrast curve from the red line of the contrast curve for the full reduction at the highest contrasts to the purple lines representing the contrast curve for the 25-frame reductions at the lowest contrasts. The trend is also present at separations inside $\sim$0.7", but the contrast curves from the different classes cross more frequently at smaller separations. Looking close to the star at separations near $\sim$0.2", we see that the 25-frame reductions with the highest contrast ($\sim 3\times10^{-4}$) are approximately as sensitive as the 35-frame reductions but less sensitive than the 40-frame and 45-frame reductions, which have contrast ratios of $\sim 2\times10^{-4}$ at $\sim$0.2". We also see that the majority of the 25-frame reductions have contrasts near 5×10^{-4} at separations of 0.2", which is less than half the sensitivity of the full 45-frame reduction. Consequently, although the best 25-frame reductions have contrasts approaching that of the full reduction, acquiring a larger number of frames ($\gtrsim$40) is advisible for targets like GJ 758 in order to maximize the sensitivity of the observation to companions at close separations.

7.4.4 Reduction of HD 69830

In a sense, the HD 69830 dataset serves as the "control group" for the rotation study because all ten rotation groups in the 90-frame class have nearly identical amounts of field rotation (22.74°–23.41°) and the fifty rotation groups in the 50-frame class differ by less than 2° of field rotation. The HD 69830 dataset therefore provides an excellent testbed with which to determine the effects of changes in airmass and AO performance on image quality in the absence of significant variations in the amount of field rotation. While a similar study could be performed by comparing the observations of two different targets using the full set of frames acquired for each target, the advantage of using the subdivided HD 69830 dataset is that the apparent magnitude and declination of the target are constant and therefore do not influence the resulting sensitivity. Furthermore, all of the frames in the HD 69830 dataset were corrected using the same set of flats and darks, which eliminates another degree of freedom compared to a similar study conducted using datasets acquired on two different nights. Given the number of controlled factors, the rotation study of HD 69830 might provide a way to refine the error bars on the contrast curves produced from SEEDS data. As discussed in Section 3.2, observing in ADI mode should theoretically lead to a near-Gaussian noise distribution in the final image (Marois et al. 2008a), but understanding the significance of direct imaging contrast curves is still a relatively new field and much remains to be learned about speckle statistics and confidence limits in the high-contrast regime.

Cognizant of the fact that the HD 69830 dataset may provide information about the influence of other factors on sensitivity, we will now examine the 50-frame reductions of the HD 69830 dataset. The color-coded contrast curves for each reduction are displayed in the top panel of Figure 7.16, and the relative sensitivity of each reduction is plotted in the lower panel. Even though the subgroups have nearly identical amounts of field rotation, we follow the convention established in Section 7.4.1 that

relative sensitivities are determined by dividing the contrast ratio for each reduction by the contrast ratio of the reduction with the largest field rotation. For the 50-frame class of the HD 69830 dataset, the subgroup with the most field rotation is rot 8 (13.69°), which has only 1.57° more field rotation than the subgroup with the lowest amount of field rotation.

Likely due to the similar amounts of field rotation in each class, the contrast curves in the upper panel of Figure 7.16 display less variation than the contrast curves shown for the other targets. Despite the tiny size of the difference in the amount of field rotation between the groups with the largest and smallest values, the lower panel of Figure 7.16 indicates that the achieved contrast does appear to depend slightly on the exact amount of field rotation for separations between ∼0.2" and ∼0.4". Specifically, the groups with $\lesssim$12.3° of field rotation are ∼2 times less sensitive than the groups with $\gtrsim$13.3° at separations of ∼0.2–0.35" For separations beyond ∼0.35", all of the rotation curves have similar contrast curves with relative sensitivities of 1±0.5.

As shown in Figure 7.17, the scatter in the contrasts of the 90-frame reductions of the HD 69830 dataset is even smaller than the scatter in the 50-frame reductions. Like Figure 7.16, Figure 7.17 displays contrast ratios in the top panel and relative sensitivities in the bottom panel. For the 90-frame reduction class, the reference subgroup used to determine the relative sensitivities is rot 0, which has 23.41° of field rotation compared to 22.74° for the subgroup with the smallest amount of field rotation (rot 9).

Ignoring the large spikes in the relative sensitivity for separations <0.2" where the contrast curves are not very meaningful, we see that the contrast ratios for all ten of the 90-frame reductions overlap almost entirely for separations >0.4". Between 0.2" and 0.4", rot 4 appears to be more sensitive than the rest of the subgroups, but the contrast curves for the other subgroups are nearly as similar as they are for larger separations. The enhanced sensitivity of rot 4 might be due to particularly good AO

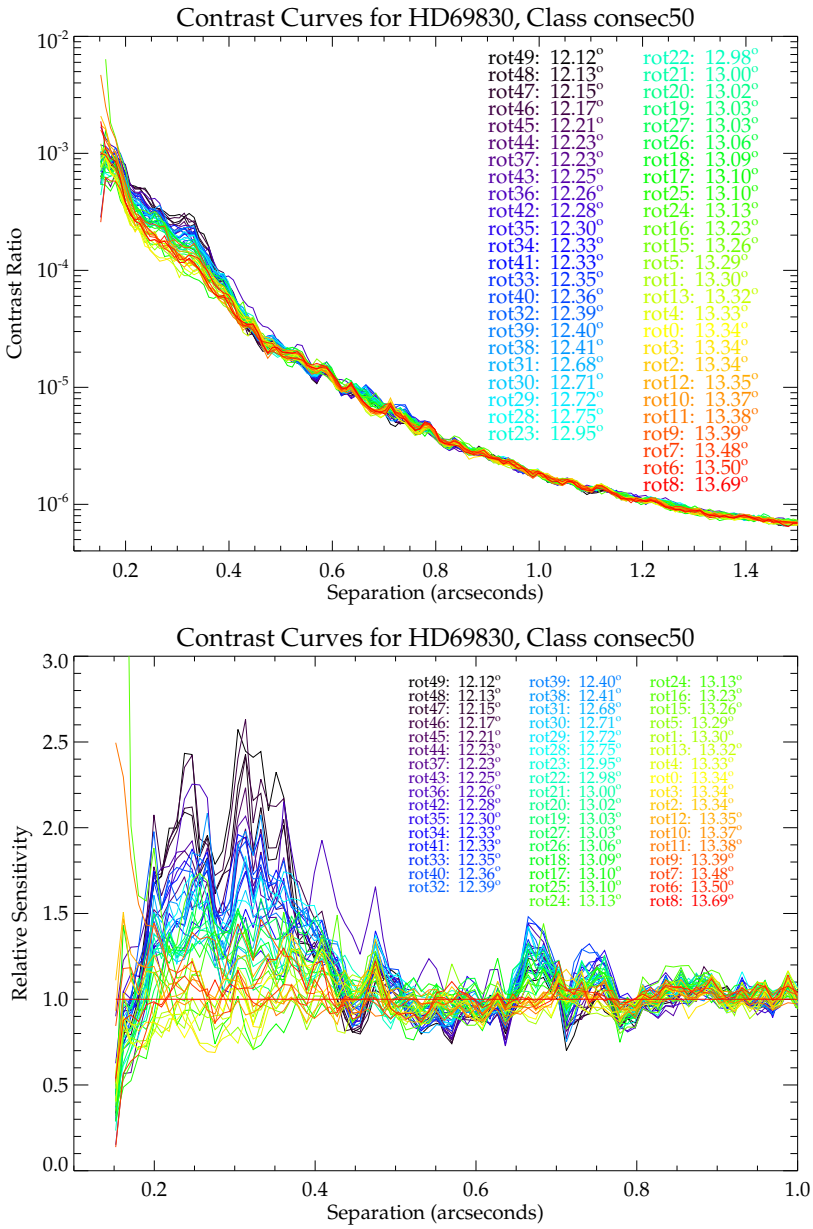

Figure 7.16: Contrast curves for 50-frame reductions of HD 69830. **Top:** Contrast ratios as a function of separation. The subgroups with the largest amount of field rotation acheive slightly better contrasts at separations between 0.2" and 0.3". **Bottom:** Relative sensitivities as a function of separation. For separations $\gtrsim$0.4", the contrast ratios agree to within a factor of 1.5.

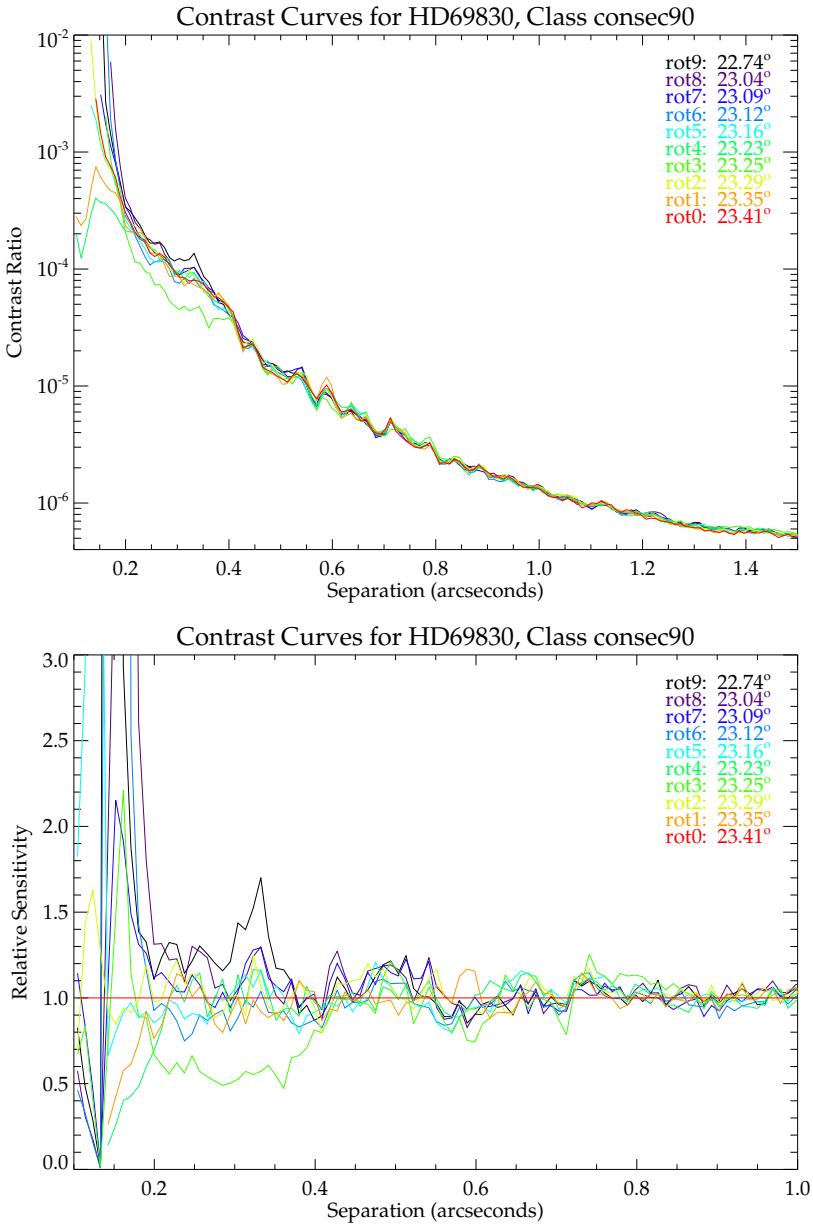

Figure 7.17: Contrast curves for 90-frame reductions of HD 69830. **Top:** Contrast ratios as a function of separation. One of the subgroups achieves a slightly higher contrast ratio for separations between 0.2" and 0.4", but the other subgroups have similar contrast ratios at all separations. **Bottom:**Relative sensitivities as a function of separation. For separations $\gtrsim$0.4", all of the contrast ratios agree to within a factor of 3.

performance or to many other possible factors.

In all, the contrast curves for the 50-frame and 90-frame reductions of HD 69830 are remarkably self-similar. Most likely, this is largely due to the fact that the majority of the frames are identical from one subgroup to the next, but the consistency of the contrast curves also demonstrates the reliability of the ADI pipeline. If the HD 69830 contrast curves had differed significantly from one another despite having nearly identical amounts of field rotation, then that would have been indicative of either rapid PSF evolution or problems with the ADI pipeline.

Chapter 8

Conclusions and Future Work

The first Chapter of this thesis was devoted to a review of exoplanet detection techniques and demographics. Chapter 2 then introduced the leading models of giant planet formation and addressed the difficulty of forming giant planets at extremely wide separations. After considering planet formation, Chapter 2 discussed planetary evolution and contrasted the "hot start" planets modeled by Burrows et al. (2001) with the core accretion planets modeled by Fortney et al. (2008a).

In Chapter 3, we presented an introduction to high contrast imaging. The chapter began with a short history of adaptive optics and then covered advanced techniques for detecting planets at small separations from bright stars. Once the general principles of direct imaging had been explained, Chapter 4 described the history, design, and target categories for the SEEDS project. The instrumentation and observation modes for the SEEDS project were reviewed in Chapter 5, and Chapter 6 provided an overview of the SEEDS data reduction pipeline. Finally, Chapter 7 explored the influence of field rotation on the sensitivity of observations acquired in ADI mode.

As explained in Chapter 7, decreasing the amount of field rotation increases the minimum separation at which planets can be detected and reduces the overall sensitivity of the observation. For moderate reductions in field rotation (e.g., decreasing

from 45° to 40°), the constrast curve may not change significantly for separations $\gtrsim$0.2", but halving the rotation rate could reduce the observation sensitivity by factors of $\sim$2–4 out to separations as large as 0.5". Accordingly, while small decreases in field rotation might be acceptable for nearby targets, more distant targets should be observed at the maximum possible rotation rate in order to maximize the sensitivity to companions at Jupiter-like ($\sim$5 AU) separations.

Furthermore, comparing the sensitivities of the different reduction classes used for the rotation study confirmed that the increasing the number of frames in an observation enhances the sensitivity of the observation. The next step is therefore to compare the sensitivity of observations with a large number of frames acquired at low rotation rates to the sensitivity of observations containing a small number of frames acquired a high rotation rates. This study determined that both increasing the amount of field rotation and increasing the number of frames can improve the sensitivity of an observation, but the number of additional frames that would be required to compensate for a given reduction in field rotation is still unknown.

A future study could adapt the methods and routines used in this study to explore that question by reducing subsets of an existing dataset with varying numbers of frames and amounts of field rotation. If several different combinations of field rotations and integration times yield similar contrast curves, then observers would be able to use that relationship between field rotation and integration time to compensate for the decreased sensitivity of ADI observations taken before or after transit by integrating for a longer period of time. However, if the study demonstrates that longer integration times cannot produce the same sensitivities as higher amounts of field rotation, then observers would have to think carefully about target selection and scheduling in order to maximize the sensitivity of each observation while still examining as many targets as possible.

The preliminary investigations in this thesis suggest that the enhanced sensitivity

of observations acquired during transit and the ability to search for companions at closer separations from the host star provide sufficient motivation to conduct all ADI observations at the maximum possible rotation rate in order to achieve the highest sensitivity to planets and disks. Particularly if the core accretion planet models of Fortney et al. (2008a) accurately predict the luminosities of young jovian planets, ADI observations conducted at less than optimal field rotations will likely not have the sensitivity required to detect exoplanets at the separations seen in our solar system. By conducting ADI observations during transit and acquiring a significant number of frames per target, the SEEDS project will both increase the likelihood of detecting planets and improve the scientific value of null detections because a greater range of angular separations and planetary masses could be exclued in the absence of a detection at a higher contrast ratio.

The results of the SEEDS project will therefore have implications for models of planetary formation and evolution by presenting a updated view of the census of exoplanets at separations $\gtrsim$5 AU around a wide variety of stars. The data acquired from the SEEDS debris disks targets will further inform planet modelers by capturing systems in various stages of planet formation and possibly even imaging planets and disks in the same system. Even for non-astronomers, the prospect of finding solar systems like our own is exciting, and the general public is more accustomed to seeing images than light curves. Accordingly, the results of the SEEDS project and other direct detection surveys have the power to inspire a whole new generation of scientists by allowing them a glimpse of another world.

Appendix A

Data Reduction Pipeline Manual

This manual provides an introduction to the SEEDS ADI pipeline as of April, 2010. Although the pipeline is still being improved, the general structure of the pipeline is fairly stable, and this manual should prove useful even as small changes are made to the pipeline. However, the user is advised to consult the most recent version of the pipeline to ensure that the keywords and input parameters used in this manual are still in use. The most recent version of the pipeline can be obtained from the Princeton svn repository, and all of the pipeline IDL routines can be found in the "hiciao," "utils," and "other" directories within the main "adi" folder. While not every pipeline routine is covered in this manual, effort has been made to include the most important functions and procedures. The manual is organized alphabetically by routine name, and functional dependencies are indicated at the beginning of each section. If no routines are listed, then the routine relies only on standard IDL and Goddard library routines.

A.1 calc_contrast.pro

This routine was written by Dr. David Lafreniére and commented by Dr. Miwa Goto. The program calls several ancillary routines to determine the contrast achieved at

a range of radial separations from the target star. Since an unsaturated image is required to produce the contrast curve, *calc_contrast.pro* cannot be used for observations that contain only saturated frames. One possible alternatives for those datasets is to compute the contrast using *star_constrast.pro* (see Section A.14).

Called by:

pipeline.pro rotpipe.pro

Calls:

prim_level.pro profrad.pro setupdir.pro sumaper_im.pro

Input Parameters and Keywords for *calc_contrast.pro*

pfname: The name of the ".info" file associated with the desired target.

verb: If set, then display images when running *sumaper_im.pro*.

Outline of *calc_contrast.pro*

1. Determine reduction subdirectory.

2. Set coronagraphic transmission, confidence level, and pixel scale. The default settings are trasmission=1 (no coronagraph used), confidence level=5σ, and pixel scale = 0.010 arcseconds per pixel. If the user wishes to compute the contrast curve at a different confidence level or for an observation taken using a coronagraph the relevent parameters must be changed in lines 16-18.

3. Read in the "final.fits" file produced by *subadi.pro*.

4. Convolve the sampling aperature over each pixel in the image and construct a radial profile for the image.

5. Determine the flux at each radius.

6. Plot the contrast curve showing the magnitude of the faintest companion that could be detected at each radius.

7. Write the IDL save file "contrast.dat" containing the following data:

   (a) **im1:** The convolved image.

   (b) **prim:** Target star flux.

   (c) **sig:** The one-dimensional radial profile.

   (d) **rsig:** The array of radii (in pixels) corresponding to the 1D profile.

   (e) **a:** The array of radii (in arcseconds) corresponding to the 1D profile.

   (f) **raw_mag:** The magnitude of the target star flux at each radius.

   (g) **lipsub:** The magnitude of the flux recovered from a companion at each radius.

   (h) **cmag:** The faintest magnitude at each radius at which a companion could be detected at the desired confidence level.

   (i) **imnoise:** The two-dimensional radial profile, which is a good measure of the amount of noise in the image.

A.2 destripe_alt3.pro

Called by:

pipeline.pro

Calls:

setupdir.pro tt_map.pro

Input Parameters and Keywords for *destripe_alt3.pro*

horizontal_only: If set, then only remove vertical stripes and ignore any horizontal stripes in the data. The default setting is to remove both horizontal and vertical stripes.

fourier: If set, apply a fast fourier transform to better identify and remove vertical stripes. The setting of the "fourier" keyword does not affect the horizontal stripe removal process.

Outline of *destripe_alt3.pro*

1. Run *setupdir.pro* to determine the data, reduction, and calibration directories.

2. Read in the list of saturated frames corresponding to the requested target. The name of the file read is given as "[target]_sat.txt" without the full path, so *destripe_alt3.pro* must be called from the reduction directory.

3. Set defaults for the expected stripe geometry based on a previous study of the detector properties. *Destripe_alt3.pro* expects 32 horizontal stripes of height 64 pixels and width 2048 pixels.

4. Divide the detector into even and odd stripes.

5. Begin looping over the saturated frames listed in the "_sat.txt" file and read in the first frame.

6. Remove bad pixels using the definition that a bad pixel has a value that differs from the mean pixel intensity by at least 10σ. Replace the bad pixels with not a number (NaN) flags.

7. Loop over the number of stripes to remove horizontal stripes.

(a) Force the median value of each stripe to be the same by adding the difference between adjacent stripes to the value of one of the stripes.

(b) Subtract the median value of the frame from all pixels.

8. Remove vertical stripes.

   (a) If "fourier" keyword is set, then perform a fast fourier transform of the image and search for peaks in fourier space. Set the value of any peaks to zero and transform back into real space. Once in normal space, flag the pixels corresponding to the peaks as Not a Number (NaN).

   (b) If "fourier" keyword is not set, then construct a template pattern based on the median value of each column and subtract the pattern from the even stripes. Repeat the procedure for the odd stripes using a second template.

9. Write the destriped frame to a FITS file with the same basename as the input file but with the extension "_ds.fits" instead of ".fits."

A.3 destripe_directory.pro

Calls:

setupdir.pro ql_get_namenext.pro tt_map.pro

Input Parameters and Keywords for *destripe_directory.pro*

path: This required parameter indicates the location of the files to be destriped.

horizontal_only: If set, then only remove horizontal stripes. If not set, then remove both horizontal and vertical stripes.

fourier: If set, then use a Fast Fourier Transform when removing vertical stripes.

filestart: If set, then start destriping at the indicated file. If "filestart" is not set, then destriping will begin at the first file in "path."

Outline of *destripe_directory.pro*

1. Run *setupdir.pro* to establish the data, calibration, and reduction directories.
2. Set default parameters.
3. If "filestart" is set, then find the starting file. Otherwise, start at the first file in the folder.
4. Find the filenames for all files in the given path.
5. Check which files have already been destriped.
6. Destripe the non-destriped files using the procedure described in Section A.2 for *destripe_alt3.pro*.
7. Beep to alert the user when destriping is finished.

A.4 filtseq.pro

Input Parameters and Keywords for *filtseq.pro*

pfname: Input parameter specifying the name of the ".info" file associated with the target (e.g., "TYC135.info").

rmin: Minimum radius used by *profrad.pro* to determine the radial profile. If not set, *profrad.pro* automatically sets "rmin" to 0. Since "rmin" is used only by *profrad.pro* and not by *tt_radialize.pro*, the value of "rmin" does not matter if "TT" is set. Even though setting "rmin" is optional, "rmin" is coded as a variable, not a keyword.

rmax:: Maximum radius used by *profrad.pro* to determine the radial profile. The default value is to use the entire width of the image. Since "rmax" is used only by *profrad.pro* and not by *tt_radialize.pro*, the value of "rmax" does not matter if "TT" is set. Even though setting "rmax" is optional, "rmax" is coded as a variable, not a keyword.

fc: If set, then *filtseq.pro* looks for input files with the extension "_r_fc.fits" and writes output files with the extension "_f_fc.fits."If not set, the default extension for input and output files are "_r.fits" and "_f.fits," respectively.

IorP: String specifying whether a PDI image is an intensity image ("IorP=I") or a polarization image ("IorP=P"). For non-PDI images this keyword is not necessary and will automatically be set to a blank string ("").

HWP: Keyword specifying the position of the half wave plate for PDI frames. For non-PDI observations "HWP" should not be set.

TT: If set, the radial profile will be determined using *tt_radialize.pro* instead of the default *profrad.pro*.

Outline of *filtseq.pro*

1. Run *setupdir.pro* to identify the reduction directory.

2. Determine the reduction subdirectory from the input parameter "pfname," which is the name of the ".info" file associated with the desired target.

3. Read in the list of file basenames from the [fileroot]+"_sat.txt" file if "HWP" is not set or the [fileroot]+"_"+[HWP]+".txt" file if "HWP" is set. (A file basename is simply the root of the filename without the extension.)

4. Add the relevent file extensions to determine the names of the input produced by *reduc_sat_alt.pro* and the output files that will be used by *subadi.pro*.

5. Process each image.

   (a) Read in each image one by one.

   (b) Determine the radial profile of the image using *tt_radialize* if "TT" is set or *profrad* if "TT" is not set.

   (c) Subtract the profile from the image.

   (d) Save the image using the extension "_f.fits" if "fc" is not set or "_f_fc.fits" if "fc" is set.

A.5 make_redgrps.pro

This routine was written by Courtney Dressing to copy files and create directories for the field rotation study described in Chapter 7.

Calls:

setupdir.pro slash.pro

Input Parameters and Keywords for *make_redgrps.pro*

loc: The location of the data frames to be copied by *make_redgrps.pro*. The default value is loc="/scr1/courtney/data/raw/[target]", where "target" is the name of the target to be reduced.

nframes: The desired number of frames per reduction sequence. The default value is 25 frames.

ds: If set, then look for destriped files with the extension "_ds.fits" instead of the default ".fits" extension.

homedir: If set, then the user can specify where to put the subdirectories for each rotation group. If not set, then "homedir" will be set by calling *setupdir.pro*.

dirbase: The name of the parent directory containing all of the rotation subgroups. The default directory name is dirbase="[target]_consec[nframes]/."

nowrite: If set, then make reduction directories for each subgroup, but do not copy files into separate data directories. Setting "nowrite" is useful if the user forgot to set "targdatabase" the first time *make_redgrps.pro* was called.

target: The name of the target to be reduced. The default target is HD23912.

phot: If set, then look for the folder "/scr1/courtney/data/raw/[target]_phot" and copy photometric files from that folder into all rotation data subdirectories.

targdatabase: If set, then copy the target database into all rotation reduction subdirectories. The user may change the location of the targetdatabase by changing the path of the "database" string given in line 34 of *make_redgrps.pro*.

spacing: If set, then only create rotation groups for every "spacing" files, i.e., if spacing=3, then only create rotation groups for every third file. Setting "spacing" allows the user to conduct a rotation study for a large dataset without creating hundreds of rotation groups.

Outline of *make_redgrps.pro*

1. Check keywords and set defaults.

2. Identify the ".fits" or "_ds.fits" files in the directory given by "loc" and store the filenames in the list "flist."

3. If "phot" is set, then create a list of the ".fits" files in the photometric directory corresponding to the desired target.

4. Extract the parts of the filenames that contain numbers and create the array "fnums" containing the numeric parts of each file listed in "flist."

5. Check that the number of files requested in each subgroup is smaller than the total number of files.

6. Create data directories for each subgroup and copy the appropriate files into each folder. If "phot" is set, then the photometry frames will be copied into all of the reduction directories.

7. Create reduction directories for each subgroup.

8. If "phot" is set, copy the file "get_cind.fits" into each reduction directory. The user should indicate the location of "get_cind.fits" by setting "getcindloc" in line 38 of *make_redgrps.pro*.

9. If "targdatabase" is set, then copy the target database into each reduction directory. The location of the target database is set by "database," which the user can change on line 34 of *make_redgrps.pro*.

10. Write a customized *setupdir.pro* to each folder.

A.6 mkobslog.pro

This simple routine was written by Dr. David Lafreniére and later modified by Dr. Markus Janson. The program creates a list of all of the FITS files in the data directory indicated in *setupdir.pro*.

Called by:

pipeline.pro

Calls:

setupdir.pro

Input Parameters and Keywords for *mkobslog.pro*

mkobslog.pro does not allow any keywords or input parameters.

Outline of *mkobslog.pro*

1. Call *setupdir.pro* to identify the data directory in which the files are stored and to determine the desired filename for the log.

2. Call the Goddard Library IDL routine *fitsdir.pro* to create a list of all of the ".fits" files in the data directory. The logfile is written to the directory from which the user called IDL and contains the following information in each column:

   (a) **Object:** The name of the observation target.

   (b) **Data Type:** This indicates whether the observation is for engineering or science. In most cases, the data type keyword will be set to "OBJECT."

   (c) **Observation Mode:** This indicates whether the observation was acquired during engineering observations or during scientific observations in direct imaging (DI), polarimetric differential imaging (PDI), or spectral differential imaging (SDI) mode. The possible values for the observation mode keyword are "TOOL," "SUBROUTINE," "DI," "PDI," and "SDI." The value "TOOL" is used for frames during the photometric sequence before and after scientific observations. The value "SUBROUTINE" indicates that a frame was acquired as the proper integration time was being determined or during target acquistion or pupil alignment. Frames marked with the Observation Mode value of "SUBROUTINE" are not as high-quality

as the scientific frames indicated by "DI,", "PDI,", or "SDI," and should therefore not be used for science unless they are carefully examined.

(d) **Filter 1:** The identity of the filter in position one. The first filter wheel currently holds the broadband filters in Y, J, H, and K, so the value of this keyword will likely be "H" or "K" because those filters are used most frequently by the SEEDS team.

(e) **Filter 2:** The identity of the filter in position two. The second filter wheel contains the pupil viewer, neutral density filters, and an open position without a filter. The value of this keyword will be "PV" for frames acquired in pupil-viewer mode during pupil alignment, "open" for frames acquired without a filter in position two, and "ND[number]" for frames acquired using a neutral density filter. All of the neutral density filters are labeled so that the number following the letters "ND" indicates the strength of the filter. For example, the keyword "ND10" indicates that the neutral density filter blocked all but 10% of the light while the keyword "ND1" indicates that only 1% of the light was transmitted by the filter.

(f) **Filter 3:** The identity of the filter in position three. This keyword will be "OPEN" for DI or PDI observations, "CH4R70" indicating the presence of a methane filter for SDI observations, or "DARK" for dark frames.

(g) **Exposure Time:** The length of the exposure in seconds.

(h) **Co-add:** Indicates the number of co-adds used in the observation. For most observations taken after October 2009, this number will be 1, indicating that no co-adds were used.

(i) **Date:** The date of the observation in UTC time. In the case of disagreements between the date given in the paper log and in the log produced by *mkobslog* using the FITS header keywords, the date in the computer-

produced log is likely correct because the paper log may occasionally provide dates in Hawaii local standard time instead of UTC.

(j) **P_RTAG:** The position of the polarization rotator (i.e., half wave plate). This value will always be 0 for DI and SDI observations, but may be 0, 22.5, 45, or 67.5 for PDI observations depending on the polarization observed in that frame.

A.7 newobs.pro

Called by:

pipeline.pro

Calls:

param.pro queryvizier2.pro[1] *setupdir.pro*

Lists of Frames Produced by /emphnewobs.pro

_sat.txt: These frames are considered saturated and have the maximum exposure time in the observation sequence.

_nsat.txt: These frames are considered unsaturated and have the minimum exposure time in the observation sequence.

_pQ.txt: These frames were taken with the half wave plate angle at 0° and are polarized in the $+Q$ direction. Only applicable to observations taken in PDI mode.

[1] *queryvizier2.pro* is a slightly modified version of the Goddard Library IDL routine *queryvizier.pro*.

_mQ.txt: These frames were taken with the half wave plate angle at 45° and are polarized in the $-Q$ direction. Only applicable to observations taken in PDI mode.

_mU.txt: These frames were taken with the half wave plate angle at 22.5° and are polarized in the $-U$ direction. Only applicable to observations taken in PDI mode.

_pU.txt: These frames were taken with the half wave plate angle at 67.5° and are polarized in the $+U$ direction. Only applicable to observations taken in PDI mode.

Outline of *newobs.pro*

1. Asks user to input the date, object name, and filter for the observation. Also prompts user to enter a suffix for the .info file produced by *newobs.pro*. Most users will not need to customize the .info file suffix and can simply press enter without entering text in order to use the default ".info" suffix.

2. If the user has supplied a targetdatabase, read in the information (RA, dec, v-band magnitude, h-band magnitude, and proper motion) corresponding to the specified target. Alternatively, if the user has not specified a target database, attempt to retrieve target information from the Simbad or Vizier databases. *newobs.pro* will return an informative error message at this point if it cannot locate the required target information.

3. Use the *param.pro* routine to create the structure s containing the target information read in from the user-supplied or online target database.

4. In the case where parallax and error on parallax were not found (e.g., objects that were not imaged by Hipparcos), set parallax and error on parallax equal

to zero. *newobs.pro* writes a warning in the terminal that parallax was not found, but this warning is easy to overlook and could be replaced by a popup widget-style warning if the user wanted to be more aware of cases for which parallax was unknown.

5. Access the log file created by *mkobslog.pro* and identified in *setupdir.pro* to obtain a list of the frames in the data directory (also specified by *setupdir.pro* that observe the requested target on the correct date with the identified filter.

6. Examine the list of frames and remove all frames that are not science observations.

7. Some of the files in the directory may have a "_ds.fits" suffix indicating that they have been destriped while other files will have the default ".fits" suffix because they have not yet been destriped. Remove the suffixes from the list of filenames and eliminate duplicates from the list. The current version of *newobs.pro* works equally well when the data directory contains only destriped files, only non-destriped files, or a mix of both; this step merely ensures that each frame will only be listed once in the output ".txt" files produced by *newobs.pro*.

8. Inspect the exposure time used for each frame and determine the maximum and minimum exposure time for the observation sequence.

9. Write the names of the files with the maximum exposure time to a list of saturated frames. The list is saved in the reduction directory and is called "[object name]+[optional .info suffix]+_sat.txt."

10. Write the names of the files with the minimum exposure time to a list of unsaturated frames. The list is saved in the reduction directory and is called "[object name]+[optional .info suffix]+_nsat.txt."

11. If the user has set the "polarimetry" keyword, also produce the output files "[object name]+[optional .info suffix]+_[yX].txt," where yX is the polarization pU, mU, pU, or pQ as explained previously in this section.

12. Set the default parameters for later steps in the reduction process. For example, set the required field rotation for each radius during the locally optimized combination of images (LOCI) to 0.75 times the point spread function.

A.8 partial_sub.pro

This procedure places fake companions into the dataset and determines the fraction of flux recovered from each companion. The routine was written by David Lafreniére and subsequently modified by Markus Janson.

Called by:

pipeline.pro rotpipe.pro

Calls:

filtseq.pro intshift.pro param.pro parangle.pro myaper.pro normbyghost.pro rotat.pro setupdir.pro statsvsr.pro subadi.pro subarr.pro translate.pro

Input Parameters and Keywords for *partial_sub.pro*

pfname: The name of the ".info" file associated with the desired target.

ntc: Number of angles at which to insert fake companions. The default value is 15, but *partial_sub.pro* takes a long time to run using 15 angles and is usually run with only 3 angles.

test: If set, the program will stop at the end of the loop so that the user can watch each step of the process.

rmax: The maximum radius at which a fake companion will be inserted. The default value is 715 pixels.

nghost: If set, then normalize by ghost using *normbyghost.pro*.

oldpa: If all of the frames are derotated to the position angle allpa[0], then this keyword must be set. For the current Princeton version of the pipeline, "oldpa" should not be set because the images are not derotated.

imgrot: If set, then derotate the frames using the rotation angles "imr" listed in the FITS file header. The user does not need to worry about setting "imgrot" because the keyword will be set automatically if rotation angles are listed in the FITS file header.

IorP: String specifying whether a PDI image is an intensity image ("IorP=I") or a polarization image ("IorP=P"). For non-PDI images this keyword is not necessary and will automatically be set to a blank string ("").

HWP: Keyword specifying the position of the half wave plate for PDI frames. For non-PDI observations "HWP" should not be set.

tag: If set, use alternate filelists with the extension "[tag].txt" instead of the default ".txt" extension.

verb: If set, then write output to the screen and display images during the reduction process. Not setting "verb" will speed up the reduction process.

Outline of *partial_sub.pro*

1. Determine filelists based on the values of "tag" and "IorP."

2. Run *setupdir* to identify the reduction directory.

3. Set parameters for the reduction.

4. Read in the filenames from the filelists and set the output filenames.

5. Identify the image size from the header of the first frame.

6. Read the file "reduc.log" produced by *reduc_sat_alt.pro* to find the hour angle and parallactic angle at the initial position of the target.

7. Set the radii and position angles of the fake companions.

8. Find the aperture radius from the FWHM in the ".info" file.

9. Calculate the fluxes of the fake companions.

10. Draw smeared fake companion PSFs on all of the "_r.fits" frames and save them with the extension "_r_fc.fits."

11. Perform ADI treatment on the "_r_fc.fits" files containing the implanted fake companions to produce the output file "final[IorP]_fc.fits."

    (a) Run *filtseq.pro*

    (b) Run *subadi.pro*

12. Read in the "final[IorP]_fc.fits" file produced by the ADI reduction and determine the fraction of companion flux that was preserved.

13. Write the output file "partial_sub[IorP].dat" containing the following information in each column:

    (a) **rc:** The radial positions of each fake companion.

    (b) **eff** The fraction of flux that was recovered from fake companions at each radius.

A.9 photo_contrast.pro

This routine was written by Michael McElwain to produce contrast curves according to the method used by *star_contrast.pro* but using an unsaturated image of the target to determine the PSF instead of an image of a background star.

Called by:

loop_contrast.pro

Calls:

setupdir.pro subarr.pro medim.pro padarr.pro tt_radialize.pro plottops.pro

Input Parameters and Keywords for *photo_contrast.pro*

targ: Name of target to reduce. The default is "TYC135."

group: Name of the rotation class to reduce. The default is "consec50."

rot: Name of the rotation subgroup to reduce. The default is 10.

savename: Name of IDL save file in which to store the separations and contrasts. The default is to save the data in the reduction directory using the filename "[targ]_[group]_[rot].sav."

nexp: The number of exposures in the subgroup. The default is that the number of exposures is given by the number in the name of the rotation class.

Outline of *photo_contrast.pro*

1. Set default parameters.

2. Read in the appropriate photometric standard.

3. Calculate the average background per pixel.

4. Read in the science frame (the "final.fits" file).

5. Convolve the image over the narrow aperture.

6. Determine the contrast "fivesig" at each separation "sep."

7. Produce plots of the contrast ratio for the given integration time and for one hour of integration.

A.10 profrad.pro

This procedure is the default routines used by *filtseq.pro* to determine the radial profile of an image. *profrad.pro* was written by **WHO?** and is stored in the "utils" directory.

Called by:

filtseq.pro

Calls:

dmedian.pro

Input Parameters and Keywords for *profrad.pro*

imt: Array containing the frame for which the radial profile should be determined. The array does not need to be square.

res: Optional variable indicating the desired resolution (in pixels) of the radial profile. The default value is 1 pixel.

r1: Optional argument stating the minimum radius for which the radial profile should be computed. The default value is 0. If "r1" is nonzero, then the radial profile will be extrapolated to radii between 0 and "r1" using a cubic spline.

r2: Optional argument stating the maximum radius for which the radial profile should be computed. If "r2" is not set, then the radial profile will be computed out to the edge of the image. If "r2" is set, then the computed profile will be extrapolated to radii beyond "r2" using a cubic spline.

med4q: If set, then take the median over the four quadrants of the image when computing the 2-dimensional radial profile. Setting "med4q" only matters if "p2d" is set, because the value of "med4q" does not influence how the 1-dimensional radial profile is computed.

p2d: If set, then compute a 2-dimensional radial profile.

p1d: If set, then compute a 1-dimensional radial profile.

rayon: An array containing the radii corresponding to each value in the radial profile.

Outline of *profrad.pro*

1. Determine the size of the image and set default parameters.

2. Create a distance array "rayon" containing the distance of all points from the center of the frame. If "r1" or "r2" are set then the distance array will only contain the distances greater than "r1" and less than "r2."

3. Compute the 1-dimensional radial profile by finding the median value of all pixels a given distance from the center of the frame (i.e. each value in "rayon").

4. If "p2d" is set, compute the 2-dimensional profile.

5. If “med4q” is set, take the median of the four quadrants.

6. If “verb” is set, print the minimum and maximum values of “rayon” to the screen.

A.11 reduc_sat_alt.pro

Input Parameters and Keywords for *reduc_sat_alt.pro*

binary: The user should set this keyword when reducing binary star data. If set, the user will be prompted for the separation in pixels from the target star to the closest companion and the approximate pixel location of the target star. The pipeline should work aproximately normally for sufficiently wide separations, but if the companion is within 100 pixels of the target star, *reduc_sat_alt.pro* warns the user that the pipeline may yield inaccurate results.

remove_stripes: If set, then *reduc_sat_alt.pro* will call *destripe_frame.pro* to destripe each frame.

manual_center:: If set, then the reference image will be shifted so that the given cordinates (x=manual_center[0], y=manual_center[1]) lie at the center of the registered frame. All other frames will then be aligned to this center. The image used as the reference frame is the middle frame of the observation sequence and the filename can be determined by checking the “Information about image used for centering” output that is printed to the terminal when *reduc_sat_alt.pro* is called.

correlation_window: The correlation window radius. Rather than align whole frames, *reduc_sat_alt.pro* compares only the central region of each frame to reduce the odds that frames will be misaligned by a large number of pixels. The

default radius of the correlation window is 100 pixels and the window is centered on each frame.

no_fine_centering: If set, then do not perform fine centering adjustments.

destriped: The user should set this keyword if the frames have already been destriped. If "destriped" is set, *reduc_sat_alt.pro* will look for files with the extension "_ds.fits" instead of the default ".fits" extension.

register:: The name of this keyword implies that the frames will not be registered if the keyword is not set, but this keyword simply determines the type of registration algorithm. If set, then *reduc_sat_alt.pro* will register the frames using the algorithm *register_coro_image.pro* instead of the default *getshift.pro* algorithm. The keywords "inner," "outer," "search," "show," "fit," and "verb" are all passed directly to *register_coro_image.pro*, so there is no point in setting those keywords when "register" is not set. The subtle differences between the two registration procedures are explained below. The performance of each registration routine seems to vary slightly based on the particular data set, so users may wish to experiment with both registration algorithms and compare the resulting reductions.

- **register_coro_image.pro:** This routine was written by Christian Thalmann to determine the offset between an image frame "img" and a reference frame "ref." The program calculates and returns the x- and y-offset of the image from the reference frame and computes the chi-squared value for the fit.

  The keywords are

  - **inner:** The inner radius (in pixels) of the annulus within which *register_coro_image.pro* computes the chi-squared value of the fit. The default value is 40 pixels.

- **outer:** The outer radius (in pixels) of the annulus within which *register_coro_image.pro* computes the chi-squared value of the fit. The default value is 150 pixels.
- **search:** Half of the sidelength of the search box within which *register_coro_image.pro* searches for the center of the image. The default half-length is 5 pixels.
- **show:** If set, then show the alignment process when *register_coro_image.pro* is called.
- **fit:** If set, then fit a Gaussian during *register_coro_image.pro*.
- **verbose:** If set, then print information to the screen.

Outline of *reduc_sat_alt.pro*

1. Set defaults.
2. Determine which star is the target if a binary system was observed.
3. Create a list of filenames.
4. Confirm that all files exist.
5. Check that all of the frames have the same values for the object observed, the exposure time, and the filters used. At the moment, the checks on right ascension and declination are ignored because the coordinates in the FITS headers are not identical for all of the frames.
6. Load the flat file.
7. Load the dark file.
8. Identify deviant pixels.
9. Load information about the target from the ".info" file.'

10. Determine which image to use for centering.

11. Dark subtract.

12. Flat field.

13. Correct bad pixels.

14. Correct distortion.

15. Find the approximate center of the frame.

16. Align all of the images.

17. Write the registered "_r.fits" files.

18. Write the reduction log "reduc.log" containing the filenames, x and y coordinates of the frame centers, the saturation radius, the hour angle, and the parallactic angle for each frame.

19. Write the initial and final parallactic angles for each frame in the file "pa.dat"

20. Beep to alert the user than *reduc_sat_alt.pro* is complete.

A.12 see_fits.pro

This routine was written by Courtney Dressing to assist the user in examining frames at various stages in the reduction process. The program displays each frame as a color IDL image and allows the user to classify the image as good or bad. Once the program is finished, the filenames of the good and bad frames are written to the files "good_frames.txt" and "bad_frames.txt," respectively.

Input Parameters and Keywords for *see_fits.pro*

ct: Number of the color table used to display image. The default color table is 13 (rainbow).

dir: The full path of the directory containing the frames to inspect. Either "dir" or "filelist" must be specified.

ds: If set, then only display destriped images with the file extension "_ds.fits." The "ds" keyword is only relevant when *see_fits.pro* is called with the "dir" keyword.

filelist: The filename of a text file containing the list of images to display. The full filepaths of the images must be included in the text file. Either "dir" or "filelist" must be specified.

scale:: The factor by which the size of the displayed image shoul be reduced. The default setting is to display the full size of the image (i.e., scale=1).

tag: If set, then only display images with the file extension "[TAG].fits." The "tag" keyword is only relevant when *see_fits.pro* is called with the "dir" keyword.

Outline of *see_fits.pro*

1. Set defaults and check that user has supplied either "dir" or "filelist" (but not both).

2. Confirm that at least one file meets the criteria.

3. Display each image and record the key pressed by the user to classify each image. Press "F" for good frames and "J" for bad frames.

4. Write the filenames of the good frames to "good_frames.txt" and the filenames of the bad frames to "bad_frames.txt."

A.13 setupdir.pro

This routine simply informs IDL of the locations of the various directories required for reducing SEEDS data.

Called by:

pipeline.pro

Input Parameters and Keywords for *setupdir.pro*

datadir: This string is the path to the data directory. Like all paths set by *setupdir.pro*, the path may be either relative or absolute, but it must end in a slash.

caldir: This string is the path to the calibration directory. In most cases, the user should be able to use the same calibration directory for all reductions.

reducdir: This string is the path to the reduction directory, which is where the reduced frames and associated output will be written. A subdirectory will be created inside of this directory with the name of the target, so if the user is reducing observations of GJ 758 and wants to direct the output to the path '/scr1/users/USER/REDUCTION/GJ758/', then *reducdir* should be set to '/scr1/users/USER/REDUCTION/' not '/scr1/users/USER/REDUCTION/GJ758/' (because that would cause output to be written to '/scr1/users/USER/REDUCTION/GJ758/GJ758/').

logfile: This string indicates the desired filename (including the extension) of the log file containing the list of frames. The logfile will be written in the main reduction directory, not the subdirectory corresponding to the target being reduced.

hiciaodir: This string indicates the path to the "hicaio" directory, which contains most of the data reduction subroutines. The user should only need to edit this path once because it will remain constant for all future reductions.

homedir: This string is the path to the directory containing the user's desired data and reduction directories. The user will likely use the same *homedir* for most reductions.

Outline of *setupdir.pro*

1. Set the data directory.
2. Set the calibration directory.
3. Set the reduction directory.
4. Set the hiciao directory.
5. Set the name of the log file.

A.14 star_contrast.pro

This routine was written by Michael McElwain and Christian Thalmann to determine the contrast of an observation using the PSF of a background star in the frame.

Called by:

Calls:

Input Parameters and Keywords for *star_contrast.pro*

phot_filename: The filename of the photometric standard. The default is "REDUCTION/GJ758_contrast/HICA90010733_r.fits."

psf_filename: The filename of the PSF standard.

science_filename: The filename of the science frame. The default is "GJ758/final.fits."

partial_sub: The filename of the "partial_sub.dat" file. The default is "GJ758/partial_sub.dat."

group: The name of the reduction subgroup.

savename: The filename to use for the IDL savefile containing the separations, contrasts, and hourfactor. The default is [targ]+[group]+'_contrast.sav'

Outline of *star_contrast.pro*

1. Set defaults.
2. Read in the photometric standard.
3. Remove bad pixels from the photometric standard.
4. Read in the PSF shape reference.
5. Calculate the effective Strehl ratio.
6. Read in the science image.
7. Determine the narrow aperture flux of the primary.
8. Calculate the noise curve.
9. Determine the contrasts at each separation.
10. Produce plots of the contrast curve for the given amount of integration time and for 1 hour of integration.
11. Save the separations, contrasts, and hourfactor in the appropriate IDL save file.

A.15 subadi.pro

Called by:

pipeline.pro rotpipe.pro

Calls:

angarr.pro medfits.pro nbr2txt.pro param.pro rotat.pro setupdir.pro

Input Parameters and Keywords for *subadi.pro*

pfname: The name of the ".info" file associated with the target to be reduced.

nfwhm: The minimum number of full width at half maximum by which an image must be shifted in order for that frame to be used for subtraction during the Locally Optimized Combination of Images (LOCI) sequence. If "nfwm" is not set in the ".info" file, then *subadi.pro* will use 0.75 FWHM as a default value.

drsub: The width of each annulus for LOCI. If "drsub" is a scalar then the same width is used for all annuli, but if "drsub" is an array, then the width of each annulus is determined iteratively and the width of the innermost annulus :

$$dr = \left(0.5\pi + \arctan\left(\frac{\text{rmin} - \text{drsub0[2]}}{\text{drsub0[3]}}\right)\right) \times \frac{1}{\pi} \times (\text{drsub0[1]} - \text{drsub0[0]}) + \text{drsub0[0]}$$

The default value of "drsub" set during *newobs.pro* are 5, 50, 120, and 1.

na: The area of optimization regions during LOCI. The default value set during *newobs.pro* is 300.

geom: The geometry of the optimization region used for LOCI. The default value set by *newobs.pro* is 1.

rmin: The minimum radius for the subtraction annuli. The default value is the saturation radius minus 5 unless the saturation radius is less than five pixels. In that case, the default value is rmin=5.

rmax: The maximum radius for the subtraction radius. The default value is $^{1}.1/_{2}$ times the width of the image.

fc: If set, the save files with the extension "fc.fits" instead of the default ".fits" extension. The "fc" keyword is set when *subadi.pro* is called by *partial_sub.pro* to recover the flux from fake companions.

angoffset: If set, then adjust the angles of the annulus sections by the value of angoffset.

outfile: If set, then save the final median fits image using the filename "outname" instead of the default filename "final[hwpstring][IorP][tag].fits" or "final[hwpstring][IorP][tag]_fc.fits"

nomedsub: If set, then do not subtract the median from the annulus segments.

visualize: If set, then display the subtraction and optimization process for the user.

imgrot: If set, then examine the FITS header to determine the angle by which each image should be rotated.

noderotation:: If set, then do not derotate the frames and save the output files with the extension "_a.fits" instead of the default extension "_s.fits."

tag:: If set, then save the output files with the extension "[tag].fits" instead of the default ".fits" dextension.

IorP: String specifying whether a PDI image is an intensity image ("IorP=I") or a polarization image ("IorP=P"). For non-PDI images this keyword is not necessary and will automatically be set to a blank string ("").

HWP: Keyword specifying the position of the half wave plate for PDI frames. For non-PDI observations "HWP" should not be set.

verb: If set, then operate in "verbose" mode and display text output to the screen during the reduction.

Outline of *subadi.pro*

1. Run *setupdir.pro* to determine the reduction directory.
2. Set filenames using the values of "tag,", "IorP," "HWP," and "fc."
3. Call *param.pro* to find the full width at half maximum, the saturation radius, the number of FWHM required for subtraction, and other LOCI parameters.
4. Load parallactic angles from "reduc.log."
5. Determine the radii of the subtraction annuli.
6. Cut each image into rings 5 pixels wide and save all of the annuli at the same radius in the same temporary file.
7. Process each annulus.
   (a) Determine the optimization region for the annulus.
   (b) Load the required rings from memory.
   (c) Remove NaN and deviant pixels.
   (d) Save the indices for the image in the file "indices_images.dat."
   (e) Construct a matrix to solve the optimization problem.
   (f) Loop through images
      i. Identify which images are sufficiently shifted for subtraction.
      ii. Construct the reference annulus.

iii. Perform subtraction.

iv. Unless "nomedsub" is set, subtract the median from the difference between the reference segment and the annulus being optimized.

v. Save the optimized annulus to a temporary binary file.

8. Erase temporary files

9. Read in indices of subtracted pixels from "indices_images.dat."

10. Reconstruct the images.

11. Unless "noderotation" is set, derotate the images so that they are aligned with the first image.

12. Save the reconstructed and derotated image to a file with the extension "_s.fits" if "fc' 'is not set or the extension "_s_fc.fits" if "fc" is set.

13. Run *medfits.pro* to compute the median image of the reconstructed and derotated images.

14. Save the median image as "final[hwpstring][IorP][tag].fits" if "fc" is not set or "final[hwpstring][IorP][tag]_fc.fits" if "fc" is set.

Appendix B

Creating a Target Database

If the SIMBAD and VizieR databases do not contain the target parameters, then the user must supply a user-created target database file when calling *newobs.pro*. As shown in the sample target database file in Table B.1, the target database file should be a text file containing one line of information for each target. Within each line, the target parameters should be separated by vertical lines "|." The file may include comments as long as the comments are marked by a semicolon as in IDL routines.

Table B.1: Sample Target Database File for use with *newobs.pro*

; Obj Name[a]	RA(hms)	Dec(dms)	RA(deg)	Dec(deg)	SIMBAD ID	Hipparcos?	SpectralType	Vmag	Plx(mas)	Plx error (mas)	PM RA	PM RA err	PM Dec	PM Dec err	2MASS?	Hmag	Hmag err
HIP25486	05:27:04.76	-11:54:03.5	81.7698	-11.9010	V* AF Lep	yes	F7V	6.30000	37.2600	0.840000	17.1900	0.690000	-49.3000	0.640000	yes	5.08700	0.0260000
HIP60661	12:25:58.58	+08:03:44.0	186.494	8.06223	GJ 466	yes	M0	10.3400	25.0800	1.85000	-129.110	2.16000	-110.850	1.48000	yes	13.4450	NaN
LKCA15	04:39:17.80	+22:21:03.5	69.8242	22.3510	LkCa15	no	K5	12.09	0.0	0.	0.	0.	0.	0.	yes	8.600	0.018
TYC135	07:23:43.59	+20:24:58.6	110.9316	20.4163	TYC 1355-214-1	no	K5	9.93	0.0	0.	-65.8	1.7	-228.1	1.6	yes	7.032	0.017
HAT-P-13	08:39:31.81	+47:21:07.330	129.88255	47.352036	TYC 3416-543-1	no	G4	10.42	0.0	0.	-25.2	1.0	-27.6	1.0	yes	9.058	0.017
HD23912	03:49:32.7263	+23:22:49.464	57.38360	23.380407	HD 23912	no	F3	9.14	0.	0.	20.90	2.1	-42.70	1.7	yes	8.097	0.024

[a]All column headers were abbreviated to fit on a single page. The full column headers are as follows:

- *Obj Name*: Name of the object as given in the logfile (e.g., "TYC135" not "TYC 135.")
- *RA (hms)*: Right ascension of the target star in hours:minutes:seconds.
- *Dec (dms)*: Declination of the target star in degrees:minutes:seconds.
- *RA (deg)*: Right ascension of the target star in degrees. Both the right ascension in hms and the right ascension in deg must be given.
- *Dec (deg)*: Declination of the target star in degrees. Both the declination in dms and the declination in deg must be given.
- *SIMBAD ID*: Target identifier used by SIMBAD. Search for the object at `http://simbad.u-strasbg.fr/simbad/` or `http://simbad.harvard.edu/simbad/` to determine the SIMBAD identifier.
- *In Hipparcos?*: Type "yes" if the object is included in the Hipparcos catalog and "no" if the object is not included in the Hipparcos catalog. The Hipparcos catalog may be accessed directly at `http://archive.ast.cam.ac.uk/hipp/hipparcos.html` or indirectly through VizieR (`http://vizier.u-strasbg.fr/`)or the Astronomer's Bazaar (`http://cdswww.u-strasbg.fr/cats/Cats.htx`).
- *Spectral Type*: The spectral type of the target star (e.g., "K5.")
- *V mag*: The v-band magnitude of the target star.
- *Parallax (mas)*: The parallax of the target star. If the star does not have a measured parallax, simply type 0.
- *Plx error (mas)*: The error on the measured parallax of the target star. If the star does not have a measured parallax, simply type 0.
- *Prop M. RA*: The proper motion of the target star in right ascension. If the star does not have a proper motion measurement, simply type 0.
- *Prop M. RA err*: The error on the proper motion of the target star in right ascension. If the star does not have a proper motion measurement, simply type 0.
- *Prop M. Dec*: The proper motion of the target star in declination. If the star does not have a proper motion measurement, simply type 0.
- *Prop M. Dec err*:The error on the proper motion of the target star in declination. If the star does not have a proper motion measurement, simply type 0.
- *In 2MASS?*: Type "yes" if the object is included in the 2MASS catalog and "no" if the object is not included in the 2MASS catalog. The 2MASS catalog can be accessed at `http://www.ipac.caltech.edu/2mass/`.
- *H mag*: The H-band magnitude of the target star.
- *H mag err*: The error on the H-band magnitude of the target star.

Bibliography

Absil, O. & Mawet, D. 2009, A&A Rev., 16

Albrow, M. D., Beaulieu, J., Caldwell, J. A. R., et al. 2000, ApJ, 535, 176

Alibert, Y., Mordasini, C., & Benz, W. 2004, A&A, 417, L25

Alonso, R., Brown, T. M., Torres, G., et al. 2004, ApJ, 613, L153

Anglada-Escudé, G., Shkolnik, E. L., Weinberger, A. J., et al. 2010, ApJ, 711, L24

Apai, D., Meyer, M. R., Hinz, P. M., et al. 2007, in Bulletin of the American Astronomical Society, Vol. 38, Bulletin of the American Astronomical Society, 781–+

Artigau, É., Biller, B. A., Wahhaj, Z., et al. 2008, in Society of Photo-Optical Instrumentation Engineers (SPIE) Conference Series, Vol. 7014, Society of Photo-Optical Instrumentation Engineers (SPIE) Conference Series

Babcock, H. W. 1953, PASP, 65, 229

Bahcall, J. N. & Spitzer, Jr., L. 1982, Scientific American, 247, 40

Bakos, G., Afonso, C., Henning, T., et al. 2009, in IAU Symposium, Vol. 253, IAU Symposium, 354–357

Baraffe, I. & Chabrier, G. 1996, ApJ, 461, L51+

Barge, P., Baglin, A., Auvergne, M., et al. 2008, A&A, 482, L17

Barnes, S. A. 2007, ApJ, 669, 1167

Basri, G., Marcy, G. W., & Graham, J. R. 1996, ApJ, 458, 600

Bean, J. L., Seifahrt, A., Hartman, H., et al. 2010, ApJ, 711, L19

Beaulieu, J.-P., Bennett, D. P., Fouqué, P., et al. 2006, Nature, 439, 437

Beckers, J. M. 1993, ARA&A, 31, 13

Béjar, V. J. S., Zapatero Osorio, M. R., Pérez-Garrido, A., et al. 2008, ApJ, 673, L185

Benedict, Jr., R., Breckinridge, J. B., & Fried, D. L. 1994, Journal of the Optical Society of America A, 11, 257

Bennett, D. P. 2008, Detection of Extrasolar Planets by Gravitational Microlensing, ed. Mason, J., 47–88

Benvenuto, O. G., Fortier, A., & Brunini, A. 2009, Icarus, 204, 752

Benz, W., Mordasini, C., Alibert, Y., & Naef, D. 2006, in Tenth Anniversary of 51 Peg-b: Status of and prospects for hot Jupiter studies, ed. L. Arnold, F. Bouchy, & C. Moutou, 24–34

Biller, B. A. 2007, PhD thesis, The University of Arizona

Biller, B. A., Close, L., Lenzen, R., et al. 2004, in Society of Photo-Optical Instrumentation Engineers (SPIE) Conference Series, Vol. 5490, Society of Photo-Optical Instrumentation Engineers (SPIE) Conference Series, ed. D. Bonaccini Calia, B. L. Ellerbroek, & R. Ragazzoni, 389–397

Biller, B. A., Close, L. M., Masciadri, E., et al. 2006, in Presented at the Society of Photo-Optical Instrumentation Engineers (SPIE) Conference, Vol. 6272, Society of Photo-Optical Instrumentation Engineers (SPIE) Conference Series

Biller, B. A., Wahhaj, Z., Liu, M., et al. 2010, in Bulletin of the American Astronomical Society, Vol. 41, Bulletin of the American Astronomical Society, 457–+

Bodenheimer, P. & Pollack, J. B. 1986, Icarus, 67, 391

Borucki, W. J., Koch, D., Basri, G., et al. 2010, Science, 327, 977

Boss, A. P. 1997, Science, 276, 1836

Boss, A. P., Weinberger, A. J., Anglada-Escudé, G., et al. 2009, PASP, 121, 1218

Bovy, J., Hogg, D. W., & Roweis, S. T. 2009, ApJ, 700, 1794

Brandner, W., Apai, D., Lenzen, R., Feldt, M., & Huélamo, N. 2005, in Astronomical Society of the Pacific Conference Series, Vol. 343, Astronomical Polarimetry: Current Status and Future Directions, ed. A. Adamson, C. Aspin, C. Davis, & T. Fujiyoshi, 75–+

Brown, T. M. 2003, ApJ, 593, L125

Bryden, G., Beichman, C. A., Trilling, D. E., et al. 2006, ApJ, 636, 1098

Buffington, A., Crawford, F. S., Muller, R. A., & Orth, C. D. 1977, Journal of the Optical Society of America (1917-1983), 67, 304

Burrows, A., Hubbard, W. B., Lunine, J. I., & Liebert, J. 2001, Reviews of Modern Physics, 73, 719

Burrows, A., Marley, M., Hubbard, W. B., et al. 1997, ApJ, 491, 856

Butler, R. P. & Marcy, G. W. 1996, ApJ, 464, L153+

Butler, R. P., Marcy, G. W., Williams, E., Hauser, H., & Shirts, P. 1997, ApJ, 474, L115+

Cameron, A. C., Bouchy, F., Hébrard, G., et al. 2007, MNRAS, 375, 951

Cardini, D. & Cassatella, A. 2007, ApJ, 666, 393

Carroll, B. & Ostlie, D. 2007, An Introduction to Modern Astrophysics (Pearson Addison Weasley, New York, NY, 2nd ed.)

Castellano, T., Jenkins, J., Trilling, D. E., Doyle, L., & Koch, D. 2000, ApJ, 532, L51

Cenarro, A. J., Peletier, R. F., Sánchez-Blázquez, P., et al. 2007, MNRAS, 374, 664

Charbonneau, D., Berta, Z. K., Irwin, J., et al. 2009, Nature, 462, 891

Charbonneau, D., Brown, T. M., Latham, D. W., & Mayor, M. 2000, ApJ, 529, L45

Charbonneau, D., Brown, T. M., Noyes, R. W., & Gilliland, R. L. 2002, ApJ, 568, 377

Chauvin, G., Lagrange, A., Dumas, C., et al. 2004, A&A, 425, L29

Chauvin, G., Lagrange, A., Zuckerman, B., et al. 2005, A&A, 438, L29

Chung, S., Kim, D., Darnley, M. J., et al. 2006, ApJ, 650, 432

Chwolson, O. 1924, Astronomische Nachrichten, 221, 329

Covone, G., de Ritis, R., Dominik, M., & Marino, A. A. 2000, A&A, 357, 816

Cumming, A. 2004, MNRAS, 354, 1165

Cutri, R. M., Skrutskie, M. F., van Dyk, S., et al. 2003, 2MASS All Sky Catalog of point sources., ed. Cutri, R. M., Skrutskie, M. F., van Dyk, S., Beichman, C. A., Carpenter, J. M., Chester, T., Cambresy, L., Evans, T., Fowler, J., Gizis, J., Howard, E., Huchra, J., Jarrett, T., Kopan, E. L., Kirkpatrick, J. D., Light, R. M., Marsh, K. A., McCallon, H., Schneider, S., Stiening, R., Sykes, M., Weinberg, M., Wheaton, W. A., Wheelock, S., & Zacarias, N.

de Pater, I. & Lissauer, J. J. 2001, Planetary Sciences (Cambridge, UK, Cambridge University Press [2001] [1st ed.].)

Dehnen, W. 1998, AJ, 115, 2384

Delfosse, X., Forveille, T., Mayor, M., et al. 1998, A&A, 338, L67

Dodson-Robinson, S. E., Veras, D., Ford, E. B., & Beichman, C. A. 2009, ApJ, 707, 79

Downing, M., Finger, G., Baade, D., et al. 2008, in Presented at the Society of Photo-Optical Instrumentation Engineers (SPIE) Conference, Vol. 7015, Society of Photo-Optical Instrumentation Engineers (SPIE) Conference Series

Duffner, R. 2009, The Adaptive Optics Revolution: A History (University of New Mexico Press, 2009)

Duncan, D. K., Vaughan, A. H., Wilson, O. C., et al. 1991, ApJS, 76, 383

Egner, S. 2009, Disortion Correction for AO Imagers: Principles and Limitations, Poster available at `http://www.naoj.org/staff/egner/distortion/distortion.html`

Einstein, A. 1936, Science, 84, 506

Endl, M., Cochran, W. D., Tull, R. G., & MacQueen, P. J. 2003, AJ, 126, 3099

Fabrycky, D. C. & Winn, J. N. 2009, ApJ, 696, 1230

Feldt, M. 2009, in American Institute of Physics Conference Series, Vol. 1158, American Institute of Physics Conference Series, ed. T. Usuda, M. Tamura, & M. Ishii, 277–284

Figueira, P., Marmier, M., Bonfils, X., et al. 2010a, A&A, 513, L8+

Figueira, P., Pepe, F., Melo, C. H. F., et al. 2010b, A&A, 511, A55+

Fischer, D. A. & Valenti, J. 2005, ApJ, 622, 1102

Fortney, J. J., Lodders, K., Marley, M. S., & Freedman, R. S. 2008a, ApJ, 678, 1419

Fortney, J. J., Marley, M. S., Saumon, D., & Lodders, K. 2008b, ApJ, 683, 1104

Foy, R. & Labeyrie, A. 1985, A&A, 152, L29

Frink, S., Mitchell, D. S., Quirrenbach, A., et al. 2002, ApJ, 576, 478

Galileo Galilei. 1610, Sidereus nuncius (Palthenius)

Gaudi, B. S. 2010, ArXiv e-prints

Gaudi, B. S. & Gould, A. 1997, ApJ, 486, 85

Gaudi, B. S. & Winn, J. N. 2007, ApJ, 655, 550

Geballe, T. R., Knapp, G. R., Leggett, S. K., et al. 2002, ApJ, 564, 466

Gonzalez, G., Laws, C., Tyagi, S., & Reddy, B. E. 2001, AJ, 121, 432

Gould, A. & Loeb, A. 1992, ApJ, 396, 104

Gray, R. O., Corbally, C. J., Garrison, R. F., McFadden, M. T., & Robinson, P. E. 2003, AJ, 126, 2048

Griffin, R. 1973, MNRAS, 162, 243

Han, I., Black, D. C., & Gatewood, G. 2001, ApJ, 548, L57

Harrington, J., Luszcz, S., Seager, S., Deming, D., & Richardson, L. J. 2007, Nature, 447, 691

Heinze, A. N., Hinz, P. M., Kenworthy, M., et al. 2010a, ApJ, 714, 1570

Heinze, A. N., Hinz, P. M., Sivanandam, S., et al. 2010b, ApJ, 714, 1551

Henry, G. W., Marcy, G. W., Butler, R. P., & Vogt, S. S. 2000, ApJ, 529, L41

Herbig, G. H. & Spalding, Jr., J. F. 1955, ApJ, 121, 118

Hernán-Obispo, M., Gálvez, M. C., Anglada-Escudé, G., et al. 2009in (AIP), 441–444

Hernán-Obispo, M., Gálvez-Ortiz, M. C., Anglada-Escudé, G., et al. 2010, A&A, 512, A45+

HiCIAO: Critical Design Review. 2006, HiCIAO: Critical Design Review

HiCIAO Team. 2009, HiCIAO Performance Report for SEEDS

Hill, J. M. & Salinari, P. 2004, in Society of Photo-Optical Instrumentation Engineers (SPIE) Conference Series, Vol. 5489, Society of Photo-Optical Instrumentation Engineers (SPIE) Conference Series, ed. J. M. Oschmann Jr., 603–614

Hillenbrand, L. A. 2008, Physica Scripta Volume T, 130, 014024

Hillenbrand, L. A. 2009, in IAU Symposium, Vol. 258, IAU Symposium, ed. E. E. Mamajek, D. R. Soderblom, & R. F. G. Wyse, 81–94

Hinkley, S., Oppenheimer, B. R., Soummer, R., et al. 2009, ApJ, 701, 804

Hinkley, S., Oppenheimer, B. R., Soummer, R., et al. 2007, ApJ, 654, 633

Hodapp, K. W., Suzuki, R., Tamura, M., et al. 2008, in Society of Photo-Optical Instrumentation Engineers (SPIE) Conference Series, Vol. 7014, Society of Photo-Optical Instrumentation Engineers (SPIE) Conference Series

Høg, E., Fabricius, C., Makarov, V. V., et al. 2000, A&A, 355, L27

Høg, E., Kuzmin, A., Bastian, U., et al. 1998, A&A, 335, L65

Hogg, D. W., Blanton, M. R., Roweis, S. T., & Johnston, K. V. 2005, ApJ, 629, 268

Holman, M. J. & Murray, N. W. 2005, Science, 307, 1288

Hubickyj, O., Bodenheimer, P., & Lissauer, J. J. 2005, Icarus, 179, 415

Ida, S. & Lin, D. N. C. 2004, ApJ, 616, 567

Ingrosso, G., Novati, S. C., de Paolis, F., et al. 2009, MNRAS, 399, 219

Janson, M., Brandner, W., Henning, T., & Close, L. 2007, in Bulletin of the American Astronomical Society, Vol. 38, Bulletin of the American Astronomical Society, 968–+

Jenkins, J. S., Jones, H. R. A., Biller, B., et al. 2010, ArXiv e-prints

Johnson, J. A., Butler, R. P., Marcy, G. W., et al. 2007, ApJ, 670, 833

Kaifu, N., Usuda, T., Hayashi, S. S., et al. 2000, PASJ, 52, 1

Kalas, P., Graham, J. R., Chiang, E., et al. 2008, Science, 322, 1345

Kandori, R., Tamura, M., Morino, J., et al. 2009, in American Institute of Physics Conference Series, Vol. 1158, American Institute of Physics Conference Series, ed. T. Usuda, M. Tamura, & M. Ishii, 251–252

Kennedy, G. M. & Kenyon, S. J. 2008, ApJ, 673, 502

Kenyon, S. J. & Bromley, B. C. 2006, AJ, 131, 1837

Kenyon, S. J. & Bromley, B. C. 2008, ApJS, 179, 451

Kiraga, M. & Paczynski, B. 1994, ApJ, 430, L101

Kirkpatrick, J. D., Reid, I. N., Liebert, J., et al. 1999, ApJ, 519, 802

Kokubo, E., Kominami, J., & Ida, S. 2006, ApJ, 642, 1131

Koleva, M., Prugniel, P., Ocvirk, P., Le Borgne, D., & Soubiran, C. 2008, MNRAS, 385, 1998

Konacki, M., Maciejewski, A. J., & Wolszczan, A. 1999, ApJ, 513, 471

Kornet, K., Bodenheimer, P., Różyczka, M., & Stepinski, T. F. 2005, A&A, 430, 1133

Kratter, K. M., Murray-Clay, R. A., & Youdin, A. N. 2010, ApJ, 710, 1375

Kuhn, J. R., Potter, D., & Parise, B. 2001, ApJ, 553, L189

Kumar, S. S. 1963, ApJ, 137, 1121

Lafrenière, D., Doyon, R., Marois, C., et al. 2007a, ApJ, 670, 1367

Lafrenière, D., Marois, C., Doyon, R., Nadeau, D., & Artigau, É. 2007b, ApJ, 660, 770

Lagrange, A., Gratadour, D., Chauvin, G., et al. 2009, A&A, 493, L21

Lavigne, J.-F., Doyon, R., Lafrenire, D., Marois, C., & Barman, T. 2009, The Astrophysical Journal, 704, 1098

Lenzen, R., Close, L., Brandner, W., Hartung, M., & Biller, B. 2005, in Science with Adaptive Optics, ed. W. Brandner & M. E. Kasper, 46–+

Levison, H. F., Thommes, E., & Duncan, M. J. 2010, AJ, 139, 1297

Linnik, V. P. 1957, Optics and Spectroscopy, 3, 401

Linnik, V. P. 1994, in European Southern Observatory Astrophysics Symposia, Vol. 48, European Southern Observatory Astrophysics Symposia, ed. F. Merkle, 535–+

Lissauer, J. J. 1993, ARA&A, 31, 129

Loeb, A. & Sasselov, D. 1995, ApJ, 449, L33+

López-Santiago, J., Montes, D., Crespo-Chacón, I., & Fernández-Figueroa, M. J. 2006, ApJ, 643, 1160

Lovis, C. & Mayor, M. 2007, A&A, 472, 657

Macintosh, B., Poyneer, L., Sivaramakrishnan, A., & Marois, C. 2005, in Society of Photo-Optical Instrumentation Engineers (SPIE) Conference Series, Vol. 5903, Society of Photo-Optical Instrumentation Engineers (SPIE) Conference Series, ed. R. K. Tyson & M. Lloyd-Hart, 170–177

Malhotra, R., Black, D., Eck, A., & Jackson, A. 1992, Nature, 356, 583

Mamajek, E. E. & Hillenbrand, L. A. 2008, ApJ, 687, 1264

Mao, S. & Paczynski, B. 1991, ApJ, 374, L37

Marley, M. S., Fortney, J. J., Hubickyj, O., Bodenheimer, P., & Lissauer, J. J. 2007, ApJ, 655, 541

Marois, C., Doyon, R., Nadeau, D., et al. 2005, PASP, 117, 745

Marois, C., Doyon, R., Nadeau, D., Racine, R., & Walker, G. A. H. 2003, in EAS Publications Series, Vol. 8, EAS Publications Series, ed. C. Aime & R. Soummer, 233–243

Marois, C., Doyon, R., Racine, R., & Nadeau, D. 2000, PASP, 112, 91

Marois, C., Lafrenière, D., Macintosh, B., & Doyon, R. 2008a, ApJ, 673, 647

Marois, C., Macintosh, B., Barman, T., et al. 2008b, Science, 322, 1348

Marois, C., Phillion, D. W., & Macintosh, B. 2006, in Society of Photo-Optical Instrumentation Engineers (SPIE) Conference Series, Vol. 6269, Society of Photo-Optical Instrumentation Engineers (SPIE) Conference Series

Martin, E. L., Basri, G., Delfosse, X., & Forveille, T. 1997, A&A, 327, L29

Martín, E. L., Dahm, S., & Pavlenko, Y. 2001, in Astronomical Society of the Pacific Conference Series, Vol. 245, Astrophysical Ages and Times Scales, ed. T. von Hippel, C. Simpson, & N. Manset, 349–+

Matsuo, T. 2009a, SEEDS Open Cluster Category, Presentation at SEEDS All-Category Meeting

Matsuo, T. 2009b, SEEDS: Status of OC Category, Presentation at SEEDS All-Category Meeting

Matsuo, T., Shibai, H., Ootsubo, T., & Tamura, M. 2007, ApJ, 662, 1282

Matzner, C. D. & Levin, Y. 2005, ApJ, 628, 817

Max, C. 2001, Introduction to Adaptive Optics and its History, `http://cfao.ucolick.org/EO/resources/History_AO_Max.pdf`

Mayne, N. J., Naylor, T., Littlefair, S. P., Saunders, E. S., & Jeffries, R. D. 2007, MNRAS, 375, 1220

Mayor, M., Bonfils, X., Forveille, T., et al. 2009, A&A, 507, 487

Mayor, M. & Queloz, D. 1995, Nature, 378, 355

McElwain, M., Matsuo, T., Turner, E., Knapp, J., & Moro-Martin, A. 2009, Moving Group Targets for SEEDS, Presentation at SEEDS All-Category Meeting

McElwain, M. W., Metchev, S. A., Larkin, J. E., et al. 2007, ApJ, 656, 505

McGrath, M. A., Nelan, E., Black, D. C., et al. 2002, ApJ, 564, L27

McGrath, M. A., Nelan, E., Noll, K., et al. 2003, in Astronomical Society of the Pacific Conference Series, Vol. 294, Scientific Frontiers in Research on Extrasolar Planets, ed. D. Deming & S. Seager, 145–150

McLaughlin, D. B. 1924, ApJ, 60, 22

Mizuno, H. 1980, Progress of Theoretical Physics, 64, 544

Moro-Martin, A. 2008, SEEDS Debris Disks Target Selection Strategy, Science Workshop on SEEDS

Neuhäuser, R., Guenther, E. W., Wuchterl, G., et al. 2005, A&A, 435, L13

Newburn, Jr., R. L. & Gulkis, S. 1973, Space Science Reviews, 14, 179

Newton, I. 1687, Philosophi naturalis principia mathematica (Jussu Societas Regi ac typis Josephi Streater, prostant venales apud Sam. Smith)

Newton, I. 1718, Opticks: or, A treatise of the reflexions, refractions, inflexions and colours of light, 2nd Ed. (Printed for W. and J. Innys, printers to the Royal Society, at the Prince's-Arms in St. Paul's Church-Yard)

O'Connor, E. F. 1966, Saturn V launch vehicle report, Tech. Rep. AIAA PAPER 66-840, NASA, Marshall Space Flight Center

Ohta, Y., Taruya, A., & Suto, Y. 2005, ApJ, 622, 1118

Oppenheimer, B. R. & Hinkley, S. 2009, ARA&A, 47, 253

Peale, S. J. 1993, AJ, 105, 1562

Perryman, M. A. C., de Boer, K. S., Gilmore, G., et al. 2001, A&A, 369, 339

Perryman, M. A. C. & ESA, eds. 1997, ESA Special Publication, Vol. 1200, The HIPPARCOS and TYCHO catalogues. Astrometric and photometric star catalogues derived from the ESA HIPPARCOS Space Astrometry Mission

Pollack, J. B., Hubickyj, O., Bodenheimer, P., et al. 1996, Icarus, 124, 62

Popper, D. M. 1993, ApJ, 404, L67

Pravdo, S. H. & Shaklan, S. B. 2009, ApJ, 700, 623

Queloz, D., Mayor, M., Weber, L., et al. 2000, A&A, 354, 99

Racine, R. 1989, PASP, 101, 436

Racine, R., Walker, G. A. H., Nadeau, D., Doyon, R., & Marois, C. 1999, PASP, 111, 587

Rafikov, R. R. 2005, ApJ, 621, L69

Rasio, F. A., Nicholson, P. D., Shapiro, S. L., & Teukolsky, S. A. 1992, Nature, 355, 325

Raymond, S. N., Quinn, T., & Lunine, J. I. 2006, Icarus, 183, 265

Rebolo, R., Martin, E. L., & Magazzu, A. 1992, ApJ, 389, L83

Refsdal, S. 1964, MNRAS, 128, 295

Reid, I. N. 2002, PASP, 114, 306

Reid, I. N., Cruz, K. L., Allen, P., et al. 2004, AJ, 128, 463

Rivera, E. J., Lissauer, J. J., Butler, R. P., et al. 2005, ApJ, 634, 625

Roddier, F. 1981, Prog. Optics, Volume 19, p. 281-376, 19, 281

Rossiter, R. A. 1924, ApJ, 60, 15

Santos, N. C., Israelian, G., & Mayor, M. 2001, A&A, 373, 1019

Santos, N. C., Israelian, G., & Mayor, M. 2004, A&A, 415, 1153

Santos, N. C., Israelian, G., Mayor, M., et al. 2005, A&A, 437, 1127

Santos, N. C., Mayor, M., Naef, D., et al. 2000, A&A, 361, 265

Schilbach, E., Robichon, N., Souchay, J., & Guibert, J. 1995, A&A, 299, 696

Schmidt, T. O. B., Neuhäuser, R., Seifahrt, A., et al. 2008, A&A, 491, 311

Schneider, G. & Silverstone, M. D. 2003, in Society of Photo-Optical Instrumentation Engineers (SPIE) Conference Series, Vol. 4860, Society of Photo-Optical Instrumentation Engineers (SPIE) Conference Series, ed. A. B. Schultz, 1–9

Serra, P. & Trager, S. C. 2007, MNRAS, 374, 769

Shectman, S. A., Thompson, I. B., & Perex, F. 2009, in Astronomy, Vol. 2010, astro2010: The Astronomy and Astrophysics Decadal Survey, 22–+

Shen, Y. & Turner, E. L. 2008, ApJ, 685, 553

Song, I., Caillault, J., Barrado y Navascués, D., Stauffer, J. R., & Randich, S. 2000, ApJ, 533, L41

Sozzetti, A. 2005, PASP, 117, 1021

Sozzetti, A. 2009, ArXiv e-prints

Stamatellos, D. & Whitworth, A. P. 2008, A&A, 480, 879

Suzuki, R., Tamura, M., Suto, H., et al. 2009, in American Institute of Physics Conference Series, Vol. 1158, American Institute of Physics Conference Series, ed. T. Usuda, M. Tamura, & M. Ishii, 293–298

Takami, H. 2008, in Society of Photo-Optical Instrumentation Engineers (SPIE) Conference Series, Vol. 7014, Society of Photo-Optical Instrumentation Engineers (SPIE) Conference Series

Takeda, G., Ford, E. B., Sills, A., et al. 2007, ApJS, 168, 297

Tamura, M. 2009a, SEEDS and HiCIAO Status, Presentation at SEEDS All-Category Meeting

Tamura, M. 2009b, in American Institute of Physics Conference Series, Vol. 1158, American Institute of Physics Conference Series, ed. T. Usuda, M. Tamura, & M. Ishii, 11–16

Tamura, M., Hodapp, K., Takami, H., et al. 2006, in Society of Photo-Optical Instrumentation Engineers (SPIE) Conference Series, Vol. 6269, Society of Photo-Optical Instrumentation Engineers (SPIE) Conference Series

Tamura, M., Takami, H., Suto, H., et al. 1998, in Astronomical Society of the Pacific Conference Series, Vol. 134, Brown Dwarfs and Extrasolar Planets, ed. R. Rebolo, E. L. Martin, & M. R. Zapatero Osorio, 338–+

Tamura, M., Usuda, T., & Takami, H. 2004, Subaru Stategic Exploration of Exoplanets and Disks with HiCIAO/AO188 (SEEDS), Subaru Telescope "Strategic Observations" Proposal

Tarter, J. C. 1975, PhD thesis, California Univ., Berkeley.

Tarter, J. C. 1986, in Astrophysics of Brown Dwarfs, ed. M. C. Kafatos, R. S. Harrington, & S. P. Maran, 121–138

ter Horst, R., Tromp, N., de Haan, M., et al. 2008, in Society of Photo-Optical Instrumentation Engineers (SPIE) Conference Series, Vol. 7018, Society of Photo-Optical Instrumentation Engineers (SPIE) Conference Series

Thalmann, C., Carson, J., Janson, M., et al. 2009, ApJ, 707, L123

Tinney, C. G., Butler, R. P., Marcy, G. W., et al. 2001, ApJ, 551, 507

Unwin, S. C., Shao, M., Tanner, A. M., et al. 2008, PASP, 120, 38

Valencia, D., Sasselov, D. D., & O'Connell, R. J. 2007, ApJ, 656, 545

Wachsmuth, I. K., Blake, P. A., & Olsvik, Ø. 1994, *Vibrio cholerae* and Cholera: molecular to global perspectives (American Society for Microbiology)

Wolszczan, A. 1994, Science, 264, 538

Wolszczan, A. & Frail, D. A. 1992, Nature, 355, 145

Wright, J. T., Marcy, G. W., Butler, R. P., & Vogt, S. S. 2004, ApJS, 152, 261

YSO Category Team. 2008, Summary of SEEDS YSO Category Materials, Presentation at SEEDS All-Category Meeting

Zuckerman, B. & Song, I. 2004, ARA&A, 42, 685